Abstract

TIAN, MING. Numerical Simulation of the Internal Two-Phase Flow within an Aerated-Liquid Injector and its Injection into the Corresponding High-speed Crossflows. (Under the direction of Dr. Jack R. Edwards.)

The current study investigates the flow structures within an aerated-liquid (barbotage) injector, which is designed to facilitate the rapid breakup of a hydrocarbon fuel jet prior to its entering a scramjet combustor, and the spray structures in the corresponding crossflow. Simulations of the transient, three-dimensional, two-phase flow within the "out-in" injector operating at different gas-to-liquid (GLR) mass ratios and in the corresponding crossflow domain have been performed, and the results compared with experimental pressure measurements of the injector and shadowgraph images of the crossflow. The numerical method solves a "mixture" model of two-phase flow using a preconditioning strategy. High-order spatial accuracy and good interface-capturing properties are facilitated by the use of shock-capturing schemes combined with second order TVD methods. Also, an immersed boundary method is used to investigate the probe effects, and a droplet transport model is used in the crossflow simulations to get more details about effect of droplet size.

The injector simulation results highlight the effects of mesh refinement and turbulence model on the predicted solutions. The pressure drop across the injector is predicted reasonably well by the computational methodology, and the trend of increasing injector pressure with increasing GLR is captured properly. Predictions of the absolute pressure level within the injector show some discrepancies in comparison with experimental data but agree well with theoretical estimates. The results of the injector simulations with plenum included are consistent with the results of the discharge tube cases. If the centerline pressure is close to the experimental data, the gas mass flow rate at outlet will approach a value below the experimental data. If the

gas mass flow rate at outlet approaches the experimental data, then the centerline pressure will be higher than the experimental data, but agrees well with theoretical analyses. The intrusion of the probe has little effect on the flowfield if the probe is contained wholly within the liquid core, but does affect the flowfield if the probe tip is in the two-phase mixing region, instead of the liquid core.

The results of crossflow show that the two-phase flow injects into the crossflow, bends towards the streamwise direction, disperses into a spray plume, and initiates a horseshoe-shape structure of the jet in the cross-sectional planes. The result based on the previous injector simulation at a higher inlet gas pressure shows best penetration height prediction among all $M_\infty = 0.3$ cases. Including the droplet transport model gives a similar spray structure in the X-Z centerplane as that of the mixture model, but gives a different spray structure in the cross-sectional planes. The horseshoe-shaped structure fades away with increases in the droplet diameter size, and the liquid mass accumulates to the X-Z centerplane.

Numerical Simulation of the Internal Two-Phase Flow within an Aerated-Liquid Injector and its Injection into the Corresponding High-speed Crossflows

by

Ming Tian

A dissertation submitted to the Graduate Faculty of
North Carolina State University
in partial fulfillment of the
requirements for the Degree of
Doctor of Philosophy

Department of Mechanical and Aerospace Engineering

Raleigh, NC
August 15, 2005

Approved by:

Dr. Hassan A. Hassan	Dr. D. Scott McRae
Dr. Zhilin Li	Dr. Jack R. Edwards, Chair

Biography

Ming Tian was born in Chengdu, Sichuan, China on April 6, 1974 to Tianrong Ni and Zuyang Tian. His birthday happened to coincide with the QingMing Festival, a traditional Chinese holiday to commemorate the ancestors. In 1986, Ming attended The 12th Middle/High School of Chengdu, one of the best middle/high schools in Sichuan. Ming took interest in Mathematics and Physics in the early middle school years.

In the Autumn of 1992, Ming left his hometown for Beijing to start his college life at Beijing University of Aeronautics and Astronautics (BUAA). The title of his bachelor's thesis is " An Experimental Investigation of Aerodynamic Characteristics over Oscillating Delta Wings at a Very High Angle of Attack in a Low-speed Wind Tunnel". After he received Bachelor of Engineering degree in Aerodynamics from BUAA in 1996, Ming was admitted to the graduate school of Beijing University in 1997. His study at Beijing University focused on the experimental fluid mechanics. In the summer of 2000, Ming met his girlfriend, Yu Chen, who became his wife on December 25th, 2000.

Ming continued his graduate study majored in Aerospace Engineering at North Carolina State University since Fall 2000, and received Master of Science degree in Aerospace Engineering from NCSU in December 2002. The title of his Master's thesis is "A Numerical Simulation of Internal Two-Phase Flow for Aerated-Liquid Injectors". Ming and Yu became Christians on August 28th, 2004. Ming will start to find a research position after his graduation.

When writing this dissertation, Ming and Yu are expecting their first baby who will be born in this September.

Acknowledgments

First and foremost, I would like to thank my advisor, Dr. Jack R. Edwards, not only for giving me the opportunity to study at NCSU, guiding my academic and professional development for the past five years, but also for the influence on me from his diligence and creativity. I would also like to thank Dr. Hassan A. Hassan and Dr. D. Scott McRae for their help in my Fluid dynamics and CFD course work and research. Thanks also go to Dr. Zhilin Li for serving on my advisory committee and instructing and discussing with me the interface capturing techniques. I'm also thankful to Dr. Tarek Echekki for agreeing to serve as a substitution for Dr. McRae on short notice.

Then, I would like to thank my parents for guiding me through my first steps of life and education. They created a nice environment for me to grow up healthily and gradually. Also I'm grateful to my loving wife, Yu Chen, for her supporting and companying me for my study in the United States.

I would like to acknowledge Taitech, Inc. for sponsoring this research under subcontract from the Air Force Research Laboratory, Wright-Patterson AFB. I also acknowledge North Carolina State University High Performance Computing Division for granting parallel-computer time and continuously supporting my research computations.

Thanks also due to every instructor who taught me in the past five years, all former and current colleagues in Hypersonics Lab, 4216 Broughton Hall, and Gwendolyn J. Smith in the department main office for all the help and support in my study in the United States.

Table of Contents

List of Tables

List of Figures

List of Symbols

Roman symbols:

A	area
a	sound speed
C_p	specific heat at constant pressure
$\mathbf{E}, \mathbf{F}, \mathbf{G}$	inviscid flux vector in ξ, η, ζ directions
$\mathbf{E_v}, \mathbf{F_v}, \mathbf{G_v}$	viscous flux vector in ξ, η, ζ directions
g	gravity acceleration
H	total enthalpy per mass of mixture
h	mixture enthalpy per mass
h	phase interface thickness in continuum surface force model
i, j, k	indices corresponding to ξ, η, and ζ directions
J	Jacobian of coordinate transformation
k	turbulent kinetic energy
M	Mach number
m	mass
N_g	number of gas components
N_l	number of liquid components
$\hat{n}$	unit vector normal to a surface
$\mathbf{P}$	preconditioning matrix
p	pressure
Pr	Prandtl number
q_i	laminar heat-flux vector
$q_{t,i}$	turbulent heat-flux vector
R	discrete representation of the steady part of governing equation set
$\mathbf{R}$	Residual vector
$\mathcal{R}$	universal gas constant
$\mathcal{R}_{mix}$	specific gas constant of the mixture gas
Re	Reynolds number
$\mathbf{S}$	source term vector
Sc	Schmidt number
T	temperature
t	time
t_{ij}	stress tensor
$\mathbf{U}$	vector of conservative variables
$\mathbf{u}$	velocity vector
u, v, w	Cartesian velocities in x, y, z directions
$u_{d,i}, v_{d,i}, w_{d,i}$	Cartesian molecular diffusion velocities of component i in gas phase
u_i	Cartesian velocity in index notation

u_r	relative velocity between gas phase and liquid phase
$\mathcal{U}, \mathcal{V}, \mathcal{W}$	contravariant velocity components
$\mathcal{U}_{d,i}, \mathcal{V}_{d,i}, \mathcal{W}_{d,i}$	contravariant diffusion velocity components of species i in gas phase
$\mathbf{V}$	vector of primitive variables
V	total volume of the system or grid cell volume
V_g, V_l	actual volume of gas phase and actual volume of liquid phase
$W_{g,i}$	molecular weight of component i in gas phase
x, y, z	Cartesian coordinates
x_i	Cartesian coordinate in index notation
$\mathbf{x}$	location vector
Y_g	mass fraction of gas phase in the mixture
$y_{g,i}$	mass fraction of component i in gas phase
Y_l	mass fraction of liquid phase in the mixture
$y_{l,j}$	mass fraction of component j in liquid phase

Greek symbols:

α	volume fraction
δ	delta function in derivation of surface tension
δ_{ij}	Kronecker delta
ϵ	turbulent dissipation rate
κ	Karman's constant, or curvature in surface tension
λ	thermal conductivity coefficient or eigenvalue
μ	laminar viscosity
μ_t	turbulent viscosity
ξ, η, ζ	generalized coordinates
ξ_i	generalized coordinate in index notation
ρ	mixture density
σ	fluid surface tension coefficient
τ_{ij}	turbulent stress tensor
Ω	vorticity vector
ω	specific dissipation rate
$\chi_{g,i}$	mole fraction of component i in gas phase

Subscripts:

$\frac{1}{2}$	represents a numerical interface quantity
∞	represents a freestream quantity
g	represents a property in gas phase
i, j, k	represents spatial coordinates or cell indices
l	represents a property in liquid phase
m	represents chemical species
p	represents partial derivative with respect to variable p
t	represents turbulent property

T	represents partial derivative with respect to variable T

Superscripts:

c	represents convective component in flux vector
k	represents pseudo time level
n	represents physical time level
p	represents pressure component in flux vector
T	represents the transpose of a matrix

Accents:

$\bar{}$	represents a Reynolds averaged quantity
$\tilde{}$	represents a Favre averaged quantity

Abbreviations:

AUSM	Advective Upwind Splitting Method
BC	Boundary Condition
CFD	Computational Fluid Dynamics
CSF	Continuum Surface Force
GLR	Gas to Liquid mass Ratio
ILU	Incomplete Lower-Upper factorization method
LDFSS	Low-Diffusion Flux-Splitting Scheme
MPI	Message-Passing Interface
RANS	Reynolds-Averaged Navier-Stokes equations
TVD	Total Variation Diminishing

Chapter 1

Introduction

Liquid atomization is a process of great importance in practical applications. Today, implementation of liquid atomization is found in many fields of industry: aerospace, chemical, civil, and mechanical engineering; pharmaceuticals; medicine; agriculture; food and others.

Fuels and water are the most commonly atomized liquids. Liquid fuels are the basic sources of energy consumed by aircraft combustors. The successful design of a liquid-fueled, air-breathing propulsion system depends to a significant extent on liquid atomization performance, which determines the mixing behavior and the combustion efficiency of the combustor. Aerated-liquid atomization (also called "effervescent atomization" or "barbotage"), which is produced by the introduction of gas directly into a liquid flow immediately upstream of the injector exit orifice to generate a two-phase flow, has been shown to produce well-atomized sprays in a quiescent environment with only a small amount of aerating gas at relatively low injection pressures.

Refs. [1–8] provide an overview of the development and use of aerated-liquid atomization techniques at the Air Force Research Laboratory's Propulsion Directorate (AFRL/PRA). Such techniques provide a means of promoting the rapid initial breakup of liquid fuel jets into an array of very small droplets and thus are suited for applications in the low hypersonic Mach number range (Mach 4 to 5), where the heating load may be insufficient to facilitate the transition of an endothermic fuel from a liquid state to a supercritical (near gaseous) state prior to injection.

Aerated-liquid atomization techniques involve the direct injection of gas into the

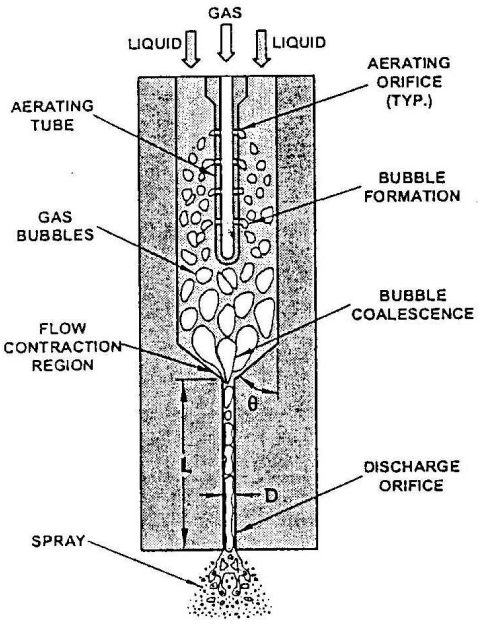

Figure 1.1: Schematic of "in-out" aerated-liquid injector

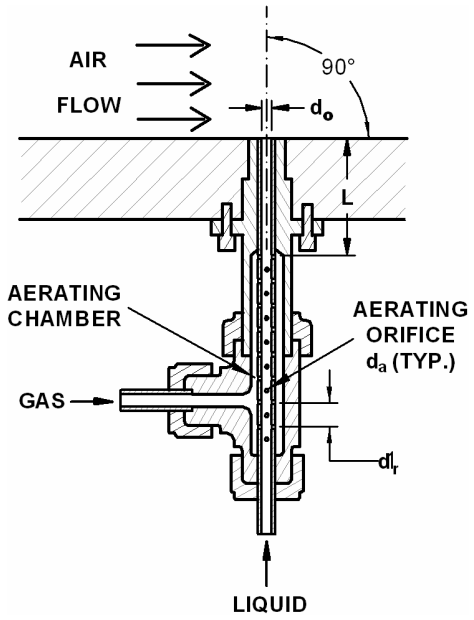

Figure 1.2: Schematic of "out-in" aerated-liquid injector

liquid flow upstream of the fuel injector exit. The aerating gas interacts with the liquid core fluid, initiating a breakup mechanism within the injector. The precise details of the mechanism depend on the type of aeration. For example, Lin, et al. [6] constructed an "in-out" aerated-liquid injector in which aerating gas was injected through a tube oriented along the centerline of a co-flowing liquid stream. (see Fig. 1.1) At high aeration levels, the aerating gas filled the majority of the inner portion of the injector, displacing the liquid toward the walls of the discharge passage. The liquid jet exited as a annular sheet, rather than a round core, facilitating its rapid breakup through aerodynamic shearing forces acting on the interior and exterior surfaces of the sheet. This case was simulated numerically in Ref. [9]. Qualitative agreement with experimental shadowgraph imaging was indicated, and the general effects of different aeration levels on the two-phase flow structure were successfully predicted. The "in-out" configurations tested in Lin, et al. [6] proved to be less than successful in actual implementations. Even though good droplet-size distributions were obtained,

the spray would pulsate due to acoustic interactions within the injector.

Another design is an "out-in" injector (see Fig. 1.2). In this variant, the aerating gas is first injected into a plenum, then is dispersed nearly uniformly through an array of small holes into a tube containing the flowing liquid. This design has been successfully used to atomize liquid jets exiting into subsonic and supersonic crossflows [7; 8]. Experimental measurements of the spray pattern indicate that the out-in atomizer configuration produces a fine spray without the pulsating effect found in the in-out configurations.

The goal of this computational study is to provide insight into the physical mechanisms that lead to accelerated liquid breakup within the out-in injector configuration and to the spray structures observed during injection into a crossflow. Such information can be used to better predict the performance of such injectors and to enable design modifications that result in improved spray penetration. Other objectives include the further validation of the two-phase flow simulation techniques described in Ref. [9] and the establishment of realistic initial conditions for future simulations of spray development within hydrocarbons-fueled scramjet combustors.

As an initial step, a 3-D Navier-Stokes solver for a "mixture" model of two-phase flow is developed. This code is based on the combination of time-derivative preconditioning [10–16] and low-diffusion upwinding methods [17; 18]. A dual-time stepping method [14; 16] is used to ensure time-accurate evolution of the governing equations.

Chapter 2 gives the derivation of two-phase mixture model utilized in the current study. Chapter 3 introduces the preconditioning method, presents an extension of the Low-Diffusion Flux-Splitting Scheme [17; 18] valid for two-phase mixture flows, and describes an incomplete lower-upper (LU) implicit method [19] to advance the nonlinear system in time. Chapter 4 briefly describes the experimental procedure, formulates the geometry, and presents initial and boundary conditions.

Chapter 5 presents and discusses the results of several simulations of the 3-D out-in type aerated-liquid injector flowfield at several gas-to-liquid (GLR) mass ratios and the results of the simulations of aerated-liquid injection into subsonic crossflow environments. In this chapter, a one-dimensional theoretical analysis is used to predict the exit pressure and inlet pressure for cases where the two-phase flow is assumed isothermal and in thermal non-equilibrium. Also, the pressure probe effects are simulated using level set method [20–23] and immersed boundary method [24–27]. In the crossflow simulations, a droplet transport model, which decouples the calculations between gas phase and liquid phase, is used to get more details about effects of droplet size and velocity slip on spray penetration.

Chapter 6 gives the conclusions. Finally, derivations of the real fluid sound speed, eigenvalues of the preconditioned system, interface flux Jacobian matrices, 1-D injector theoretical analysis and the immersed boundary algorithm are presented in Appendices A, B, C, D and E. respectively.

Chapter 2

Derivation of the Two-Phase Flow Models

In this chapter, the two-phase mixture model used in this study is developed in detail. Then the droplet transport model is described briefly. These models are implemented in general-coordinate finite volume form in the computations. The mixture model solves the preconditioned Navier-Stokes equations describing a compressible, multi-component, two-phase (gas/liquid) flow. The droplet transport model is a decoupled analysis of the two-phase flow. The flow is assumed isothermal in the injector simulations and is assumed in thermal non-equilibrium in the crossflow simulations. In order to get a better understanding of the two-phase mixture model, we start with some definitions used in this model. In general, subscripts "g" and "l" refer to "gas phase" and "liquid phase" respectively. Detailed descriptions can be found in Ref. [28].

2.1 Definitions

2.1.1 Volume Fraction

Volume fraction represents the volume occupied by a particular phase, referenced to the system's total volume. In our mixture model, there are two phases, gas phase and liquid phase. For the gas phase, the gas volume fraction is expressed as:

$$\alpha_g = \frac{V_g}{V_g + V_l} = \frac{V_g}{V} \tag{2.1}$$

where V_g is the volume of the gas phase, V_l is the volume of the liquid phase, and V is the total volume of the system. Similarly, the liquid volume fraction is expressed as: $\alpha_l = \frac{V_l}{V} = \frac{V - V_g}{V} = 1 - \alpha_g$.

2.1.2 Mixture Density

The mixture or bulk density of the two-phase system is the volume-fraction weighted average of the gas phase density and liquid phase density. It is defined as:

$$\rho = \rho_g \alpha_g + \rho_l \alpha_l, \quad \text{or} \quad \frac{1}{\rho} = \frac{Y_g}{\rho_g} + \frac{Y_l}{\rho_l}, \tag{2.2}$$

where ρ_g and ρ_l are the actual densities of the gas phase and liquid phase respectively, and Y_g and Y_l are mass fractions of the gas phase and liquid phase respectively, which are defined as follows.

2.1.3 Mass Fraction and Mole Fraction

In the two-phase system, the mass fraction of gas phase, Y_g, is the ratio of the mass of gas phase to the total mass of the system, and written as:

$$Y_g = \frac{m_g}{m} = \frac{\rho_g V_g}{\rho V} = \frac{\rho_g V_g / V}{\rho} = \frac{\rho_g \alpha_g}{\rho_g \alpha_g + \rho_l \alpha_l} \tag{2.3}$$

where m_g is the mass of the gas phase, and m is the total mass of the system. Similarly, the mass fraction of the liquid phase can be written as:

$$Y_l = \frac{m_l}{m} = \frac{\rho_l V_l}{\rho V} = \frac{\rho_l \alpha_l}{\rho_g \alpha_g + \rho_l \alpha_l} = 1 - Y_g \tag{2.4}$$

where m_l is the mass of the liquid phase.

If the gas phase consists of N_g components, then the mass fraction of component i in the gas phase is defined as the ratio of the mass of component i to the mass of gas phase. It can be written as:

$$y_{g,i} = \frac{m_{g,i}}{m_g} = \frac{\rho_{g,i} V_g}{\rho_g V_g} = \frac{\rho_{g,i}}{\sum_{k=1}^{N_g} \rho_{g,k}}, \quad \text{and} \quad \sum_{k=1}^{N_g} y_{g,k} = 1 \tag{2.5}$$

where $m_{g,i}$ is the mass of component i in the gas phase.

The concept of mole fraction may be used in the derivation of gas mixture transport models. The mole fraction of gas species k is defined as:

$$\chi_{g,k} = \frac{\frac{y_{g,k}}{W_{g,k}}}{\sum_{m=1}^{N_g} \frac{y_{g,m}}{W_{g,m}}} \tag{2.6}$$

where $W_{g,k}$ is the molecular weight of gas species k.

2.1.4 Mixture Density and Mixture Enthalpy

The general definitions of gas density and liquid density are assumed to be functions of mass fractions, pressure and temperature, and are written as:

$$\rho_g = \rho_g(y_{g,i}, p, T), \quad \text{or } \rho_l = \rho_g(y_{l,j}, p, T). \tag{2.7}$$

The mixture density (Eq.2.2) in general statement then can be written as:

$$\rho = \alpha_g \rho_g(y_{g,i}, p, T) + \alpha_g \rho_l(y_{l,j}, p, T), \quad \frac{1}{\rho} = \frac{Y_g}{\rho_g(y_{g,i}, p, T)} + \frac{Y_l}{\rho_l(y_{l,j}, p, T)} \tag{2.8}$$

The mixture enthalpy can be written as:

$$h = Y_g h_g(y_{g,i}, p, T) + Y_l h_l(y_{l,j}, p, T), \quad \rho h = \rho_g \alpha_g h_g(y_{g,i}, p, T) + \rho_l \alpha_l h_l(y_{l,j}, p, T). \tag{2.9}$$

General procedures for deriving two-phase flow equations may be found in Ref. [29].

2.1.5 Mass-Averaged Velocity

There are several ways to define the mixture velocity. In our two-phase mixture system, we choose a mass-averaged velocity. It is defined as a mass-fraction weighted average of gas phase velocity and liquid phase velocity. It can be written as:

$$u_i = \left(\rho_g \alpha_g u_{ig} + \rho_l \alpha_l u_{il}\right) / \rho = Y_g u_{ig} + Y_l u_{il}, \tag{2.10}$$

where u_{ig} is the velocity of gas phase and u_{il} is the velocity of liquid phase in index notation. Thus, considering Eq. 2.10, u_{ig} and u_{il} can be expressed as

$$\begin{array}{rcccl} u_{ig} & = & u_i + u_{ig} - u_i & = & u_i + Y_l u_{ir}, \\ u_{il} & = & u_i + u_{il} - u_i & = & u_i - Y_g u_{ir}, \end{array} \tag{2.11}$$

where u_{ir} is the relative velocity between two phases, $u_{ir} = u_{ig} - u_{il}$. If $u_{ir} = 0$, then we have $u_{ig} = u_{il} = u_i$. This is called kinematic equilibrium. We will assume the mixture flow is in kinematic equilibrium during most of our simulations.

2.2 Governing Equations for the Mixture Model

2.2.1 Derivation of the Mixture Equations

The Navier-Stokes equations are assumed to govern the dynamics of the compressible, multi-component, two-phase fluids. Isothermal flow is assumed in the injector simulations, while thermal non-equilibrium flow is assumed in the crossflow simulation. Turbulence effects are incorporated using Menter's hybrid k-ω/k-ϵ model [30; 31], along with Boussinesq/gradient-diffusion closure hypotheses. In the two-phase mixture system, we suppose there are N_g components in gas phase and one component (water) in liquid phase. If kinematic equilibrium and thermal equilibrium are assumed, then $N_g - 1$ continuity equations for the gas phase, one phasic continuity equation, one mixture continuity equation, three mixture momentum equations, and one mixture energy equation will be solved. In this section, a simple mixture equation set is derived. Turbulence modeling and diffusion terms will be implemented later.

In the derivation of the two-phase mixture model, mass-averaged velocities are utilized. For instance, the two phasic continuity equations can be expressed as:

$$\begin{array}{rcccl} \dfrac{\partial(\rho Y_g)}{\partial t} & + & \dfrac{\partial(\rho Y_g u_{ig})}{\partial x_i} & = & 0, \\ \dfrac{\partial(\rho Y_l)}{\partial t} & + & \dfrac{\partial(\rho Y_l u_{il})}{\partial x_i} & = & 0, \end{array} \tag{2.12}$$

We sum up these two equations, introducing the mixture density and the mass-averaged velocity, to get the mixture continuity equation,

$$\frac{\partial(\rho Y_g + \rho Y_l)}{\partial t} + \frac{\partial(\rho Y_g u_{ig} + \rho Y_l u_{il})}{\partial x_i} = \frac{\partial \rho}{\partial t} + \frac{\partial(\rho u_i)}{\partial x_i} = 0. \tag{2.13}$$

Similarly, the mixture momentum equations can be derived as:

$$\frac{\partial(\rho u_i)}{\partial t} + \frac{\partial}{\partial x_i}(\rho u_i u_j + \rho Y_g Y_l u_{ir} u_{jr} + \delta_{ij} p - t_{ij}) = 0. \tag{2.14}$$

The kinematic equilibrium drift-flux model is used to relate the relative velocities to other variables. This closure assumes that $u_{ig} = u_{il}$, or $u_{ir} = 0$. It means that the momentum transfer between phases is fast enough so that velocities of both phases become the same very quickly. Thus, Eq. 2.14 can be simplified as:

$$\frac{\partial(\rho u_i)}{\partial t} + \frac{\partial}{\partial x_i}(\rho u_i u_j + \delta_{ij} p - t_{ij}) = 0. \tag{2.15}$$

We also assume that all phases are in thermal equilibrium, which means that the two phases have the common temperature. Having these assumptions, we now solve only one energy equation for the mixture system. It can be expressed as:

$$\frac{\partial(\rho H - p)}{\partial t} + \frac{\partial}{\partial x_i}(\rho H u_i - u_j t_{ij} + q_i) = 0. \tag{2.16}$$

The stress tensor, heat flux, and total enthalpy per unit mass are given as follows:

$$\begin{aligned} t_{ij} &= \mu \left(\frac{\partial u_i}{\partial x_j} + \frac{\partial u_j}{\partial x_i} - \frac{2}{3}\delta_{ij} \frac{\partial u_k}{\partial x_k} \right) \\ q_i &= -\lambda \frac{\partial T}{\partial x_i} \\ H &= h + \frac{1}{2} u_i u_i \end{aligned} \tag{2.17}$$

where μ is the mixture viscosity, λ is the mixture thermal conductivity, and h is the mixture enthalpy per unit mass. These mixture thermodynamic and transport properties will be detailed in Section 2.3.

2.2.2 Vector form of the Conservation Equations

Including gravity and surface tension, the governing equations can be written in strong conservation law, vector form for Cartesian coordinates as:

$$\frac{\partial \mathbf{U}}{\partial t} + \frac{\partial (\mathbf{E} - \mathbf{E_v})}{\partial x} + \frac{\partial (\mathbf{F} - \mathbf{F_v})}{\partial y} + \frac{\partial (\mathbf{G} - \mathbf{G_v})}{\partial z} = \mathbf{S} \tag{2.18}$$

where $\mathbf{U}$ is the vector of conservative variables, $\mathbf{E}$, $\mathbf{F}$ and $\mathbf{G}$ are the inviscid fluxes, $\mathbf{E_v}$, $\mathbf{F_v}$ and $\mathbf{G_v}$ are the viscous fluxes, and $\mathbf{S}$ is the vector of source terms, expressed separately as

$$\mathbf{U} = \begin{bmatrix} \rho y_{g,1} Y_g \\ \vdots \\ \rho y_{g,N_g-1} Y_g \\ \rho Y_g \\ \rho \\ \rho u \\ \rho v \\ \rho w \\ \rho H - p \end{bmatrix}, \tag{2.19}$$

$$\mathbf{E} = \begin{bmatrix} \rho y_{g,1} Y_g u \\ \vdots \\ \rho y_{g,N_g-1} Y_g u \\ \rho Y_g u \\ \rho u \\ \rho u^2 + p \\ \rho v u \\ \rho w u \\ \rho H u \end{bmatrix}, \mathbf{F} = \begin{bmatrix} \rho y_{g,1} Y_g v \\ \vdots \\ \rho y_{g,N_g-1} Y_g v \\ \rho Y_g v \\ \rho v \\ \rho u v \\ \rho v^2 + p \\ \rho w v \\ \rho H v \end{bmatrix}, \mathbf{G} = \begin{bmatrix} \rho y_{g,1} Y_g w \\ \vdots \\ \rho y_{g,N_g-1} Y_g w \\ \rho Y_g w \\ \rho w \\ \rho u w \\ \rho v w \\ \rho w^2 + p \\ \rho H w \end{bmatrix}, \tag{2.20}$$

$$\mathbf{E_v} = \begin{bmatrix} -\rho y_{g,1} Y_g u_{d,1} \\ \vdots \\ -\rho y_{g,N_g-1} Y_g u_{d,N_g-1} \\ -\rho Y_g Y_l u_r \\ 0 \\ t_{xx} \\ t_{yx} \\ t_{zx} \\ u_i t_{ix} - q_x \end{bmatrix}, \mathbf{F_v} = \begin{bmatrix} -\rho y_{g,1} Y_g v_{d,1} \\ \vdots \\ -\rho y_{g,N_g-1} Y_g v_{d,N_g-1} \\ -\rho Y_g Y_l v_r \\ 0 \\ t_{xy} \\ t_{yy} \\ t_{zy} \\ u_i t_{iy} - q_y \end{bmatrix}, \tag{2.21}$$

$$\mathbf{G_v} = \begin{bmatrix} -\rho y_{g,1} Y_g w_{d,1} \\ \vdots \\ -\rho y_{g,N_g-1} Y_g w_{d,N_g-1} \\ -\rho Y_g Y_l w_r \\ 0 \\ t_{xz} \\ t_{yz} \\ t_{zz} \\ u_i t_{iz} - q_z \end{bmatrix}, \mathbf{S} = \begin{bmatrix} \omega_g \\ \vdots \\ 0 \\ \omega_g \\ 0 \\ \mathrm{F}_{sv,x} + \rho g \\ \mathrm{F}_{sv,y} \\ \mathrm{F}_{sv,z} \\ \mathrm{F}_{sv,x_i} u_i + \rho g u \end{bmatrix}, \tag{2.22}$$

$$\mathbf{F_{sv}} = \mathrm{F}_{sv,x}\,\vec{\mathrm{i}} + \mathrm{F}_{sv,y}\,\vec{\mathrm{j}} + \mathrm{F}_{sv,z}\,\vec{\mathrm{k}}, \tag{2.23}$$

where $u_{d,i}$, $v_{d,i}$, $w_{d,i}$ are diffusion velocities for component i in gas phase, and $\mathbf{F_{sv}}$ is the surface tension force between gas phase and liquid phase. The gravity force is assumed to be aligned with the x direction. In Eq. 2.21 and Eq. 2.22, index notation is used to simplify the formulations. ω_g is the gas source term from a mass-exchange model for conversion of liquid water to vapor [32] and it can be expressed as:

$$\omega_g = C_{\mathrm{Prod}} \left(\rho_g \alpha_l \max(0, p_{sat} - p) - \frac{C_{\mathrm{Dest}}}{C_{\mathrm{Prod}}} \rho_g \alpha_g \alpha_l^2 \right), \; C_{\mathrm{Prod}} = 100, \; \frac{C_{\mathrm{Dest}}}{C_{\mathrm{Prod}}} = 0.01, \tag{2.24}$$

where p_{sat} is the saturation pressure. This model is necessary in the initial phases of the injector simulation as the liquid water jet expands rapidly into the external air.

2.3 Thermodynamic Relations

2.3.1 Thermodynamic Properties for Gas Phase

For the gas phase, the ideal gas state equation is used to get a relation between pressure, temperature and gas density, which is given as

$$\rho_g = \rho_g(p, T) = \frac{p}{\mathcal{R}_{mix} T}, \quad \mathcal{R}_{mix} = \sum_{k=1}^{N_g} \frac{y_{g,k}}{W_{g,k}} \mathcal{R}, \tag{2.25}$$

where $\mathcal{R}_{mix}$, the mixture value for the specific gas constant, is a weighted average of the individual specific gas constants of the constituent components at constant pressure, and $\mathcal{R}$ is the universal gas constant.

The specific heat at constant pressure and enthalpy of gas phase are defined as:

$$C_{p,g} = \sum_{k=1}^{N_g} y_{g,k} C_{p,k}, \quad h_g = \sum_{k=1}^{N_g} y_{g,k} h_{g,k}, \tag{2.26}$$

where $C_{p,k}$ and $h_{g,k}$ are the specific heat and the enthalpy of gas species k, respectively. These properties are given by polynomial curve-fits:

$$\begin{aligned} C_{p,k} &= \frac{\mathcal{R}}{W_{g,k}} \left(a_{1,k} + a_{2,k}T + a_{3,k}T^2 + a_{4,k}T^3 + a_{5,k}T^4 \right), \\ h_{g,k} &= \frac{\mathcal{R}}{W_{g,k}} T \left(a_{1,k} + \frac{1}{2}a_{2,k}T + \frac{1}{3}a_{3,k}T^2 + \frac{1}{4}a_{4,k}T^3 + \frac{1}{5}a_{5,k}T^4 + \frac{b_{1,k}}{T} \right), \end{aligned} \tag{2.27}$$

where the coefficients $a_{i,k}$ $(i = 1, \ldots, 5)$ and $b_{1,k}$ are obtained from McBride, *et al.* [33]

The molecular viscosity of each gas species, $\mu_{g,i}$, is determined as follows from Sutherland's formula:

$$\frac{\mu_{g,i}}{\mu_{0,i}} = \left(\frac{T}{T_{0,i}} \right)^{\frac{3}{2}} \frac{T_{0,i} + S_i}{T + S_i} \tag{2.28}$$

where the constants of gas species i, $\mu_{0,i}$, $T_{0,i}$ and S_i, are given in Table 2.1.

Table 2.1: Constants for molecular transport of gas

Species i	Name	$\mu_{0,i}$	$T_{0,i}$	S_i
1	H_2O	1.703×10^{-5}	273.1	138.6
2	N_2	1.663×10^{-5}	273.1	106.7
3	O_2	1.919×10^{-5}	273.1	138.9

The gas mixture molecular viscosity is then determined by Wilke's mixing rule [34]:

$$\mu_g = \sum_{i=1}^{N_g} \frac{\chi_{g,i}\mu_{g,i}}{\sum_{j=1}^{N_g} \chi_{g,j}\phi_{ij}}, \quad \phi_{ij} = \frac{\left[1 + \left(\frac{\mu_{g,i}}{\mu_{g,j}} \right)^{\frac{1}{2}} \left(\frac{W_{g,j}}{W_{g,i}} \right)^{\frac{1}{4}} \right]^2}{\sqrt{8} \left(1 + \frac{W_{g,i}}{W_{g,j}} \right)^{\frac{1}{2}}} \tag{2.29}$$

The molecular thermal conductivity of gas mixture, λ_g, is determined by the

Prandtl number as follows:

$$\lambda_g = \frac{C_{p,g}\mu_g}{\mathrm{Pr}}, \tag{2.30}$$

where the Prandtl number, Pr, is chosen to be 0.72 in the current work.

The molecular diffusion velocity of gas species i, $u_{d,i,j}$, is expressed using Fick's law as $u_{d,i,j} = -\dfrac{\mathcal{D}_i}{y_{g,i}}\dfrac{\partial y_{g,i}}{\partial x_j}$, where $\mathcal{D}_i$ represents the diffusion coefficient for gas species i. Fick's law can be rewritten by way of the Schmidt number ($\mathrm{Sc} = \dfrac{\mu}{\rho Y_g \mathcal{D}}$),

$$\rho y_{g,i} Y_g u_{d,i,j} = -\frac{\mu}{\mathrm{Sc}}\frac{\partial y_{g,i}}{\partial x_j}. \tag{2.31}$$

The Schmidt number is assumed to be 0.5 for all gas phase species. The mass-diffusion term of gas mixture, $-\rho Y_g Y_l u_{r,i}$ is modeled using gradient-diffusion methods as

$$-\rho Y_g Y_l u_{r,i} = -\rho Y_g Y_l (u_{g,i} - u_{l,i}) \approx C\mu_t \frac{\partial Y_g}{\partial x_i} \tag{2.32}$$

with C equal to a constant and μ_t equal to the eddy viscosity.

2.3.2 Thermodynamic Properties for Liquid Phase

The generalized Tait equation of state is used to describe the relationship among the pressure, the temperature, and the liquid density for the liquid. It is written as [35]:

$$\frac{\rho_l}{\rho_{l,sat}} = \left(1 + \frac{p - p_{sat}}{3.0 \times 10^8}\right)^{\frac{1}{7}}, \tag{2.33}$$

where p_{sat} is the saturation pressure, and $\rho_{l,sat}$ is the saturation density for liquid. These saturation properties are given in Ref. [36]:

$$\ln\frac{p_{sat}}{p_c} = \frac{T_c}{T}\left(a_1\theta + a_2\theta^{1.5} + a_3\theta^3 + a_4\theta^{3.5} + a_5\theta^4 + a_6\theta^{7.5}\right), \tag{2.34}$$

$$\frac{\rho_{l,sat}}{\rho_c} = 1 + b_1\theta^{\frac{1}{3}} + b_2\theta^{\frac{2}{3}} + b_3\theta^{\frac{5}{3}} + b_4\theta^{\frac{16}{3}} + b_5\theta^{\frac{43}{3}} + b_6\theta^{\frac{110}{3}}, \tag{2.35}$$

where $\theta = 1 - \frac{T}{T_c}$, and p_c, T_c and ρ_c represent the critical pressure, temperature,

and density, respectively. The critical conditions for water are $p_c = 22.64 \times 10^5$ Pa, $T_c = 647.14$ K, and $\rho_c = 332$ kg/m^3. The coefficients a_i and b_i are given in Ref. [36].

The enthalpy of the liquid phase (water) is determined by its departure from water vapor state enthalpy as [35]:

$$h_l - h_{g,1} = (C_{v,l} - C_{v,g})(T - T_0) - h_{lh} + \frac{p}{\rho_l} - \frac{\mathcal{R}}{W_{g,1}}T \tag{2.36}$$

where $h_{g,1}$ and $W_{g,1}$ are the enthalpy and the molecular weight of gas species 1 (water vapor) respectively, h_{lh} is the latent heat of water vapor, and other constants are listed in Table 2.2.

Table 2.2: Constants for enthalpy departure of liquid water

Constant	$C_{v,l}$	$C_{v,g}$	T_0	h_{lh}
Value	4180.0 J/kg K	1410.8 J/kg K	273.15 K	2502789.4 J/kg

The viscosity and thermal conductivity of liquid phase (water) are determined by following equations [37]:

$$\begin{aligned} \mu_l &= e^{c_1 + \frac{c_2}{c_3 - T}}, \\ \lambda_l &= d_1 + d_2 T + d_3 T^2, \end{aligned} \tag{2.37}$$

where the coefficients, c_i and d_i, are given in Table 2.3 [37].

Table 2.3: Coefficients for transport quantities of liquid water

Index i	c_i	d_i
1	-10.4349	-0.7676
2	-507.881	7.5390×10^{-3}
3	149.390	-9.8250×10^{-6}

2.3.3 Phasic Mixing Rules

The bulk density and mixture enthalpy are defined in Eq. 2.8 and Eq. 2.9,

$$\frac{1}{\rho} = \frac{Y_g}{\rho_g} + \frac{Y_l}{\rho_l}, \quad h = Y_g h_g + Y_l h_l. \tag{2.38}$$

The mixture viscosity and the mixture thermal conductivity are defined as:

$$\mu = \alpha_g \mu_g + \alpha_l \mu_l, \tag{2.39}$$

$$\lambda = \alpha_g \lambda_g + \alpha_l \lambda_l, \tag{2.40}$$

The sound speed for the mixture, derived in Appendix A, is a function of thermodynamic derivatives, such as ρ_T, ρ_p, h_T and h_p:

$$a^2 = \frac{\rho h_T}{\rho \rho_p h_T - \rho \rho_T h_p + \rho_T} \tag{2.41}$$

These thermodynamic derivatives can be obtained by differentiating Eq. 2.38 with respect to p and T:

$$\begin{aligned} \rho_p &= \rho^2 \left(\frac{Y_g}{{\rho_g}^2} \frac{\partial \rho_g}{\partial p} + \frac{1 - Y_g}{{\rho_l}^2} \frac{\partial \rho_l}{\partial p} \right), \\ \rho_T &= \rho^2 \left(\frac{Y_g}{{\rho_g}^2} \frac{\partial \rho_g}{\partial T} + \frac{1 - Y_g}{{\rho_l}^2} \frac{\partial \rho_l}{\partial T} \right), \\ h_p &= (1 - Y_g) \frac{\partial h_l}{\partial p}, \\ h_T &= Y_g \frac{\partial h_g}{\partial T} + (1 - Y_g) \frac{\partial h_l}{\partial T}. \end{aligned} \tag{2.42}$$

If the flow is assumed isothermal, then the sound speed a is simplified as

$$\frac{1}{a^2} = \rho_p = \rho^2 \left(\frac{Y_g}{{\rho_g}^2} \frac{\partial \rho_g}{\partial p} + \frac{1 - Y_g}{{\rho_l}^2} \frac{\partial \rho_l}{\partial p} \right), \tag{2.43}$$

and the energy equation in the governing equations (Eq.2.18) is replaced by the constraint that the temperature holds constant $T = T_\infty$.

2.4 Reynolds Averaging and Favre Averaging

Since the computational grid is not sufficient to resolve turbulent fluctuations of the various flow properties, we use Reynolds-Averaged Navier-Stokes (RANS) [38] approach to average certain flow properties to avoid fluctuating parts occurring in the set of governing equations.

In this study, Reynolds averaging is a time average over the time interval $(t, t+T)$. The time average of an instantaneous flow variable, $f(\mathbf{x}, t)$, is defined by

$$\overline{f}(\mathbf{x}) = \frac{1}{T}\int_{t}^{t+T} f(\mathbf{x}, t)\mathrm{d}t, \tag{2.44}$$

where the time interval T is much longer than the time scale of turbulent fluctuations but is much smaller than the time scale of the slow variations in the flow. Thus, the flow variable can be decomposed into mean part, $\overline{f}$, and fluctuating component, f', as follows

$$f = \overline{f} + f'. \tag{2.45}$$

Reynolds averaging the whole equation set will increase the complexity of establishing suitable closure modelings. This problem can be simplified by introducing Favre averaging [38], which is defined by $\widetilde{f} = \dfrac{\overline{\rho f}}{\overline{\rho}}$. Therefore, the decomposition can be rewritten in terms of a Favre-averaged part,$\widetilde{f}$, and a Favre-fluctuating part, f'' as follows

$$f = \widetilde{f} + f''. \tag{2.46}$$

Applying Reynolds and Favre averaging procedures to the Navier-Stokes equations we can obtain the RANS equations:

$$\frac{\partial(\overline{\rho}\widetilde{Y}_{g,k}\widetilde{Y}_g)}{\partial t} + \frac{\partial}{\partial x_i}\left(\overline{\rho}\widetilde{Y}_{g,k}\widetilde{Y}_g\widetilde{u}_i - (\overline{\rho}\widetilde{Y}_{g,k}\widetilde{Y}_g\widetilde{u}_{d,i} + \Gamma_{k,i})\right) = 0, \tag{2.47}$$

$$\frac{\partial(\overline{\rho}\widetilde{Y}_g)}{\partial t} + \frac{\partial}{\partial x_i}\left(\overline{\rho}\widetilde{Y}_g\widetilde{u}_i - (\overline{\rho}\widetilde{Y}_g\widetilde{Y}_l\widetilde{u}_{r,i} + \overline{\rho Y_g'' Y_l u_{r,i}''})\right) = 0, \tag{2.48}$$

$$\frac{\partial\overline{\rho}}{\partial t} + \frac{\partial(\overline{\rho}\widetilde{u}_i)}{\partial x_i} = 0, \tag{2.49}$$

$$\frac{\partial(\overline{\rho}\widetilde{u}_i)}{\partial t} + \frac{\partial}{\partial x_i}\left(\overline{\rho}\widetilde{u}_i\widetilde{u}_j + \delta_{ij}\overline{p} - (\overline{t}_{ij} + \tau_{i,j})\right) = 0, \tag{2.50}$$

$$\frac{\partial(\overline{\rho}\widetilde{H} - \overline{p})}{\partial t} + \frac{\partial}{\partial x_i}\left(\overline{\rho}\widetilde{H}\widetilde{u}_i - \widetilde{u}_j(\overline{t}_{ij} + \tau_{ij}) + (\overline{q}_i + q_{t,i})\right) = 0, \tag{2.51}$$

$$
\begin{aligned}
\text{where} \qquad \Gamma_{k,i} &= \overline{\rho Y''_{g,k} Y''_g u''_{d,i}}, && (2.52)\\
\bar{t}_{ij} &= \mu(\widetilde{T}) \left(\frac{\partial \widetilde{u}_i}{\partial x_j} + \frac{\partial \widetilde{u}_j}{\partial x_i} - \frac{2}{3}\delta_{ij} \frac{\partial \widetilde{u}_k}{\partial x_k} \right), && (2.53)\\
\tau_{i,j} &= -\overline{\rho u''_i u''_j}, && (2.54)\\
\overline{q}_i &= -\lambda(\widetilde{T}) \frac{\partial \widetilde{T}}{\partial x_i}, && (2.55)\\
q_{t,i} &= \overline{\rho u''_i h''}. && (2.56)
\end{aligned}
$$

The turbulent diffusion tensor, $\Gamma_{k,i}$ is expressed as

$$
\Gamma_{k,i} = \overline{\rho Y''_{g,k} Y''_g u''_{d,i}} = -\frac{\mu_t}{\mathrm{Sc}_t} \frac{\partial \widetilde{Y}_{g,k}}{\partial x_i}, \tag{2.57}
$$

where the turbulent Schmidt number Sc_t, is assumed to be 0.5 in the current study, and the eddy viscosity, μ_t, will be obtained from turbulent model equations described later. The Reynolds-stress tensor, $\tau_{i,j}$, and the turbulent heat-flux vector, $q_{t,i}$, are modeled using the Boussinesq eddy viscosity approximation and the gradient-diffusion approximation:

$$
\begin{aligned}
\tau_{ij} &= \mu_t(\widetilde{T}) \left(\frac{\partial \widetilde{u}_i}{\partial x_j} + \frac{\partial \widetilde{u}_j}{\partial x_i} - \tfrac{2}{3}\delta_{ij} \frac{\partial \widetilde{u}_k}{\partial x_k} \right),\\
q_{t,i} &= \frac{c_p \mu_t}{\mathrm{Pr}_t} \frac{\partial \widetilde{T}}{\partial x_i},
\end{aligned} \tag{2.58}
$$

where the turbulent Prandtl number, Pr_t, is assumed to be 0.9 in this work.

2.5 Coordinate Transformation

The governing equations may be written for a generalized coordinate system (ξ, η, ζ) according to the transformation $(x, y, z) \mapsto (\xi, \eta, \zeta)$. Using the chain rule of partial differentiation, the governing equations can be written as:

$$
\frac{1}{J}\frac{\partial \mathbf{U}}{\partial t} + \frac{\partial (\mathbf{E} - \mathbf{E_v})}{\partial \xi} + \frac{\partial (\mathbf{F} - \mathbf{F_v})}{\partial \eta} + \frac{\partial (\mathbf{G} - \mathbf{G_v})}{\partial \zeta} = \mathbf{S} \tag{2.59}
$$

where J is the Jacobian of the transformation (see Ref. [39]), $\mathbf{U}$ is the vector of conservative variables, $\mathbf{E}$, $\mathbf{F}$ and $\mathbf{G}$ are the inviscid fluxes, $\mathbf{E_v}$, $\mathbf{F_v}$ and $\mathbf{G_v}$ are the viscous fluxes, and $\mathbf{S}$ is the vector of source terms, expressed separately as

$$\mathbf{U} = \begin{bmatrix} \overline{\rho}\widetilde{Y}_{g,1}\widetilde{Y}_g \\ \vdots \\ \overline{\rho}\widetilde{Y}_{g,N_g-1}\widetilde{Y}_g \\ \overline{\rho}\widetilde{Y}_g \\ \overline{\rho} \\ \overline{\rho}\widetilde{u} \\ \overline{\rho}\widetilde{v} \\ \overline{\rho}\widetilde{w} \\ \overline{\rho}\widetilde{H} - \overline{p} \end{bmatrix}, \tag{2.60}$$

$$\mathbf{E} = \frac{1}{J}\begin{bmatrix} \overline{\rho}\widetilde{Y}_{g,1}\widetilde{Y}_g\mathcal{U} \\ \vdots \\ \overline{\rho}\widetilde{Y}_{g,N_g-1}\widetilde{Y}_g\mathcal{U} \\ \overline{\rho}\widetilde{Y}_g\mathcal{U} \\ \overline{\rho}\mathcal{U} \\ \overline{\rho}\widetilde{u}\mathcal{U} + \xi_x\overline{p} \\ \overline{\rho}\widetilde{v}\mathcal{U} + \xi_y\overline{p} \\ \overline{\rho}\widetilde{w}\mathcal{U} + \xi_z\overline{p} \\ \overline{\rho}\widetilde{H}\mathcal{U} \end{bmatrix}, \mathbf{F} = \frac{1}{J}\begin{bmatrix} \overline{\rho}\widetilde{Y}_{g,1}\widetilde{Y}_g\mathcal{V} \\ \vdots \\ \overline{\rho}\widetilde{Y}_{g,N_g-1}\widetilde{Y}_g\mathcal{V} \\ \overline{\rho}\widetilde{Y}_g\mathcal{V} \\ \overline{\rho}\mathcal{V} \\ \overline{\rho}\widetilde{u}\mathcal{V} + \eta_x\overline{p} \\ \overline{\rho}\widetilde{v}\mathcal{V} + \eta_y\overline{p} \\ \overline{\rho}\widetilde{w}\mathcal{V} + \eta_z\overline{p} \\ \overline{\rho}\widetilde{H}\mathcal{V} \end{bmatrix}, \mathbf{G} = \frac{1}{J}\begin{bmatrix} \overline{\rho}\widetilde{Y}_{g,1}\widetilde{Y}_g\mathcal{W} \\ \vdots \\ \overline{\rho}\widetilde{Y}_{g,N_g-1}\widetilde{Y}_g\mathcal{W} \\ \overline{\rho}\widetilde{Y}_g\mathcal{W} \\ \overline{\rho}\mathcal{W} \\ \overline{\rho}\widetilde{u}\mathcal{W} + \zeta_x\overline{p} \\ \overline{\rho}\widetilde{v}\mathcal{W} + \zeta_y\overline{p} \\ \overline{\rho}\widetilde{w}\mathcal{W} + \zeta_z\overline{p} \\ \overline{\rho}\widetilde{H}\mathcal{W} \end{bmatrix}, \tag{2.61}$$

$$\mathbf{E_v} = \frac{1}{J}\begin{bmatrix} -\overline{\rho}\widetilde{Y}_{g,1}\widetilde{Y}_g\mathcal{U}_{d,1} \\ \vdots \\ -\overline{\rho}\widetilde{Y}_{g,N_g-1}\widetilde{Y}_g\mathcal{U}_{d,N_g-1} \\ -\overline{\rho}\widetilde{Y}_g\widetilde{Y}_l\mathcal{U}_r \\ 0 \\ \xi_{x_i}(\overline{t}_{i1} + \tau_{i1}) \\ \xi_{x_i}(\overline{t}_{i2} + \tau_{i2}) \\ \xi_{x_i}(\overline{t}_{i3} + \tau_{i3}) \\ \xi_{x_i}[\widetilde{u}_j(\overline{t}_{ij} + \tau_{ij}) - (\overline{q}_i + q_{t,i})] \end{bmatrix}, \mathbf{F_v} = \frac{1}{J}\begin{bmatrix} -\overline{\rho}\widetilde{Y}_{g,1}\widetilde{Y}_g\mathcal{V}_{d,1} \\ \vdots \\ -\overline{\rho}\widetilde{Y}_{g,N_g-1}\widetilde{Y}_g\mathcal{V}_{d,N_g-1} \\ -\overline{\rho}\widetilde{Y}_g\widetilde{Y}_l\mathcal{V}_r \\ 0 \\ \eta_{x_i}(\overline{t}_{i1} + \tau_{i1}) \\ \eta_{x_i}(\overline{t}_{i2} + \tau_{i2}) \\ \eta_{x_i}(\overline{t}_{i3} + \tau_{i3}) \\ \eta_{x_i}[\widetilde{u}_j(\overline{t}_{ij} + \tau_{ij}) - (\overline{q}_i + q_{t,i})] \end{bmatrix}, \tag{2.62}$$

$$\mathbf{G_v} = \frac{1}{J}\begin{bmatrix} -\overline{\rho}\widetilde{Y}_{g,1}\widetilde{Y}_g\mathcal{W}_{d,1} \\ \vdots \\ -\overline{\rho}\widetilde{Y}_{g,N_g-1}\widetilde{Y}_g\mathcal{W}_{d,N_g-1} \\ -\overline{\rho}\widetilde{Y}_g\widetilde{Y}_l\mathcal{W}_r \\ 0 \\ \zeta_{x_i}(\overline{t}_{i1}+\tau_{i1}) \\ \zeta_{x_i}(\overline{t}_{i2}+\tau_{i2}) \\ \zeta_{x_i}(\overline{t}_{i3}+\tau_{i3}) \\ \zeta_{x_i}[\widetilde{u}_j(\overline{t}_{ij}+\tau_{ij})-(\overline{q}_i+q_{t,i})] \end{bmatrix}, \mathbf{S} = \frac{1}{J}\begin{bmatrix} \omega_g \\ \vdots \\ 0 \\ \omega_g \\ 0 \\ \mathrm{F}_{sv,\xi}+\overline{\rho}g \\ \mathrm{F}_{sv,\eta} \\ \mathrm{F}_{sv,\zeta} \\ \mathrm{F}_{sv,\xi_i}\widetilde{u}_i+\overline{\rho}g\widetilde{u} \end{bmatrix}, \tag{2.63}$$

$$\mathbf{F_{sv}} = \mathrm{F}_{sv,\xi}\,\vec{\xi} + \mathrm{F}_{sv,\eta}\,\vec{\eta} + \mathrm{F}_{sv,\zeta}\,\vec{\zeta}. \tag{2.64}$$

In the above development, $\mathcal{U}$, $\mathcal{V}$, and $\mathcal{W}$ are the contravariant velocity components, $\mathcal{U}_{d,i}$, $\mathcal{V}_{d,i}$, and $\mathcal{W}_{d,i}$ are the contravariant diffusion velocities for component i in gas phase, and $\mathcal{U}_r$, $\mathcal{V}_r$, and $\mathcal{W}_r$ are the contravariant relative velocity components. They all have the same form as

$$\begin{aligned} (\mathcal{U},\mathcal{U}_{d,i},\mathcal{U}_r) &\equiv \xi_x(\widetilde{u},\widetilde{u}_{d,i},\widetilde{u}_r)+\xi_y(\widetilde{v},\widetilde{v}_{d,i},\widetilde{v}_r)+\xi_z(\widetilde{w},\widetilde{w}_{d,i},\widetilde{w}_r) \\ (\mathcal{V},\mathcal{V}_{d,i},\mathcal{V}_r) &\equiv \eta_x(\widetilde{u},\widetilde{u}_{d,i},\widetilde{u}_r)+\eta_y(\widetilde{v},\widetilde{v}_{d,i},\widetilde{v}_r)+\eta_z(\widetilde{w},\widetilde{w}_{d,i},\widetilde{w}_r) \\ (\mathcal{W},\mathcal{W}_{d,i},\mathcal{W}_r) &\equiv \zeta_x(\widetilde{u},\widetilde{u}_{d,i},\widetilde{u}_r)+\zeta_y(\widetilde{v},\widetilde{v}_{d,i},\widetilde{v}_r)+\zeta_z(\widetilde{w},\widetilde{w}_{d,i},\widetilde{w}_r). \end{aligned} \tag{2.65}$$

2.6 Turbulence Modeling

The averaging procedures performed on the governing equations introduced three additional terms: the Reynolds-stress tensor, turbulent heat-flux vector, and the turbulent diffusion tensor. All these terms are dependent on the turbulent viscosity, μ_t, or the turbulent kinematic eddy viscosity, $\nu_t = \dfrac{\mu_t}{\rho}$. In this work, the eddy viscosity is calculated using Menter's hybrid k-ω/k-ϵ shear stress transport (SST) model [30; 31].

The transport equations for the turbulence kinetic energy, k, and the specific

dissipation rate, ω, are given by

$$\frac{\partial(\rho k)}{\partial t} + \frac{\partial(\rho k u_j)}{\partial x_j} = \mu_t \Omega^2 - \beta^* \rho \omega k + \frac{\partial}{\partial x_j}\left[(\mu + \sigma_k \mu_t)\frac{\partial k}{\partial x_j}\right], \tag{2.66}$$

$$\begin{aligned}\frac{\partial(\rho \omega)}{\partial t} + \frac{\partial(\rho \omega u_j)}{\partial x_j} &= \gamma \rho \Omega^2 - \beta \rho \omega^2 + \frac{\partial}{\partial x_j}\left[(\mu + \sigma_\omega \mu_t)\frac{\partial \omega}{\partial x_j}\right] \\ &\quad + 2(1 - F_1)\rho \sigma_{\omega 2}\frac{1}{\omega}\frac{\partial k}{\partial x_j}\frac{\partial \omega}{\partial x_j}.\end{aligned} \tag{2.67}$$

where Ω is the magnitude of the vorticity vector, and any constant in Menter's model, ϕ, is blended by the blending function F_1

$$\phi = F_1 \phi_1 + (1 - F_1)\phi_2 \tag{2.68}$$

where the ϕ_1 constants are from the k-ω equation:

$$\begin{aligned}&\sigma_{k1} = 0.85, \quad \sigma_{\omega 1} = 0.5, \quad \beta_1 = 0.075, \\ &\beta^* = 0.09, \quad \kappa = 0.41, \quad \gamma_1 = \frac{\beta_1}{\beta^*} - \frac{\sigma_{\omega 1}\kappa^2}{\sqrt{\beta^*}}\end{aligned} \tag{2.69}$$

and the ϕ_1 constants are from the k-ϵ equation:

$$\begin{aligned}&\sigma_{k2} = 1.0, \quad \sigma_{\omega 2} = 0.856, \quad \beta_2 = 0.0828, \\ &\beta^* = 0.09, \quad \kappa = 0.41, \quad \gamma_2 = \frac{\beta_2}{\beta^*} - \frac{\sigma_{\omega 2}\kappa^2}{\sqrt{\beta^*}}\end{aligned} \tag{2.70}$$

The blending function F_1 is defined as

$$F_1 = \tanh(\arg_1^4), \quad \arg_1 = \min\left[\max\left(\frac{\sqrt{k}}{0.09\omega y}; \frac{500\nu}{y^2\omega}\right)\frac{4\rho\sigma_{\omega 2}k}{\mathrm{CD}_{k\omega}y^2}\right] \tag{2.71}$$

where y is the distance to the nearest wall, and $\mathrm{CD}_{k\omega}$ is the positive component of the cross-diffusion term in Eq. 2.67

$$\mathrm{CD}_{k\omega} = \max\left(2\rho\sigma_{\omega 2}\frac{1}{\omega}\frac{\partial k}{\partial x_j}\frac{\partial \omega}{\partial x_j}, 10^{-20}\right) \tag{2.72}$$

The eddy viscosity is defined as:

$$\nu_t = \frac{a_1 k}{\max(a_1\omega; \Omega F_2)} \tag{2.73}$$

where $a_1 = 0.31$ and F_2 is another blending function given by

$$F_2 = \tanh(\arg_2^2), \quad \arg_2 = \max\left(2\frac{\sqrt{k}}{0.09\omega y}; \frac{500\nu}{y^2\omega}\right) \tag{2.74}$$

2.7 Interface Surface Tension

The continuum surface force (CSF) model developed by Brackbill, *et al.* [40] is selected to describe the effects of surface tension on a phase interface. This model interprets surface tension as a continuous, three-dimensional effect across an interface, rather than as a boundary value condition on the interface.

In the CSF model, the surface volume force, $\mathbf{F}_{\text{sv}}(\mathbf{x})$, for finite interfacial thickness, h, is expressed as

$$\mathbf{F}_{\text{sv}}(\mathbf{x}_{\text{s}}) = \sigma\kappa(\mathbf{x})\frac{\nabla\widetilde{c}(\mathbf{x})}{[\,c\,]}. \tag{2.75}$$

where $\sigma = 0.072$ is the surface tension coefficient, κ is the interface curvature, and c is a mollified color function. κ is calculated as $\kappa = -(\nabla \cdot \hat{n})$, where the normals are gradients of the mollified color function, $\mathbf{n}(\mathbf{x}) = \nabla\widetilde{c}(\mathbf{x})$. Thus the unit normal is $\hat{n}(\mathbf{x}) = \dfrac{\nabla\widetilde{c}(\mathbf{x})}{|\nabla\widetilde{c}(\mathbf{x})|}$. Since $\nabla\widetilde{c}$ is not zero only in the interface transition region, the surface volume force also is nonzero only in this region. The color function $\widetilde{c}$ is chosen as volume fraction of the gas phase, α_g. Thus, $[\,c\,] = [\,\alpha_g\,] = 1.0$, and Eq. 2.75 can be rewritten as:

$$\mathbf{F}_{\text{sv}}(\mathbf{x}_{\text{s}}) = -\sigma\left[\nabla \cdot \left(\frac{\nabla\alpha_g}{|\nabla\alpha_g|}\right)\right]\nabla\alpha_g, \tag{2.76}$$

or in index notation as:

$$\mathrm{F}_{sv,x_i} = -\sigma\left[\frac{\partial}{\partial x_i}\left(\frac{\dfrac{\partial\alpha_g}{\partial x_i}}{\sqrt{\dfrac{\partial\alpha_g}{\partial x_k}\dfrac{\partial\alpha_g}{\partial x_k}}}\right)\right]\frac{\partial\alpha_g}{\partial x_i}, \tag{2.77}$$

Using the chain rule, Eq. 2.77 can be transformed to generalized coordinates, and is

written as:

$$\mathrm{F}_{sv,\xi_i} = -\,\sigma\,\frac{\partial \xi_j}{\partial x_i}\frac{\partial}{\partial \xi_j}\left[\frac{\dfrac{\partial \xi_j}{\partial x_i}\dfrac{\partial \alpha_g}{\partial \xi_j}}{\sqrt{\left(\dfrac{\partial \xi_j}{\partial x_k}\dfrac{\partial \alpha_g}{\partial \xi_j}\right)\left(\dfrac{\partial \xi_j}{\partial x_k}\dfrac{\partial \alpha_g}{\partial \xi_j}\right)}}\right]\frac{\partial \xi_j}{\partial x_i}\frac{\partial \alpha_g}{\partial \xi_j}, \tag{2.78}$$

2.8 Droplet Transport Model

In the crossflow experiment, many droplet properties are measured or calculated. But not all of these properties can be calculated in the simulations with the mixture model. For example, the separate liquid droplet velocities cannot be obtained, nor can predictions of average droplet size. In order to understand more liquid properties, an Eulerian droplet transport model is implemented in this work, which decouples calculations between the two phases.

The droplet transport model is included in the crossflow simulations to get more details about effects of droplet size and velocity slip on spray penetration. In this model, one liquid mass continuity equation in conservative form, along with three liquid momentum equations discretized in divergence form, are solved in a similar matter used in the mixture model. No droplet energy equation needs to be solved since the droplet temperature in the jet exit plane is assumed to be frozen at the injector exit value. Droplet equations are solved separately from the mixture equations. As a first step, the droplet distribution is assumed to be monodisperse with an inputted diameter. Some mixture properties are held fixed during the calculations that include the droplet model, such as the mixture velocities, pressure, mixture viscosity, temperature and eddy viscosity. Some properties are allowed to vary, such as gas and liquid volume fractions, mass fractions, and mixture density. But as this is a one-way coupling, all properties changed in the droplet model calculations will not

be sent back to the mixture calculations. The equation set can be written as:

$$\frac{\partial(\rho_l \alpha_l)}{\partial t} + \nabla \cdot (\rho_l \alpha_l \mathbf{u}_l) = \nabla \cdot \left(\frac{(\mu + \mu_t)}{\mathrm{Sc}_d} \nabla Y_l \right), \tag{2.79}$$

$$\frac{\partial \mathbf{u}_l}{\partial t} + (\mathbf{u}_l \cdot \nabla)\mathbf{u}_l - \frac{\mathbf{t}_l}{\rho_l} = \beta_l \mathbf{u}_r + \mathbf{g}, \tag{2.80}$$

where the right hand side of Eq. 2.79 is a diffusion term, which is similar to that used in the mixture model, $\mathbf{t}_l$ is the liquid turbulent stress tensor, which is also similar to that used in the mixture model, and β_l is the friction coefficient, which is expressed as [41]:

$$\beta_l = \begin{cases} 150 \dfrac{\alpha_l \mu_g}{\rho_l {\alpha_g}^2 d^2} + 1.75 \dfrac{\rho_g |\mathbf{u}_r|}{\rho_l d}, & \alpha_g < 0.8, \\ \dfrac{3}{4} C_D \dfrac{\rho_g |\mathbf{u}_r|}{\rho_l d} f(\alpha_g), & \alpha_g \geqslant 0.8. \end{cases} \tag{2.81}$$

where d is the droplet diameter, $f(\alpha_g)$ is the correction function, which can be expressed as $f(\alpha_g) = {\alpha_g}^{-2.65}$. The drag coefficient, C_D, is related to the droplet Reynolds number:

$$C_D = \begin{cases} \dfrac{24}{\mathrm{Re}_d} \left(1 + 0.15 \mathrm{Re}_d^{0.687}\right), & \mathrm{Re}_d < 1000, \\ 0.44 & \mathrm{Re}_d \geqslant 1000. \end{cases} \tag{2.82}$$

$$\mathrm{Re}_d = \frac{\rho_g \alpha_g |\mathbf{u}_r| d}{\mu_g}. \tag{2.83}$$

The relative velocity, $\mathbf{u}_r$, can be calculated from the mixture velocity and liquid velocity as follows:

$$u_{ir} = u_{ig} - u_{il} = \frac{u_i - u_{il}}{Y_g}. \tag{2.84}$$

If the mixture velocities are used as droplet velocities, then the drag term will vanish due to the no-slip condition.

Chapter 3

Numerical Algorithms

In this chapter, the main algorithms required for solution of the Navier-Stokes equations are presented. These methods include a time-derivative preconditioning method, a low-diffusion upwinding method, and numerical solution of the non-linear system.

3.1 Preconditioning Method

The concept of time-derivative preconditioning [10–13; 15; 42] is now widely used in many applications to enable standard compressible gas codes to perform at very low Mach numbers. More recently, there have been several efforts designed to extend its applicability to supercritical fluids [43], flow governed by generalized equations of state [44], and two-phase flows [18; 45–47].

Conventional time marching algorithm encounters convergence difficulties at low Mach numbers because of the wide disparity in characteristic wave speeds, which are the eigenvalues of the inviscid flux Jacobian (i.e., for one-dimensional system, u and $u \pm a$). Errors present in the characteristic variables are convected out of the system at the wave speeds of the system. At low speeds, the error convected at u and errors convected at $u \pm a$ are transported at widely varying time scales. This results in poor convergence rates of traditional time marching algorithm, since stability constraints typically require the selection of finite time-step sizes. Preconditioning methods introduce pseudo time-derivatives which alter the characteristic waves (i.e., $u \pm a$) so that they propagate at speeds that are comparable in magnitude to the characteristic wave (i.e., u). This approach eliminates the stiffness in the wave speeds and make

the system well-conditioned. Since preconditioning methods can lack robustness in many situations (i.e., low speed reactive flows), it may sometimes be necessary to use implicit methods for time advancement. Another concern is that it may be necessary to specify, in general, a constant "reference velocity" as a consistent velocity scale to avoid numerical difficulties in stagnation region [18].

The system described in section 2.2.2 may be preconditioned as follows:

$$\frac{1}{J}\left(\mathbf{P}\frac{\partial \mathbf{V}}{\partial \tau}+\frac{\partial \mathbf{U}}{\partial t}\right)+\frac{\partial(\mathbf{E}-\mathbf{E_v})}{\partial \xi}+\frac{\partial(\mathbf{F}-\mathbf{F_v})}{\partial \eta}+\frac{\partial(\mathbf{G}-\mathbf{G_v})}{\partial \zeta}=\mathbf{S} \tag{3.1}$$

where τ is the pseudo time variable, and t is the physical time variable. This is called a dual-time stepping method [14; 16]. For steady-state computations, Eq. 3.1 will contain only pseudo time-derivatives. For unsteady computations, Eq. 3.1 will contain both pseudo and physical time-derivatives. In latter cases, the transient solution is advanced in physical time and pseudo time iterations are performed at each physical time step until the non-linear system is satisfied.

The preconditioning matrix, $\mathbf{P}$, is that of Weiss and Smith [12], which is a variant of the Turkel [10; 13] and and Choi-Merkle [11] preconditioners. This preconditioner may be expressed as a rank-one perturbation of the Jacobian matrix $\frac{\partial \mathbf{U}}{\partial \mathbf{V}}$:

$$\mathbf{P}=\frac{\partial \mathbf{U}}{\partial \mathbf{V}}+\Theta \vec{u}\vec{v}^{T} \tag{3.2}$$

where

$$\mathbf{V}=\begin{bmatrix} y_{g,1} \\ \vdots \\ y_{g,N_g-1} \\ Y_g \\ p \\ u \\ v \\ w \\ T \end{bmatrix}, \vec{u}=\begin{bmatrix} y_{g,1} \\ \vdots \\ y_{g,N_g-1} \\ Y_g \\ 1 \\ u \\ v \\ w \\ H \end{bmatrix}, \vec{v}=\begin{bmatrix} \partial p/\partial y_{g,1} \\ \vdots \\ \partial p/\partial y_{g,N_g-1} \\ \partial p/\partial Y_g \\ \partial p/\partial p \\ \partial p/\partial u \\ \partial p/\partial v \\ \partial p/\partial w \\ \partial p/\partial T \end{bmatrix}=\begin{bmatrix} 0 \\ \vdots \\ 0 \\ 0 \\ 1 \\ 0 \\ 0 \\ 0 \\ 0 \end{bmatrix}, \Theta=\frac{1}{V_{\text{ref}}^2}-\frac{1}{a^2}, \tag{3.3}$$

and V_{ref}^2 is a suitably defined reference velocity. The quantity a is the sound speed as defined in Appendix A. In the limit of an incompressible flow ($a^2 \to \infty$), this preconditioner reduces to a variant of Chorin's artificial compressibility method [48], while $\dfrac{\partial \mathbf{U}}{\partial \mathbf{V}}$ is recovered as $V_{\text{ref}}^2 \to a^2$. The reference velocity is usually defined as

$$V_{\text{ref}}^2 = \min\left[a^2, \max\left(|\vec{V}|^2, V_\infty^2\right)\right], \tag{3.4}$$

where $|\vec{V}|$ is the local fluid velocity magnitude, and V_∞ is a user defined cutoff velocity, which is designed to prevent singular behavior in stagnation regions. As shown in Refs. [15; 18; 49] and [50], this choice may be not adequate for low speed unsteady flows at small physical time steps. Another choice of the reference velocity for unsteady preconditioning is defined as [28; 47]

$$V_{\text{ref,un}}^2 = \min\left[a^2, \max\left(|\vec{V}|^2, V_\infty^2, \left(\frac{\sqrt{\Delta x_i^2}}{\Delta t}\right)^2\right)\right], \tag{3.5}$$

where $\sqrt{\Delta x_i^2}$ is a length scale characteristic of a cell. In the following sections, different choices for the reference velocity will be used in different parts of the interface flux in the implementations of flux-splitting method.

According to Appendix B, the eigenvalues of the flux Jacobian of Eq. 3.1 in the ξ direction, $\mathbf{P}^{-1}\dfrac{\partial \mathbf{E}}{\partial \mathbf{V}}$, are $\overline{\mathcal{U}}$ and $\overline{\mathcal{U}}' \pm a'$,

$$\overline{\mathcal{U}}' \pm a' = \frac{1 + M_{\text{ref}}^2}{2}\left[\overline{\mathcal{U}} \pm a\frac{\sqrt{\left(1 - M_{\text{ref}}^2\right)^2 M^2 + 4M_{\text{ref}}^2}}{1 + M_{\text{ref}}^2}\right], \tag{3.6}$$

$$\overline{\mathcal{U}} = \overline{\xi}_x u + \overline{\xi}_y v + \overline{\xi}_z w,\ \overline{\xi}_x = \frac{\xi_x}{|\nabla \xi|},\quad \overline{\xi}_y = \frac{\xi_y}{|\nabla \xi|},\quad \overline{\xi}_z = \frac{\xi_z}{|\nabla \xi|}, \tag{3.7}$$

where $\overline{\mathcal{U}}$ is the normal component of the contravariant velocity in the ξ direction, M_{ref} and M are the reference Mach number and the Mach number defined as:

$$M_{\text{ref}} = \frac{V_{\text{ref,un}}}{a},\quad M = \frac{\overline{\mathcal{U}}}{a}. \tag{3.8}$$

In the limit of an incompressible flow, the acoustic eigenvalues revert to

$$\overline{\mathcal{U}}' \pm a' = \frac{1}{2}\left(\overline{\mathcal{U}} \pm \sqrt{\overline{\mathcal{U}}^2 + 4V_{\text{ref}}^2}\right), \tag{3.9}$$

which scale as the reference velocity.

3.2 Flux-Splitting Scheme

The inviscid fluxes in the governing equations are discretized using low-diffusion flux-splitting scheme (LDFSS) [17; 18], which belongs to the 'AUSM-family' [51; 52]. These schemes are hybrid flux-vector/flux-difference splitting methods that combine high resolution with efficiency and compactness of formulation. The viscous and diffusive terms in the governing equations are discretized using central differences.

3.2.1 LDFSS

The version of LDFSS used in this study is valid for real fluids undergoing phase transitions [18; 28; 46]. Details regarding the original development of LDFSS may be found in Refs. [17; 53]. The algorithm is formulated as an upwinding procedure in one dimension, and then applied to three spatial dimensions. For simplicity, the derivation that follows is for the ξ direction flux only. For clarity, the accents denoting Reynolds and Favre averaged quantities are omitted in this section. The inviscid ξ direction flux $\mathbf{E}$ can be split into convective and pressure contributions:

$$\mathbf{E} = \mathbf{E}^c + \mathbf{E}^p = \frac{|\nabla\xi|}{J}\left(\overline{\mathcal{U}}\Phi + p\Psi\right), \tag{3.10}$$

$$\Phi = \begin{bmatrix} \rho Y_{V,1} Y_V \\ \vdots \\ \rho Y_{V,N_V-1} Y_V \\ \rho Y_V \\ \rho \\ \rho u \\ \rho v \\ \rho w \\ \rho H \end{bmatrix}, \quad \Psi = \begin{bmatrix} 0 \\ \vdots \\ 0 \\ 0 \\ 0 \\ \overline{\xi}_x \\ \overline{\xi}_y \\ \overline{\xi}_z \\ 0 \end{bmatrix}, \tag{3.11}$$

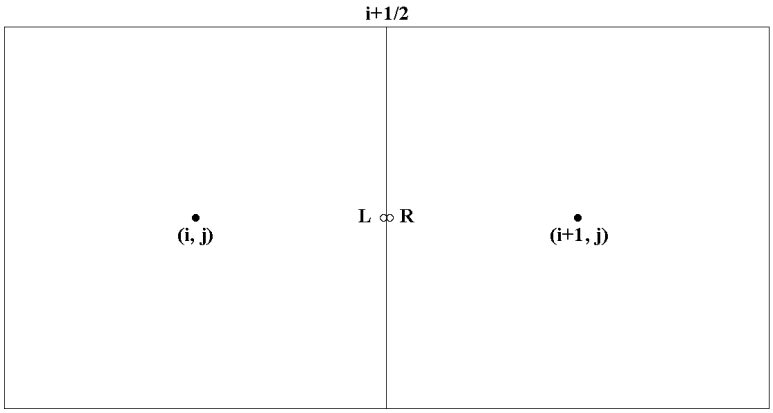

Figure 3.1: Upwinding stencil used for LDFSS algorithm (ξ direction).

Fig. 3.1 shows the computational stencil used in this work. The upwinding scheme is performed at the cell interfaces, using the properties at the left (L) and right (R) states. This results in the inviscid flux being split into convective and pressure parts as the sum of left and right components:

$$\mathbf{E}_{i+\frac{1}{2}} = \mathbf{E}^c_{i+\frac{1}{2}} + \mathbf{E}^p_{i+\frac{1}{2}} = \frac{|\nabla\xi|}{J}\left(U^+\Phi_L + U^-\Phi_R\right) + \frac{|\nabla\xi|}{J}P_{\frac{1}{2}}\Psi_i, \tag{3.12}$$

where the split velocities $U^\pm$ and the interface pressure $P_{\frac{1}{2}}$ are defined as

$$U^+ = \tilde{a}_{\frac{1}{2}}\left[\mathcal{M}^+ - \mathcal{M}_{\frac{1}{2}}\left(1 - \frac{p_L - p_R}{2\rho_L V^2_{\text{ref},\frac{1}{2}}}\right)\right], \tag{3.13}$$

$$U^- = \tilde{a}_{\frac{1}{2}}\left[\mathcal{M}^- + \mathcal{M}_{\frac{1}{2}}\left(1 + \frac{p_L - p_R}{2\rho_R V^2_{\text{ref},\frac{1}{2}}}\right)\right], \tag{3.14}$$

$$P_{\frac{1}{2}} = \frac{1}{2}\left(p_L + p_R\right) + \frac{1}{2}\left(P^+ - P^-\right)\left(p_L - p_R\right) + \rho_{\frac{1}{2}}V^2_{\text{ref},\frac{1}{2}}\left(P^+ + P^- - 1\right), \tag{3.15}$$

where $\rho_{\frac{1}{2}}$ is the interface density, $V_{\text{ref},\frac{1}{2}}$ is the interface reference velocity as defined in Eq. 3.4 or Eq. 3.5, and $\tilde{a}_{\frac{1}{2}}$ is a "numerical speed of sound" [49; 50; 54] derived from the acoustic eigenvalues of the preconditioned system and evaluated at a cell interface:

$$\tilde{a}_{\frac{1}{2}} = \left[\frac{\sqrt{\left(1 - M^2_{\text{ref}}\right)^2\overline{\mathcal{U}}^2 + 4V^2_{\text{ref,un}}}}{1 + M^2_{\text{ref}}}\right]_{\frac{1}{2}}, \tag{3.16}$$

where the '$\frac{1}{2}$' subscript indicates the evaluation using cell-averaged velocity and sound

speed data, and M_{ref} is the reference Mach number as defined in Eq. 3.7. This study utilizes arithmetic averaging for the cell-averaged data. For instance, the averaged sound speed looks like, $a_{\frac{1}{2}} = \frac{1}{2}\left(a_L + a_R\right)$. Other quantities needed are Mach numbers at left and right states, and van Leer/Liou polynomials in Mach number [55]:

$$\begin{aligned} M_{L,R} &= \frac{\overline{u}_{L,R}}{\tilde{a}_{\frac{1}{2}}} \\ M^{\pm}_{(1)} &= \frac{1}{2}\left(M \pm |M|\right), \\ M^{\pm}_{(2)} &= \begin{cases} \pm\frac{1}{4}\left(M \pm 1\right)^2, & |M| < 1, \\ M^{\pm}_{(1)}, & \text{otherwise}, \end{cases} \end{aligned} \tag{3.17}$$

The properties at the left (L) and right (R) states used in the above definitions will be specified later in Section 3.2.2. The split Mach numbers in the above equations are given as:

$$\begin{aligned} &\mathcal{M}^{+} = \alpha^{+}_{L}\left(1+\beta_L\right)M_L - \beta_L M^{+}_{(2),L}, \\ &\mathcal{M}^{-} = \alpha^{-}_{R}\left(1+\beta_R\right)M_R - \beta_R M^{-}_{(2),R}, \\ &\alpha^{\pm}_{L,R} = \frac{1}{2}\left[1.0 \pm \text{sign}\left(1.0, M_{L,R}\right)\right], \\ &\beta_{L,R} = -\max\left[0.0, 1.0 - \text{int}\left(|M_{L,R}|\right)\right], \\ &\mathcal{M}_{\frac{1}{2}} = \frac{1}{2}\left(\mathcal{M}^{+} - \alpha^{+}_{L}M_L - \mathcal{M}^{-} + \alpha^{-}_{R}M_R\right), \\ &P^{\pm} = \alpha^{\pm}_{L,R}\left(1+\beta_{L,R}\right) - \frac{\beta_{L,R}}{2}\left[1.0 \pm g\left(M_{L,R}\right)\right], \end{aligned} \tag{3.18}$$

where $g\left(M\right)$ is a γ-polynomial proposed by Liou [51; 55]:

$$g\left(M\right) = \begin{cases} M, & \text{in first degree,} \\ \left(\frac{3}{2}+2\gamma\right)M - \left(\frac{1}{2}+4\gamma\right)M^3 + 2\gamma M^5, & \begin{cases} \text{in third degree,} & \text{if} \gamma = 0, \\ \text{in fifth degree,} & \text{if} \gamma \neq 0. \end{cases} \end{cases} \tag{3.19}$$

In the current work, $g\left(M\right)$ is chosen to be in first degree.

Different reference velocities may be used in the developments of Eqs. 3.13-3.15. For the split velocities $U^{\pm}$, the unsteady reference velocity (Eq. 3.5) is used. For the interface pressure $P_{\frac{1}{2}}$, the steady reference velocity (Eq. 3.4) is used. These choices require different expressions for $\tilde{a}_{\frac{1}{2}}$ and $M_{L,R}$, in addition to $V^2_{\text{ref},\frac{1}{2}}$.

3.2.2 Second-Order Extension

The second-order extension of the LDFSS is achieved by a TVD-type limited interpolation [56] of the primitive variables to the cell interface.

The interpolation of an arbitrary property, q, to the left and right states can be expressed as:

$$\begin{aligned} q_L &= q_i + \frac{1}{2} P_i^l \cdot \text{avg}\left(q_{i+1} - q_i, q_i - q_{i-1}\right), \\ q_R &= q_{i+1} - \frac{1}{2} P_{i+1}^l \cdot \text{avg}\left(q_{i+2} - q_{i+1}, q_{i+1} - q_i\right), \end{aligned} \tag{3.20}$$

where P^l is a pressure limiter introduced in Ref. [57] and $\text{avg}(a, b)$ is an averaging procedure. P_i^l is defined as:

$$\begin{aligned} P_i^l &= 1.0 - \max\left(\frac{|(\Delta p)_i|}{|(\Delta p)_i| + \kappa_0 p_\infty}, \frac{|(\Delta \alpha_g)_i|}{|(\Delta \alpha_g)_i| + \kappa_0}\right), \\ (\Delta p)_i &= p_{i+1} - p_{i-1}, \quad (\Delta \alpha_g)_i = (\alpha_g)_{i+1} - (\alpha_g)_{i-1}, \end{aligned} \tag{3.21}$$

where κ_0 is a user-defined constant, and p_∞ is the freestream pressure. The function $\text{avg}(a, b)$ is one of the TVD-type limiter. Van Leer type and minmod type limiters are used in our study, and can be expressed as [58]:

$$\text{avg}(a, b) = \begin{cases} \frac{1}{2}\left[\text{sign}(1.0, a) + \text{sign}(1.0, b)\right] \min\left(\frac{|a+b|}{2.0}, 2|a|, 2|b|\right), & \text{van Leer}, \\ \frac{1}{2}\left[\text{sign}(1.0, a) + \text{sign}(1.0, b)\right] \min\left(|a|, |b|\right), & \text{minmod}, \end{cases} \tag{3.22}$$

3.3 Time Integration

The governing equations are solved using a cell-centered, generalized coordinate finite volume discretization. The discrete representation of the governing equations given in Eq. 2.59 can be expressed as:

$$\frac{\partial \mathbf{U}_{i,j,k}}{\partial t} = -R_{i,j,k} \tag{3.23}$$

where $R_{i,j,k}$ is the residual vector that represents the "steady" part of governing equations at grid point (i,j,k),

$$R_{i,j,k} = \frac{(\mathbf{E}-\mathbf{E_v})_{i+\frac{1}{2},j,k}-(\mathbf{E}-\mathbf{E_v})_{i-\frac{1}{2},j,k}}{\Delta\xi}+\frac{(\mathbf{F}-\mathbf{F_v})_{i,j+\frac{1}{2},k}-(\mathbf{F}-\mathbf{F_v})_{i,j-\frac{1}{2},k}}{\Delta\eta} + \frac{(\mathbf{G}-\mathbf{G_v})_{i,j,k+\frac{1}{2}}-(\mathbf{G}-\mathbf{G_v})_{i,j,k-\frac{1}{2}}}{\Delta\zeta}-\mathbf{S}_{i,j,k}. \quad (3.24)$$

In order to advance the solution in time, the following backward Euler time linearization of the system is built to approximate the discretized governing equations:

$$\left[\frac{\mathbf{P}}{\Delta\tau}+\frac{1}{\Delta t}\frac{\partial\mathbf{U}}{\partial\mathbf{V}}+A-\frac{\partial\mathbf{S}}{\partial\mathbf{V}}\right]^{n+1,m}_{i,j,k}\Delta\mathbf{V}^{n+1,m+1}_{i,j,k}+B^{n+1,m}_{i,j,k}\Delta\mathbf{V}^{n+1,m+1}_{i-1,j,k}+C^{n+1,m}_{i,j,k}\Delta\mathbf{V}^{n+1,m+1}_{i+1,j,k}$$
$$+D^{n+1,m}_{i,j,k}\Delta\mathbf{V}^{n+1,m+1}_{i,j-1,k}+E^{n+1,m}_{i,j,k}\Delta\mathbf{V}^{n+1,m+1}_{i,j+1,k}+F^{n+1,m}_{i,j,k}\Delta\mathbf{V}^{n+1,m+1}_{i,j,k-1}+G^{n+1,m}_{i,j,k}\Delta\mathbf{V}^{n+1,m+1}_{i,j,k+1}$$
$$=-\mathbf{R}^{n+1,m}_{i,j,k}, \quad (3.25)$$

where $\Delta\tau$ is the pseudo time-step, Δt is the physical time-step, the matrices A-G are functions of the inviscid and viscous flux Jacobians which are constructed as outlined in Appendix C and Ref. [17], and $\mathbf{R}$ is the unsteady residual vector. At physical time level $n+1$, pseudo time-level m, the unsteady residual vector is given by:

$$\mathbf{R}^{n+1,m}=\frac{3\mathbf{U}^{n+1,m}-4\mathbf{U}^{n}+\mathbf{U}^{n-1}}{2\Delta t}+R\left(\mathbf{U}^{n+1,m}\right). \quad (3.26)$$

Eq. 3.25 may be factorized using incomplete LU (ILU) method [19] as follows:

$$\mathbf{A}\Delta\mathbf{V}^{n+1,m+1}=(\mathscr{L}+\mathscr{D}+\mathscr{U})\Delta\mathbf{V}^{n+1,m+1}=-\mathbf{R}^{n+1,m}_{i,j,k} \quad (3.27)$$

where $\mathbf{A}$ is the system Jacobian matrix. $\mathscr{L}$ and $\mathscr{U}$ are defined as:

$$\mathscr{L}=B+D+F, \quad \mathscr{U}=C+E+G. \quad (3.28)$$

$\mathscr{D}$ is defined recursively as:

$$\mathscr{D}_{i,j,k}=P_{i,j,k}-B_{i,j,k}P_{i+1,j,k}C_{i+1,j,k}-D_{i,j,k}P_{i,j+1,k}E_{i,j+1,k}-F_{i,j,k}P_{i,j,k+1}G_{i,j,k+1}, \quad (3.29)$$

where P is defined as:

$$P = \frac{\mathbf{P}}{\Delta\tau} + \frac{1}{\Delta t}\frac{\partial \mathbf{U}}{\partial \mathbf{V}} + A - \frac{\partial \mathbf{S}}{\partial \mathbf{V}} \tag{3.30}$$

The matrix $\mathbf{A}$ is approximated by the following matrix $\mathbf{M}$:

$$\mathbf{M} = (\mathscr{L} + \mathscr{D})\mathscr{D}^{-1}(\mathscr{U} + \mathscr{D}), \tag{3.31}$$

A nonlinear ILU approach for advancing the solution in pseudo-time is implemented in two steps, a backward and forward step in ξ direction as follows:

$$\text{step 1} \quad : \quad \Delta\mathbf{V}_i^{n+1,m+\frac{1}{2}} = \left(\mathscr{D}_i^{n+1,m}\right)^{-1}\left[-\mathbf{R}_i^{n+1,m} - \mathscr{U}_i^{n+1,m}\Delta\mathbf{V}_{i+1}^{n+1,m+\frac{1}{2}}\right], \tag{3.32}$$

$$\text{step 2} \quad : \quad \Delta\mathbf{V}_i^{n+1,m+1} = \Delta\mathbf{V}_i^{n+1,m+\frac{1}{2}} - \left(\mathscr{D}_i^{n+1,m}\right)^{-1}\mathscr{L}_i^{n+1,m}\Delta\mathbf{V}_{i-1}^{n+1,m+1}. \tag{3.33}$$

Jacobian matrix elements are stored over the number of blocks mapped to a particular processor, allowing the "freezing" of the matrix elements and their factorization over the duration of the subiterations. This reduces the computational workload significantly. The reference velocity as it appears in the preconditioning matrix, the definition of the local time step, and in the implicit Jacobian matrices is always chosen to be the "unsteady" definition (Eq. 3.5).

A correction scheme is used to help correct the update the primitive variables as:

$$\Delta\mathbf{V}_{\text{correction}}^{n+1,m+1} = \Delta\mathbf{V}^{n+1,m+1} - \mathbf{M}^{-1}\mathbf{A}\Delta\mathbf{V}^{n+1,m+1}. \tag{3.34}$$

The advantage of introducing this procedure is that it implicitly couples the solution across block boundaries, thus allowing a more rapid transfer of information across the domain. However, it is also more expensive since it introduces more calculations.

Finally, the primitive variables at the new pseudo-time level $m+1$ is then updated by:

$$\mathbf{V}^{n+1,m+1} = \mathbf{V}^{n+1,m} + \Delta\mathbf{V}_{\text{correction}}^{n+1,m+1}. \tag{3.35}$$

Chapter 4

Implementation

This chapter describes the experimental procedure, computational grid, and boundary conditions.

4.1 Experimental Procedure

Experiments were carried out inside a subsonic wind tunnel in Test Cell 18 of the Air Force Research Laboratory, Wright-Patterson Air Force Base. Aerated-liquid jets were injected vertically upward into the subsonic wind tunnel with the nozzle exit flush with the tunnel bottom wall. The wind tunnel has a rectangular test section with a width of 125 mm, a height of 75 mm, and a length of 406 mm. The distance between the axis of the aerated-liquid injector and the leading edge of the test section is 114 mm. Three quartz windows installed on the top and both sides of the test section provide visual observation and optical instrumentation access. Large vacuum pumps are connected to the end of the tunnel to maintain a constant backpressure. The airflow is provided continuously by two large reciprocating compressors.

A plain-orifice aerated-liquid injector, consisting of an internal tube for liquid flow and an annular passage for aerating gas, is schematically illustrated in Fig. 1.2. Nitrogen was used as the aerating gas throughout the test program.

The liquid and aerating gas injection system consists of a large liquid tank, two flow meters, and a nozzle unit. A schematic of the liquid supply system is illustrated in Fig. 4.1. The relatively large volume of the injection tank insures a constant liquid supply pressure. Liquid and aerating gas volumetric flow rates are controlled

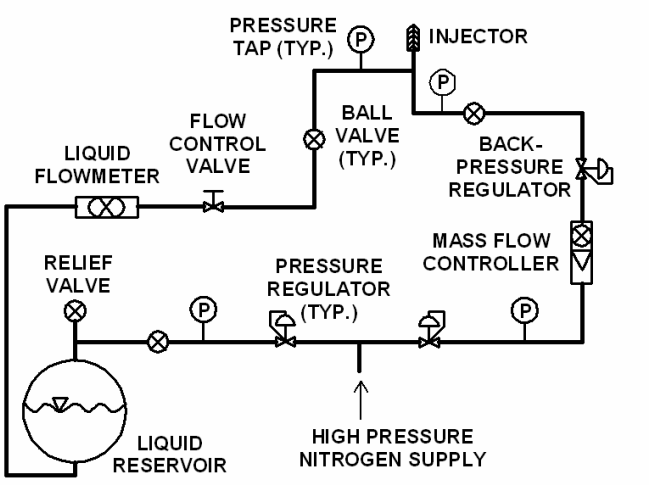

Figure 4.1: Schematic of liquid supply system

by pressure regulators and measured by flow meters. The flow meters are calibrated to an uncertainty of less than 2%. Pressure measurements inside the aerated-liquid injector were obtained using a 152 μm OD pressure probe. The probe has an inside diameter of 50 μm and was inserted from upstream of the aerated-liquid injector. The probe was positioned at various axial locations from the nozzle exit to 50.8 mm inside the injector, in order to establish the pressure profile. Due to the small inside diameter of the pressure probe, a measurement time of 40 minutes was carried out for the pressure reading to reach the steady state.

Table 4.1: Test conditions

Gas-to-Liquid (GLR) (%) mass ratio (%)	Plenum pressure (psia)	Liquid volume flow rate (l/min)	Gas volume flow rate (stl/min)
0.0	N/A	0.454	0.0
2.0	98.2	0.454	7.83
4.0	134.3	0.454	15.5
8.0	214.2	0.454	31.5

Table 4.1 presents experimental mass flow and plenum pressure levels for GLR values ranging from 0 (no gas injection) to 8% for the 1.0 mm diameter injector. Fig. 4.2 presents the corresponding gauge pressure distributions as a function of non-dimensional distance away from the exit of the discharge tube. For the higher GLR

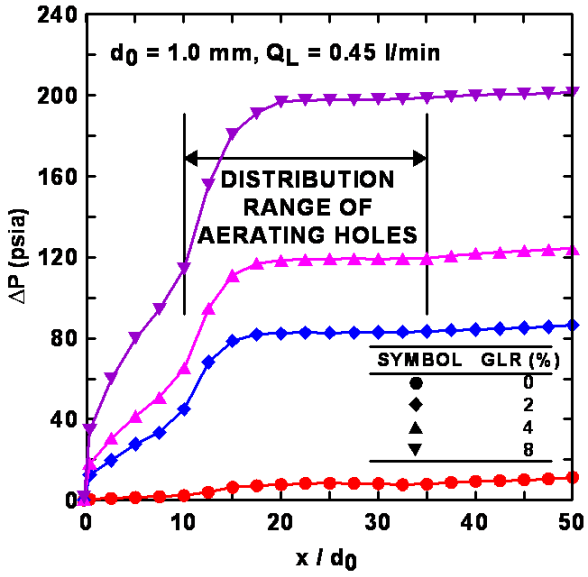

Figure 4.2: Pressure profiles within the out-in injector

values, the distributions do not recover the ambient pressure levels at the tube exit. (Ambient pressure levels are indicated at the first plotted data point, but this actually is a reference condition, not a measurement location.) This implies that the gas injection forces the choking of the flow somewhere within the tube.

4.2 Computational Grids

There are three types of computational grids with different geometries used in this study. Two of them are injector types: one contains the central injector tube only; the other one also includes the surrounding gas plenum chamber. The third type is the crossflow domain.

Fig. 4.3 shows details of a grid of the injector configuration. GridPro software (Program Development Corporation) was used to generate a simply-connected, multi-block structured mesh encompassing the central discharge tube, the surrounding gas plenum chamber, a small region downstream of the tube exit, and the array of aerating-gas holes.

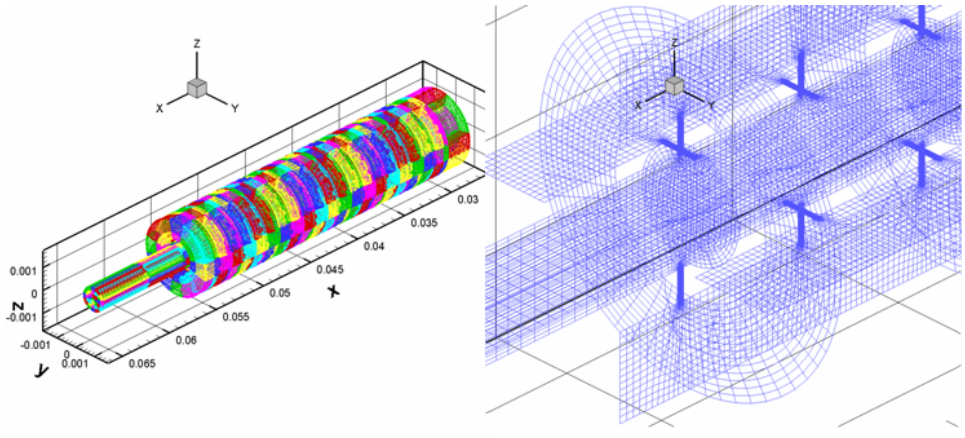

Figure 4.3: Injector grid arrangement details

In the injector simulations involving only the discharge tube, the tube grid plus external air region consists of 1852 blocks. Two grids, one containing 194, 560 interior mesh cells and the other containing 1, 556, 480 interior mesh cells, are used for the calculations with discharge tube. The grid blocks are partitioned over a fixed number of processors (16 or 25, depending on the grid size) using "METIS" load-balancing software [59]. In the injector simulations with plenum, only one grid containing 454, 912 mesh cells is used. This grid consists of 3108 blocks and is partitioned over 16 processors. Also, the probe effects are considered using level set method and immersed boundary method with this grid. In these simulations, the flow of aerating gas into the discharge tube is calculated directly, rather than being imposed as a boundary condition.

Fig. 4.4 shows details of domain decomposition of the crossflow field configuration. The distance between the axis of the injector and the leading edge of the crossflow domain is 100 mm. The entire domain consists 192 blocks containing 312, 384 interior mesh cells. These blocks are partitioned over 16 processors. Also, a refined grid containing 1, 853, 568 interior mesh cells was used for same calculations.

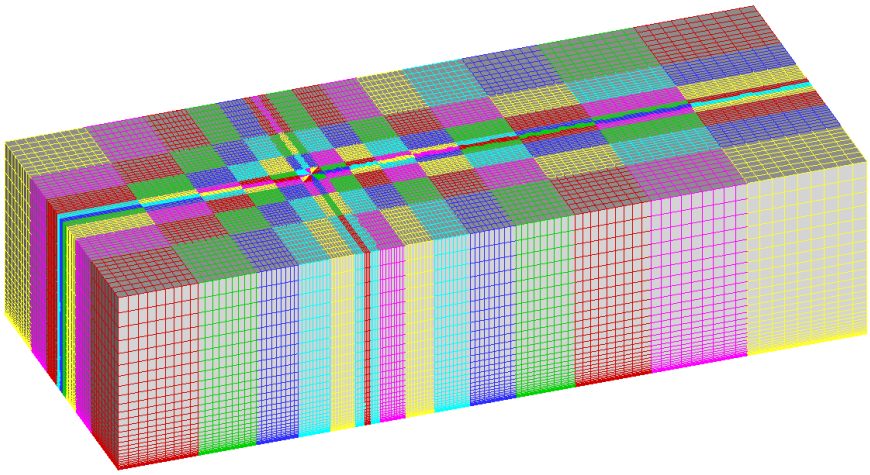

Figure 4.4: Crossflow grid blocks

The calculations were parallelized with Message-Passing Interface [60; 61] standard and run on the IBM Blade Center at North Carolina State University (see http://www.ncsu.edu/itd/hpc).

4.3 Boundary Conditions

For the injector simulations involving only the discharge tube, liquid water enters through one end while gaseous nitrogen enters through an array of small holes, oriented around the perimeter of the tube. At these entrance ports, the mass fluxes of liquid and vapor are fixed at their target values and the pressure is extrapolated from the interior. The exception is where the pressure drop is such that the flow within a gas injection hole is choked. In this case, the pressure is fixed at the choke-point value given from the isentropic analysis. The mass flux of gas is imposed as a boundary condition over each aerating hole, with values determined from experimental measurements of the pressure drop across the hole (the difference between an adjusted plenum pressure and the measured pressure level in Table 4.1) and isentropic flow theory. A uniform discharge coefficient is calculated from experimental measurements of the gas mass flow rate and is used to scale the individual mass flux values for

each hole. The two-phase mixture exits the tube into a small external region. As the flow is predicted to be choked under the conditions simulated, the flow expands supersonically into the external region. Extrapolation boundary conditions are thus used. No-slip, adiabatic wall boundary conditions are used along all solid surfaces.

In the injector simulations with plenum chamber, different inlet boundary conditions were used. These conditions include subsonic inflow boundary condition like the above, and Bernoulli inflow boundary condition. In the subsonic boundary condition, the properties, such as u, v, w, T, Y_g, etc., are fixed, while the pressure is extrapolated from the interior of the domain. In the Bernoulli boundary condition, the total pressure p_0 is fixed as:

$$p_0 = p_\infty + \frac{1}{2}\rho_\infty u_\infty^2 = \text{constant}. \tag{4.1}$$

Meanwhile axial velocity, u, is extrapolated from the interior of the domain. Extrapolation boundary conditions are used as the supersonic outflow boundary conditions. In the simulations involving the measurement probe, a level set immersed boundary method is used to determine the interface between the probe and flowfield. If a grid is determined as an interior point within the probe, then all properties at this point will be set to freestream values.

In the crossflow simulations, the subsonic inflow boundary condition is used for the inflow air. At the injection hole, all properties are fixed since flow is choked. A subsonic outflow boundary condition is used for tunnel outflow, where the pressure is fixed at the backpressure and other properties are extrapolated from the interior of the domain.

The decomposition introduces interface boundaries between adjacent blocks. The flow variables along interface boundaries were updated using adjacent interface data during the block communications.

Chapter 5

Results and Discussion

Several simulations are performed on three types of geometries (injector only, injector with plenum, and crossflow field) respectively. The results of these simulations are discussed in detail in this chapter.

5.1 Injector Simulations

Injector flowfields at three GLR mass ratios are simulated: 2%, 4% and 8%. Also, turbulence modeling is used in some cases. For the GLR = 2% case, simulations on a refined grid are also performed. Table 5.1 lists all cases simulated in this section.

Table 5.1: Description of injector simulations

Case	GLR (%)	Description
1	2.0	coarse grid, laminar
2	2.0	coarse grid, turbulent
3	2.0	refined grid, laminar
4	2.0	refined grid, turbulent
5	4.0	coarse grid, laminar
6	4.0	coarse grid, turbulent
7	8.0	coarse grid, laminar
8	8.0	coarse grid, turbulent

In this section, the basic flow features within the injector are described in detail, based on the results of coarse grid and refined grid simulations at GLR=2%. Then, a theoretical analysis is made to predict the exit pressure and inlet pressure. After that, the centerline pressure results of different cases are compared with each other, and mass conservation is also discussed.

5.1.1 Basic Flow Features

First, we will investigate the basic flow features of the two-phase flow in the injector. In order to do that, mixture density contours are plotted within the injector flowfield.

Fig. 5.1 presents snapshots of density contours within the injector after a statistically-stationary state has been reached. The GLR mass ratio is 2%, and the flow is assumed to be laminar. For clarity in viewing the figures, the Y and Z scales are both exaggerated by a factor of 2.5. The coarse grid (194, 560 interior mesh cells) is used. From this figure, we can find that the aerating gas is displaced toward the walls of the tube, forming a gas "sheath" that forces the liquid flow toward the centerline. The breakup of the narrow liquid jet (as represented by the "mixture" model) occurs about 4 tube diameters upstream of the exit. This effect is different from the in-out injector [6; 9], in which gas interaction forces the liquid flow toward the walls to create an annular jet.

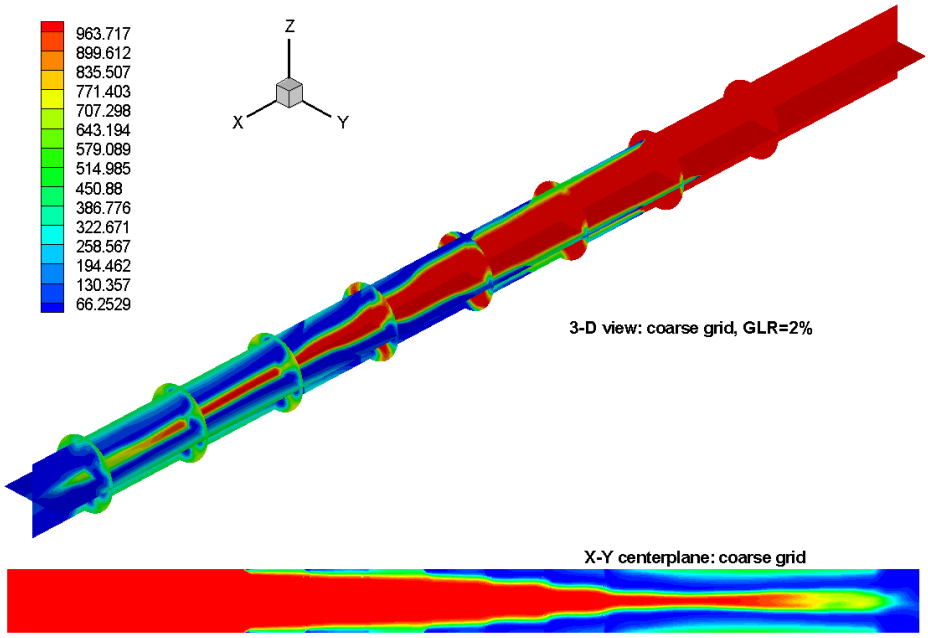

Figure 5.1: Snapshot of density contours: coarse mesh, GLR=2%

Fig. 5.2 presents density contours from a laminar calculation at GLR=2% on the

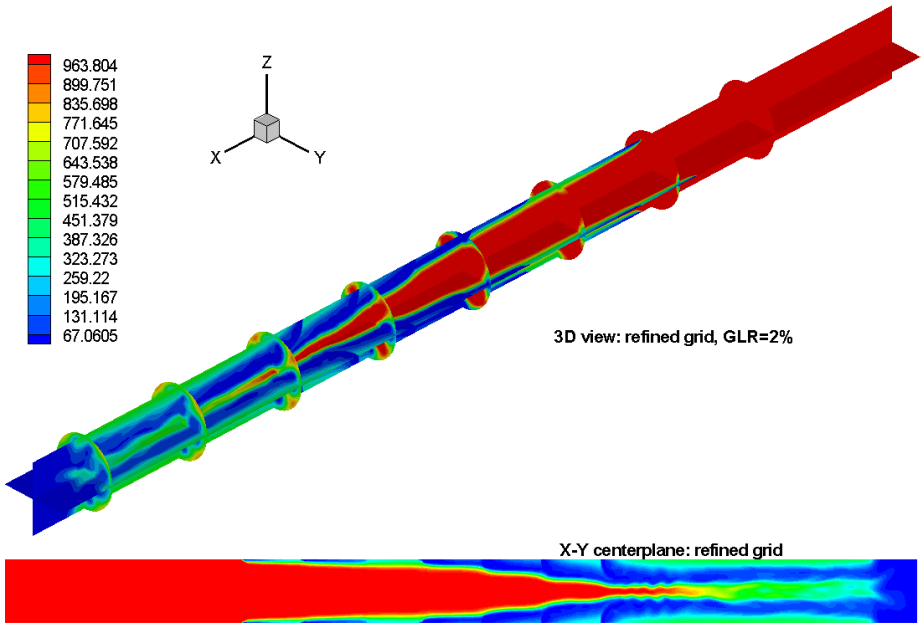

Figure 5.2: Snapshot of density contours: refined mesh, GLR=2%

refined mesh (2, 119, 932 interior points). We can find that instabilities along the gas-liquid interface are captured more clearly on the refined mesh and the breakdown of the liquid core into a highly mixed two-phase fluid occurs further upstream of the exit. Some evidence of a swirling (sinuous) mode of jet instability is seen in the 3-D snapshot and the gas jets are more clearly delineated in the 2-D centerplane snapshot. This implies that decreasing the grid size does help capture flow features more clearly.

Fig. 5.3 illusrates the two-phase mixing process through iso-surfaces of gas mass fraction extracted from the solution on the refined mesh. At this relatively low aeration level, the gas does not penetrate far into the liquid core. Therefore, liquid occupies the majority of the discharge tube.

Fig. 5.4 presents density contours along the X-Y centerplane for different GLR values assuming both laminar and turbulent flow. As before, the Y scale is exaggerated by a factor of 2.5. Since the distribution of aerating gas changes for the different GLRs, the gas is injected from different locations within the array of aerating holes.

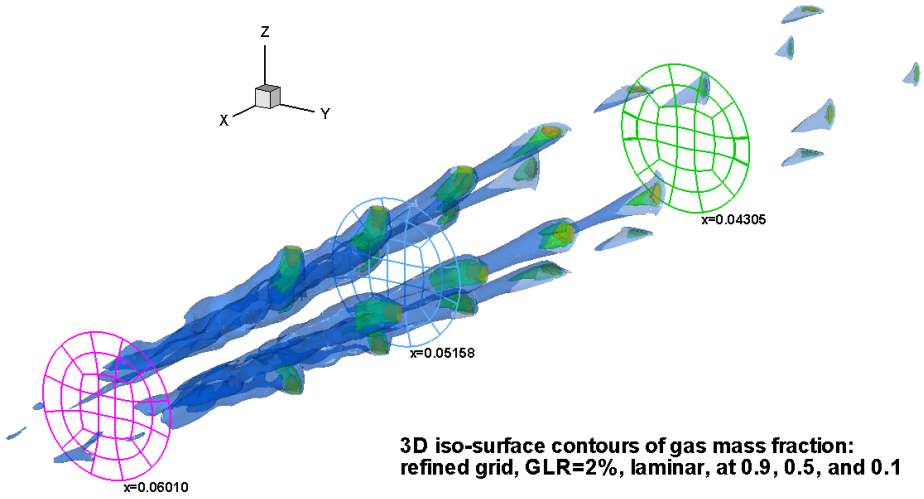

Figure 5.3: Snapshot of gas mass fraction iso-surfaces: refined mesh, GLR=2%

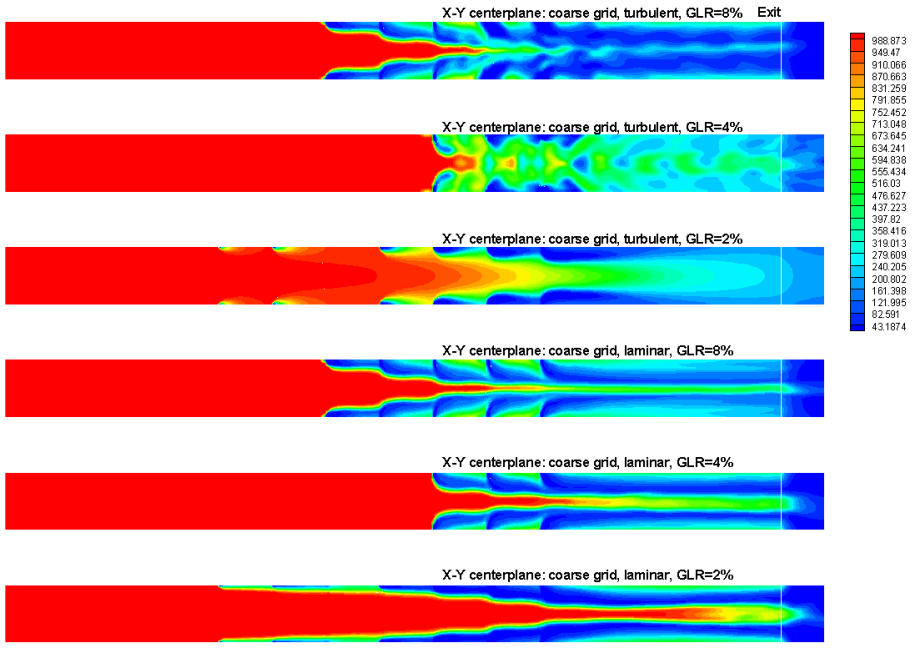

Figure 5.4: Snapshot of density contours: Coarse mesh, different GLRs

In the laminar flows, with increases in GLR value, the aerating gas forces the liquid flow toward the centerline more quickly, initiating a more rapid breakup of the liquid core due to large-scale interactions of the aerating gas jets with the liquid stream. Density contours for cases run with the turbulence model are also included. The general flow pattern is similar to the laminar results, except that the gas-liquid interface is more diffuse. This models, to some degree, the action of small-scale turbulence in stripping liquid filaments and small droplets from the central liquid jet. As a result, the two-phase mixture is more homogeneous at the exit plane.

5.1.2 Theoretical Analysis

A one-dimensional theoretical analysis is used to predict the exit pressure and inlet pressure for cases where the two-phase mixture flow is assumed isothermal (as in the calculations) and thermal non-equilibrium (with a liquid-phase energy equation from Saurel, et al.[35].) In each case, the flow is assumed to be a homogeneous mixture of liquid water and nitrogen vapor that is choked at the injector exit. Frictional forces are neglected due to the small axial extent of the injector and gravitational effects (though included in the analysis) are found to be negligible. This theoretical analysis is used to provide a consistency check when comparing pressure predictions with experimental measurements in the next section. Details of the theoretical analysis is discussed in Appendix D.

Table 5.2 and Table 5.3 list the theoretical predictions for inlet and exit pressures, exit temperature, and sound speed for the isothermal case and thermal non-equilibrium case, respectively.

As shown in the thermal non-equilibrium case, the predicted liquid temperature is very close to the predicted gas temperature at the exit plane for each GLR value. This implies that the flow can be actually treated as in a state of thermal equilibrium.

Table 5.2: Theoretical predictions for some properties (isothermal)

GLR (%)	Inlet pressure (psia)	Exit pressure (psia)	Exit liquid temp. (K)	Exit gas temp. (K)	Sound speed (m/s)
2.0	118.96	59.33	300.00	300.00	51.13
4.0	170.00	84.72	300.00	300.00	67.87
8.0	245.27	122.12	300.00	300.00	90.57

Table 5.3: Theoretical predictions for some properties (thermal non-equilibrium)

GLR (%)	Inlet pressure (psia)	Exit pressure (psia)	Exit liquid temp. (K)	Exit gas temp. (K)	Sound speed (m/s)
2.0	118.71	59.16	299.79	298.75	51.07
4.0	169.38	84.29	299.60	297.79	67.74
8.0	243.67	120.95	299.23	296.08	90.26

Also as shown in these two tables, the inclusion of thermal non-equilibrium effects results in similar predicted pressure levels and sound speed relative to the isothermal results. This implies that we can furthermore assume that the flow in the injector is in an isothermal state, which is done in our numerical simulations.

5.1.3 Centerline Pressure Results

In this section, centerline pressure results of several simulations will be compared with the experimental data and with the theoretical predictions described in the above section.

Fig. 5.5 presents a snapshot of the centerline pressures obtained on coarse and refined grids for GLR=2% assuming both laminar and turbulent flow. The results are compared with experimental data and with inlet/exit values determined from the theoretical analyses. From this figure, we can find that all numerical simulations and the theoretical analyses show higher pressure levels than indicated in the experimental data. In the upstream section, the coarse-grid laminar result is about 10 psia

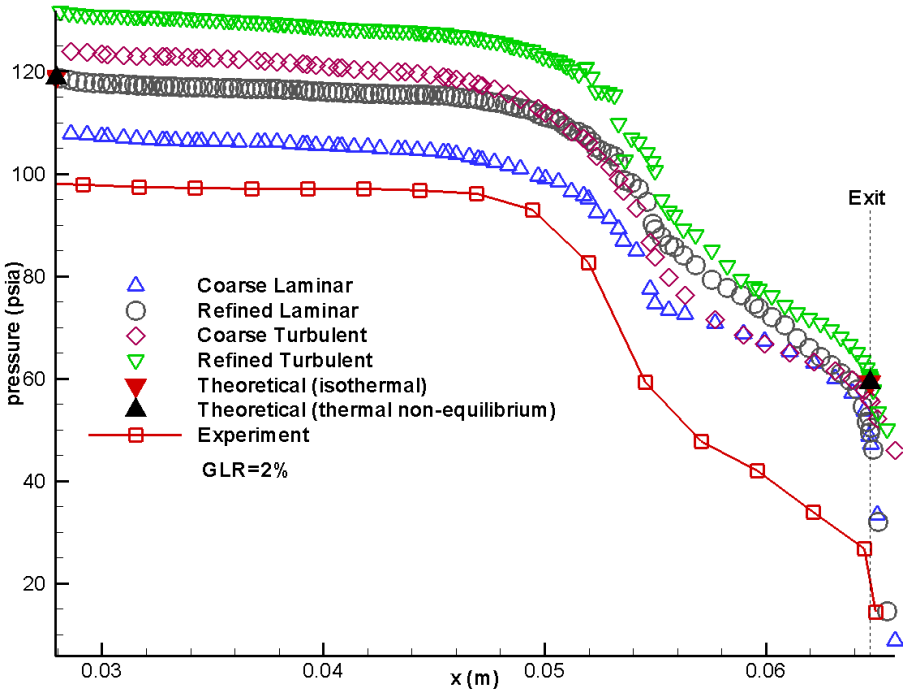

Figure 5.5: Centerline pressure distributions (GLR=2%)

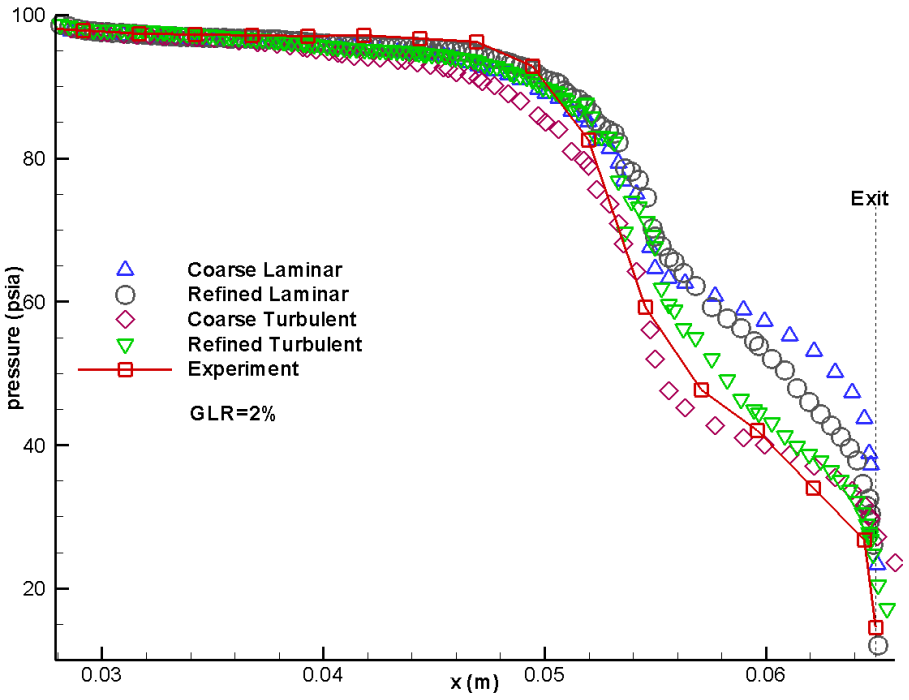

Figure 5.6: Centerline pressure distributions, after adjustment (GLR=2%)

larger than the experimental data, while the refined laminar result is 20 psia larger. The turbulent results display more of a difference between inlet and exit pressures, indicating that enhanced frictional effects are playing a role. The predicted inlet pressure for the refined-grid laminar simulation is in close agreement with the theoretical prediction. Also, exit-plane pressure values of all cases are in close agreement with the theoretical predictions, but the experimental results display a much lower pressure. This may indicate that the actual flow is not choked at the GLR=2% conditions. Another possible reason that explains the pressure difference at exit plane is the effect of the measurement probe which will be discussed in Section 5.3.

To better compare the shape of the pressure distributions, Fig. 5.6 presents an adjusted view in which the computational predictions are scaled to be at the same inlet level as the experimental results. With this view, it is evident that the fine-grid, laminar and turbulent flow predictions agree best with the experimental distribution.

Fig. 5.7 presents a snapshot of the centerline pressures at GLR=4% and on the coarse grid as compared with theoretical results and with experimental data. Again, the computational results overpredict the experimental pressure levels but agree well with the theoretical predictions. The differences between turbulent and laminar predictions are less pronounced in comparison with the GLR=2% cases. The adjusted distributions are shown in Fig. 5.8. The pressure drop across the region of gas injection is less than indicated in the experimental data, and again, the choke-point pressure is predicted to be larger.

Fig. 5.9 presents a snapshot of the centerline pressures at GLR=8% and on the coarse grid as compared with theoretical results and with experimental data. Again, the computational results agree well with the theoretical predictions, but are larger than the experimental data. The laminar result is getting close to the turbulent result. The differences between these results are smaller in comparison with the

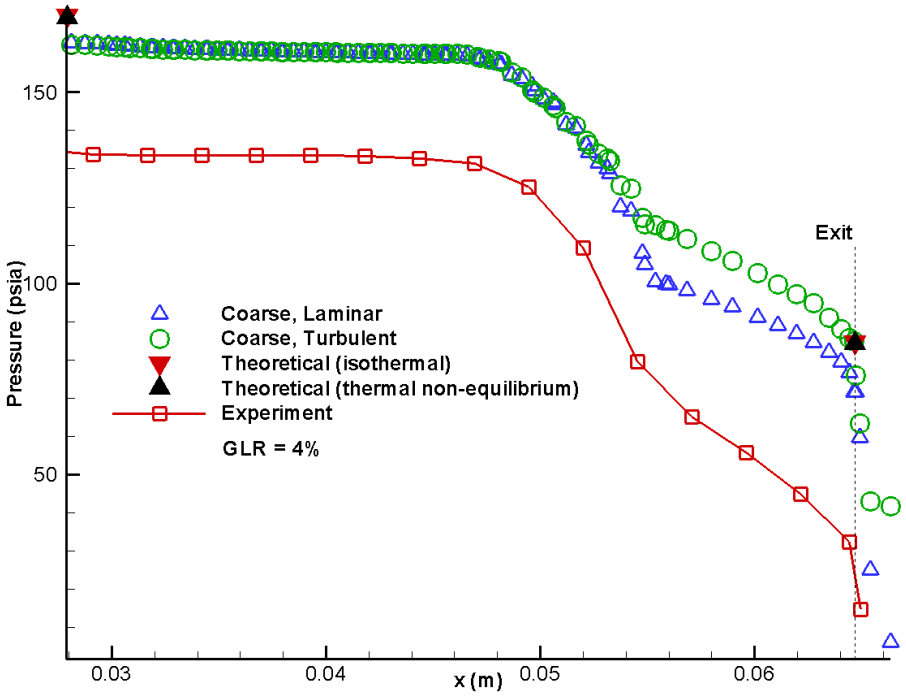

Figure 5.7: Centerline pressure distributions (GLR=4%)

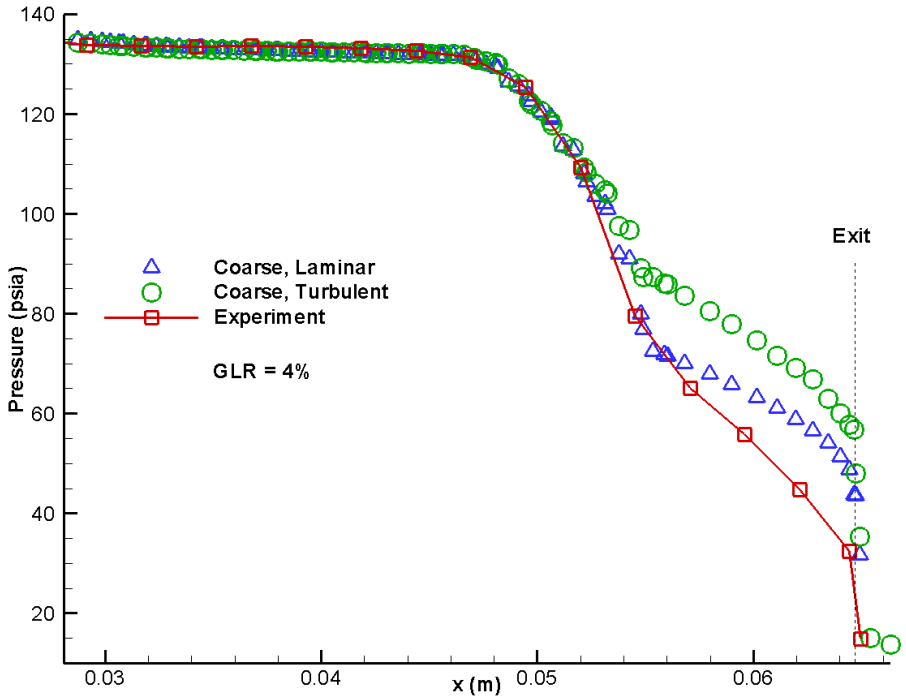

Figure 5.8: Centerline pressure distributions, after adjustment (GLR=4%)

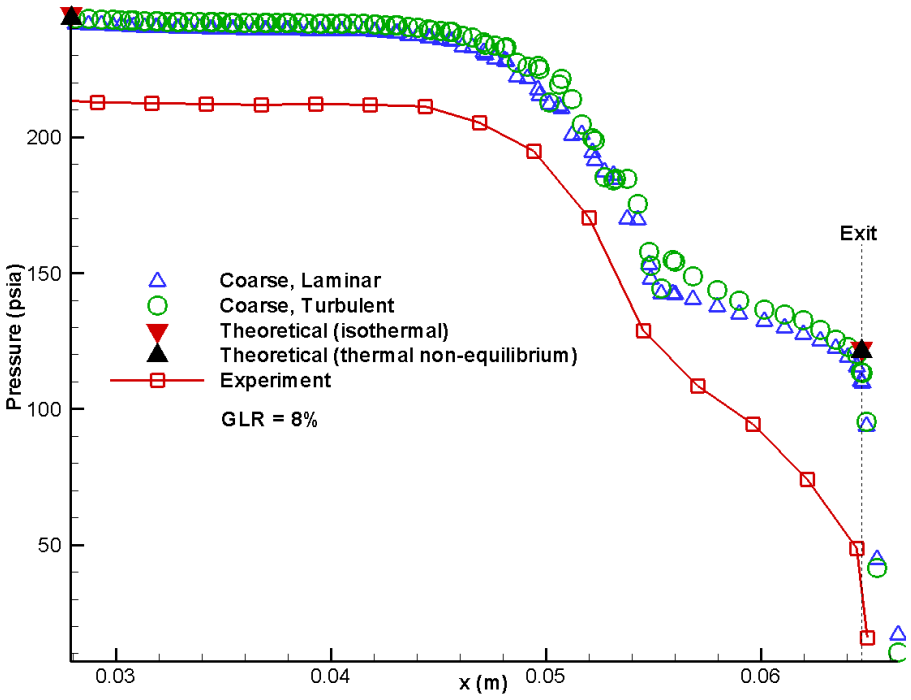

Figure 5.9: Centerline pressure distributions (GLR=8%)

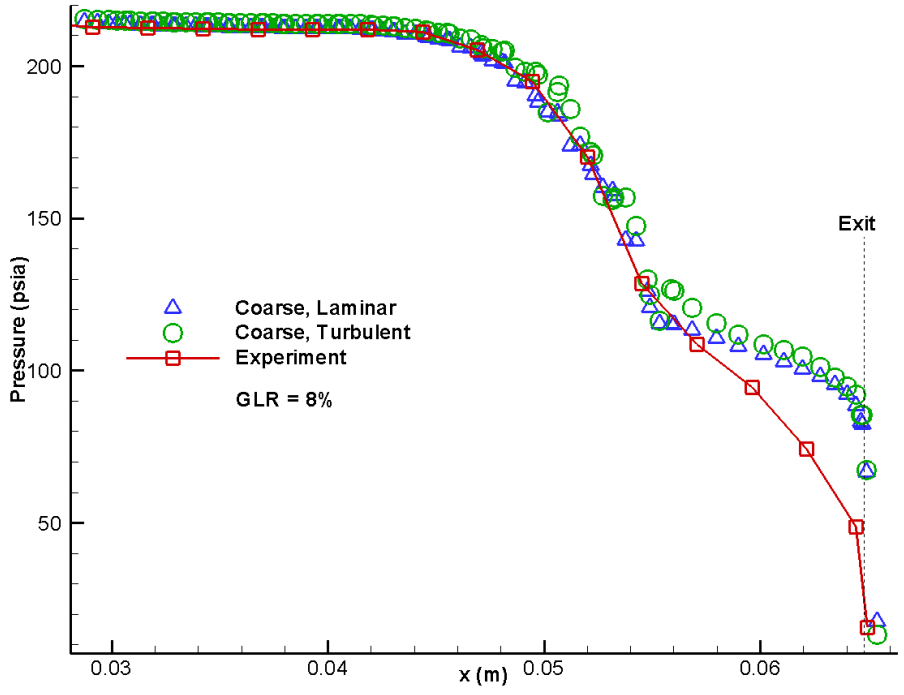

Figure 5.10: Centerline pressure distributions, after adjustment (GLR=8%)

GLR=2% and GLR=4% cases. The adjusted distributions are shown in Fig. 5.10. Again, the pressure drop across the region of gas injection is less than indicated in the experimental data, and the exit pressure is predicted to be larger.

Comparing Fig. 5.6, Fig. 5.8, and Fig. 5.10, we can find that with increases in GLR value, the predicted centerline pressure profiles generally approach the experimental data. Also, the discrepancies between the laminar and turbulent predictions get smaller with increasing GLR. This is most likely due to the fact that, at the higher aeration levels, gas-liquid mixing occurs at the largest scales, which are resolved adequately on the grid. For GLR=2% on the coarse grid, assuming laminar flow, gas injection results in the narrowing of the liquid jet but not its breakup. The inclusion of turbulence effects enhances the mixing rate substantially for this case, leading to a more homogeneous flow exiting the nozzle.

5.1.4 Mass Conservation

Figs. 5.11-5.14 show inlet and exit mass flow rates for the mixture and for the gas alone for the GLR=4% and GLR=8% laminar coarse grid cases. Good mass conservation is indicated for both cases once a statistically steady state is reached. Similar results are obtained for the GLR=2% cases.

5.1.5 Concluding Remarks

Simulations of the transient, three-dimensional, two-phase flow within the "out-in" injector discharge tube have been performed, and the results compared with experimental pressure measurements. With increases in GLR, the aerating gas forces the liquid flow toward the centerline, inducing large-scale mixing that acts to break up the liquid jet well before the exit of the tube. Only at the lowest GLR value of 2% is a relatively intact liquid core predicted to exist, and then only under assumed laminar flow conditions. Predicted centerline pressure distributions are consistent with

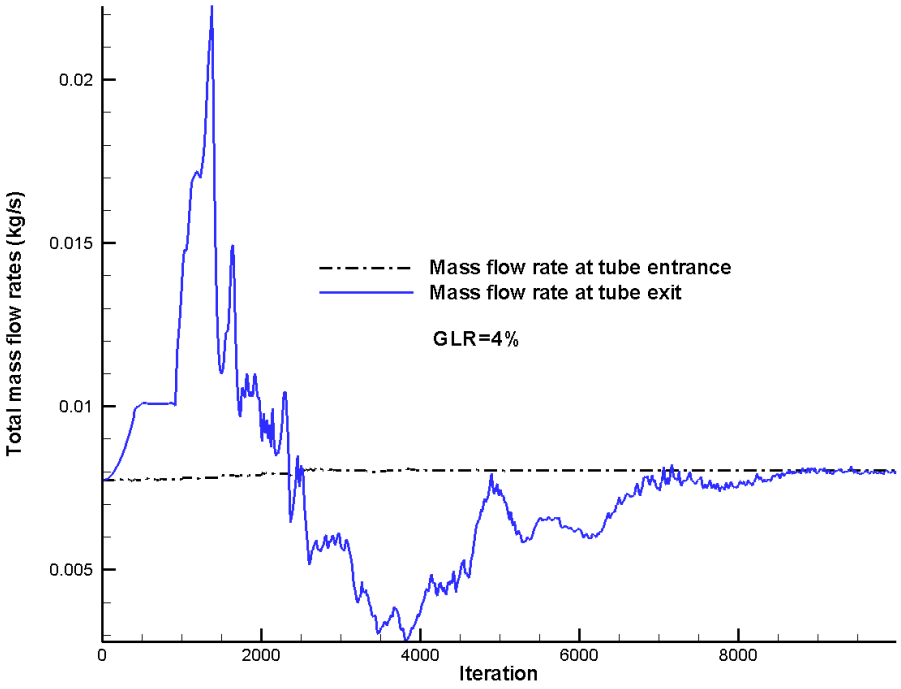

Figure 5.11: Total mass flow rates for laminar coarse grid (GLR=4%)

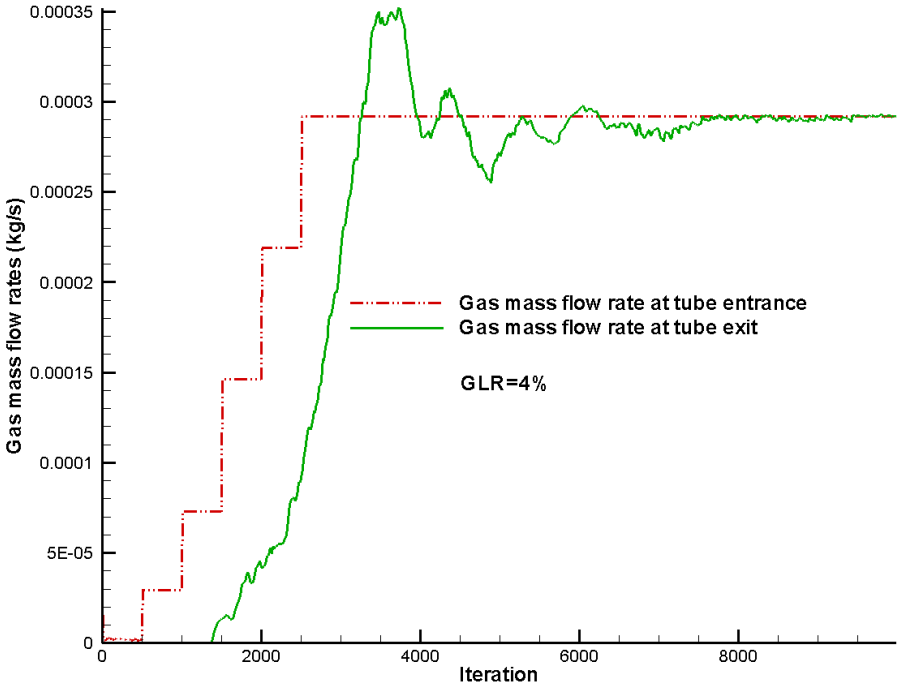

Figure 5.12: Gas mass flow rates for laminar coarse grid (GLR=4%)

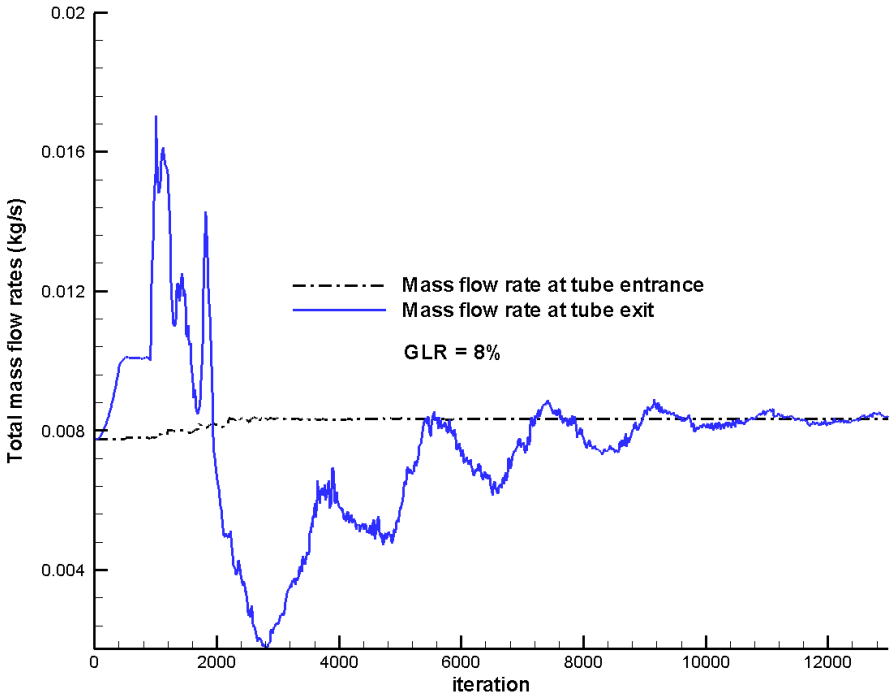

Figure 5.13: Total mass flow rates for laminar coarse grid (GLR=8%)

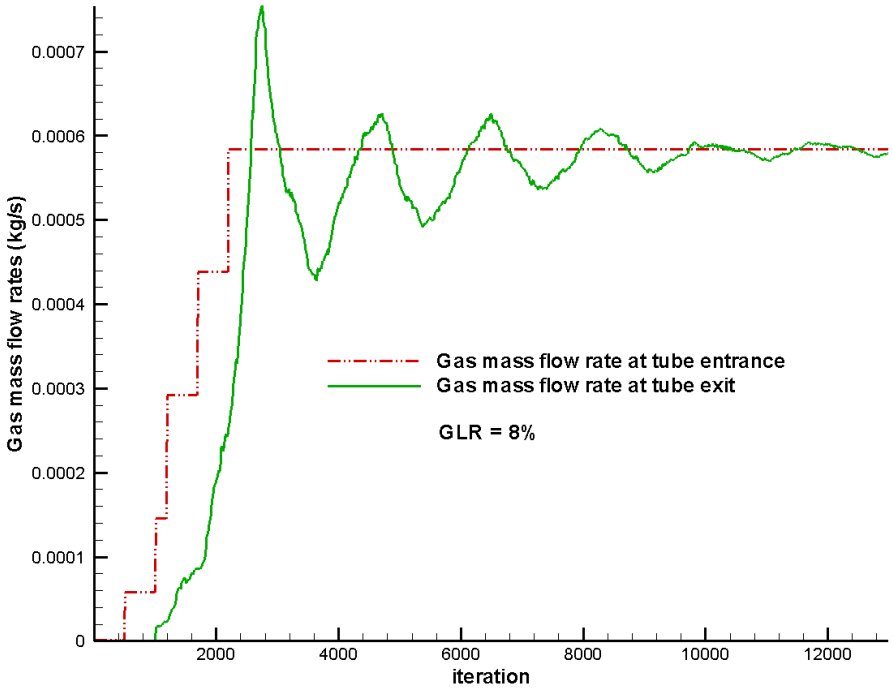

Figure 5.14: Gas mass flow rates for laminar coarse grid (GLR=8%)

theoretical analyses that assume choked flow at the exit of the injector tube, but exhibit systematically higher absolute levels compared with the experimental data. The shape of the pressure distribution induced by gas injection is best predicted when turbulence effects are modeled and when very fine grids are used.

5.2 Injector Simulations with Plenum

In section 5.1, numerical results for simulations of two-phase flow in the discharge tube are discussed in detail. The predicted centerline pressure distributions are consistent with theoretical analyses, but exhibit systematically higher absolute levels compared with the experimental data. One possible reason is that the geometry used in the simulation is different from the experiment. Only the discharge tube is used in those simulations. Thus, certain boundary conditions have to be imposed over the array of aerating-gas holes around the perimeter of the tube. But in the experiments, the aerating-gas flows into the system from the plenum inlet. In order to be more consistent with the experimental environment, a injector grid (454, 912 internal mesh cells) including the surrounding gas plenum chamber is used. With this grid, there is no boundary condition imposed over the array of aerating-gas holes. The flow into or out of the discharge tube is calculated directly.

Table 5.4: Description of injector simulations with plenum

Case	GLR (%)	Boundary conditions at inlet
1	4.0	Subsonic B.C. for both gas and liquid
2	4.0	Bernoulli B.C. for gas, subsonic B.C. for liquid
3	4.0	Bernoulli B.C. for both gas and liquid
4	4.0	Bernoulli B.C. for gas (170 psia), subsonic B.C. for liquid

Only one GLR mass ratio (4%)is chosen in the simulations, and laminar flow is assumed. Different inlet boundary conditions are used for gas and liquid. Table 5.4 lists all cases simulated in this section.

5.2.1 Basic Flow Features

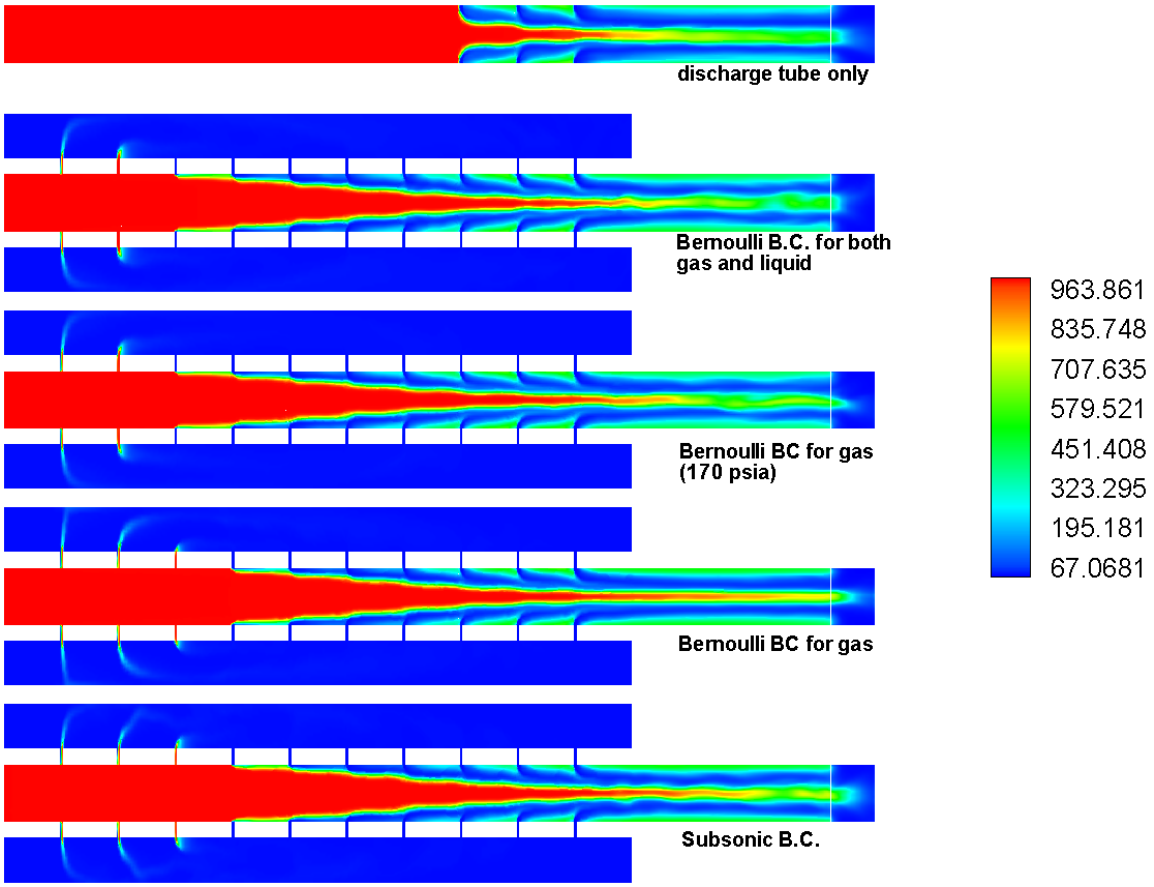

Figure 5.15: Snapshot of density contours: Coarse mesh, different BCs

Fig. 5.15 presents snapshots of density contours within the injector and the plenum along the X-Y centerplane after a statistically-stationary state has been reached. The GLR mass ratio is 4%, and the flow is assumed to be laminar. As before, the Y scale is exaggerated by a factor of 2.5. From this figure, we can find that the flow features are very similar to each other among all cases with plenum. In the upstream section, since the pressure in the discharge tube is larger than the pressure in the plenum chamber, the liquid flow is injected from the tube into the plenum. In the downstream section, the plenum pressure is larger than the tube pressure, thus the aerating gas is dispersed through the array of small holes into the discharge tube and is displaced toward the

walls of the tube, forcing the liquid flow toward the centerline. This feature is very similar to the results of discharge tube cases.

5.2.2 Case with Subsonic BCs for Gas and Liquid at Inlet

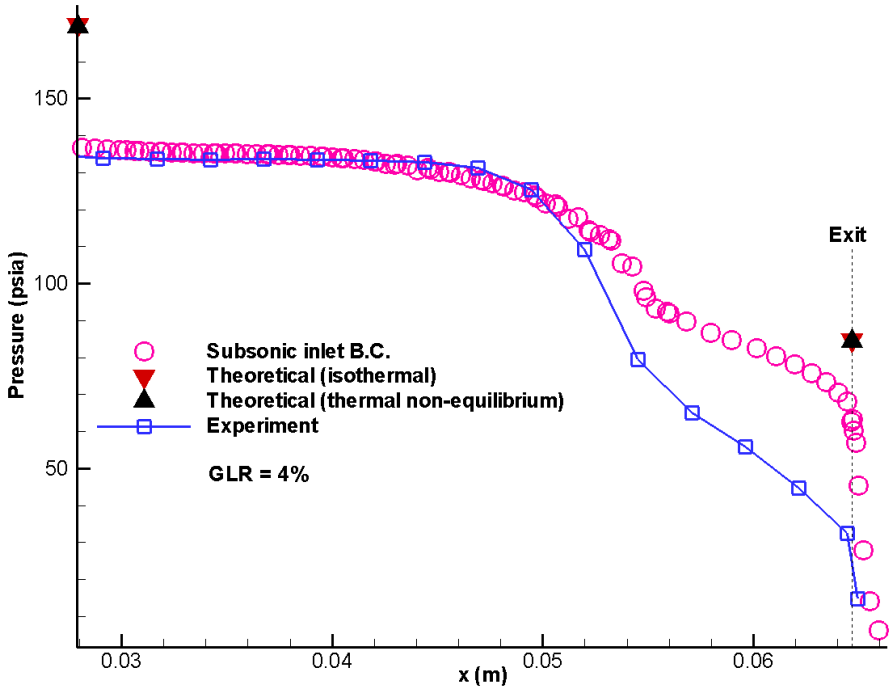

Figure 5.16: Centerline pressure distributions, subsonic BCs

Fig. 5.16 presents a snapshot of the centerline pressure obtained with subsonic boundary conditions. The results are compared with experimental data and with inlet/exit values determined from the theoretical analyses. From this figure, we can find that the numerical simulation and the experimental data show lower pressure levels than the theoretical analyses. But the shape of the pressure distribution of the simulation is more like that of discharge tube simulations: in the upstream section, the numerical result agrees well with the experimental data, but the exit-plane pressure is predicted to be larger than the experimental data.

Fig. 5.17 shows inlet and exit mass flow rates for the mixture. As shown, the exit mass flow rate approaches the inlet mass flow rate as a steady state is reached. But

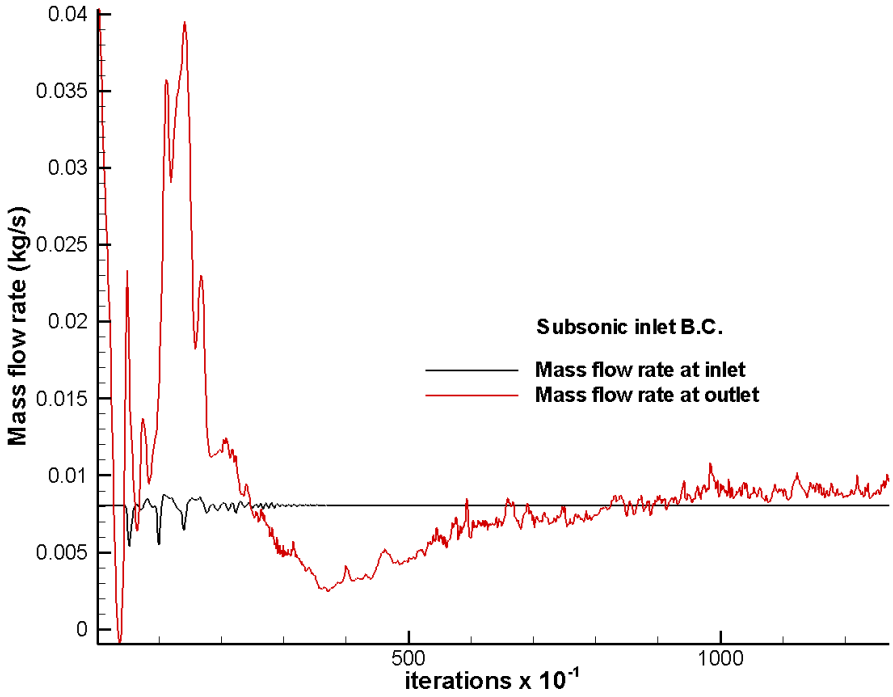

Figure 5.17: Total mass flow rates, subsonic BCs

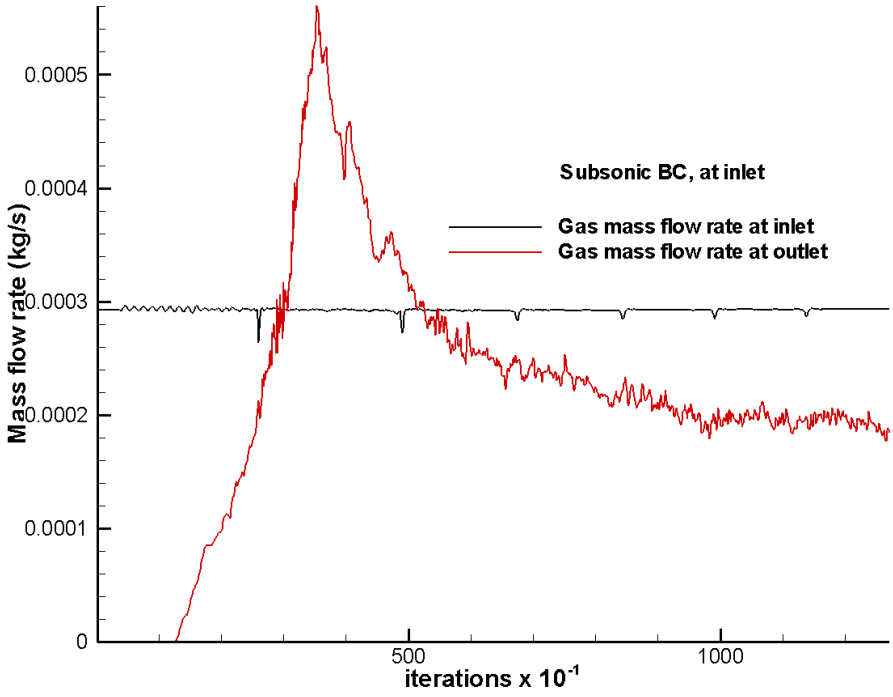

Figure 5.18: Gas mass flow rates, subsonic BCs

as shown in Fig. 5.18, the gas mass flow rate at the outlet (about 2.0×10^{-4} kg/s) does not approach the gas mass flow rate at the inlet (about 2.93×10^{-4} kg/s). The relative error is about 32%. This error is possibly due to the relatively short run times, which are not long enough for pressure disturbances to feed upstream through the array of holes to the plenum so as to adjust the pressure level to the value that would produce the correct mass flow rate.

This leads us to think about how to fix the gas mass conservation problem. One partial solution is to impose a variable gas mass flow rate at inlet. This can be implemented using Bernoulli boundary conditions. With the Bernoulli boundary condition, the total pressure is fixed at the inlet, but the static pressure and the velocity are variable. Thus, the inlet gas mass flow rate can be changed according to any change in the pressure distribution within the injector.

5.2.3 Case with Bernoulli BC for Gas at Inlet

This case starts running from the solution of Case 1 at 4900 iterations. Fig. 5.19 presents a snapshot of the centerline pressure obtained with Bernoulli boundary condition for inlet gas. The results are compared with experimental data and with inlet/exit values determined from the theoretical analyses. The centerline pressure distribution for this case is very similar to that of the case with subsonic inlet boundary condition for the gas phase. The numerical results are close to the experimental data, but are lower than the theoretical analyses. At the exit-plane, the numerical result is also larger than the experimental data.

Fig. 5.20 shows inlet and exit mass flow rates for the mixture. As shown, the exit mass flow rate approaches the inlet mass flow rate as a steady state is reached. Fig. 5.21 shows inlet and exit mass flow rates for the gas phase. This time, the outlet gas mass flow rate agrees well with the inlet gas mass flow rate when a steady state

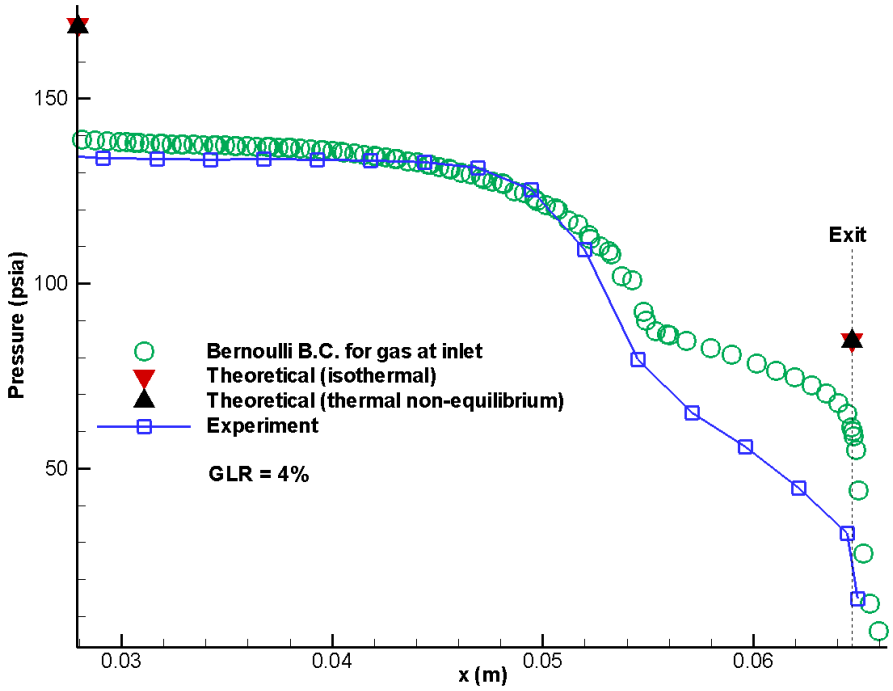

Figure 5.19: Centerline pressure distributions, Bernoulli BC for gas at inlet

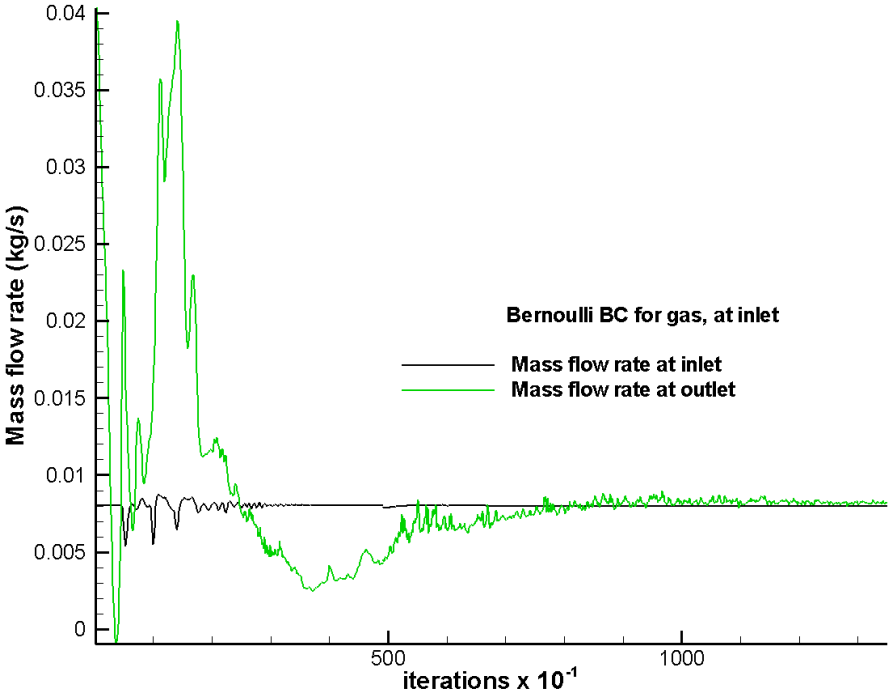

Figure 5.20: Total mass flow rates, Bernoulli BC for gas at inlet

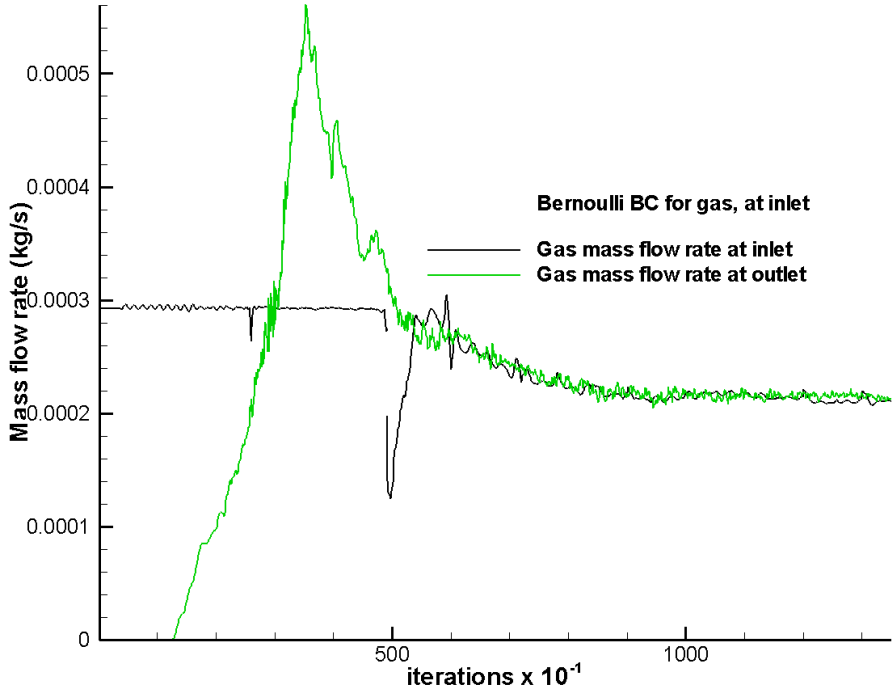

Figure 5.21: Gas mass flow rates, Bernoulli BC for gas at inlet

is reached. But both rates approach a value (about 2.1×10^{-4} m/s) which is much lower than the expected value (about 3×10^{-4} m/s). This corresponds to an effective GLR of 2.8 %.

5.2.4 Case with Bernoulli BCs for Gas and Liquid at Inlet

This case starts running from the solution of Case 2 at 13500 iterations. Fig. 5.22 presents a snapshot of the centerline pressure obtained with Bernoulli boundary conditions for both gas and liquid at the inlet. The results are compared with experimental data and with inlet/exit values determined from the theoretical analyses. The centerline pressure distribution for this case is also very similar to that of the case with subsonic boundary conditions. The numerical results are close to the experimental data, but are lower than the theoretical analyses. At the exit-plane, the numerical result is also larger than indicated in the experimental data.

Fig. 5.23 shows inlet and exit mass flow rates for the mixture. As shown, the exit

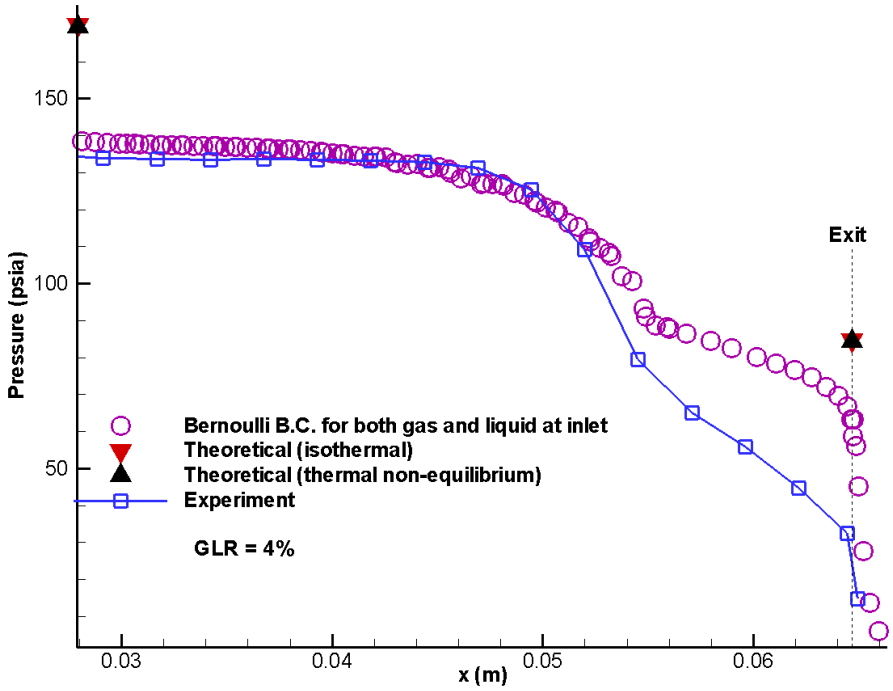

Figure 5.22: Centerline pressure distributions, Bernoulli BCs for gas and liquid

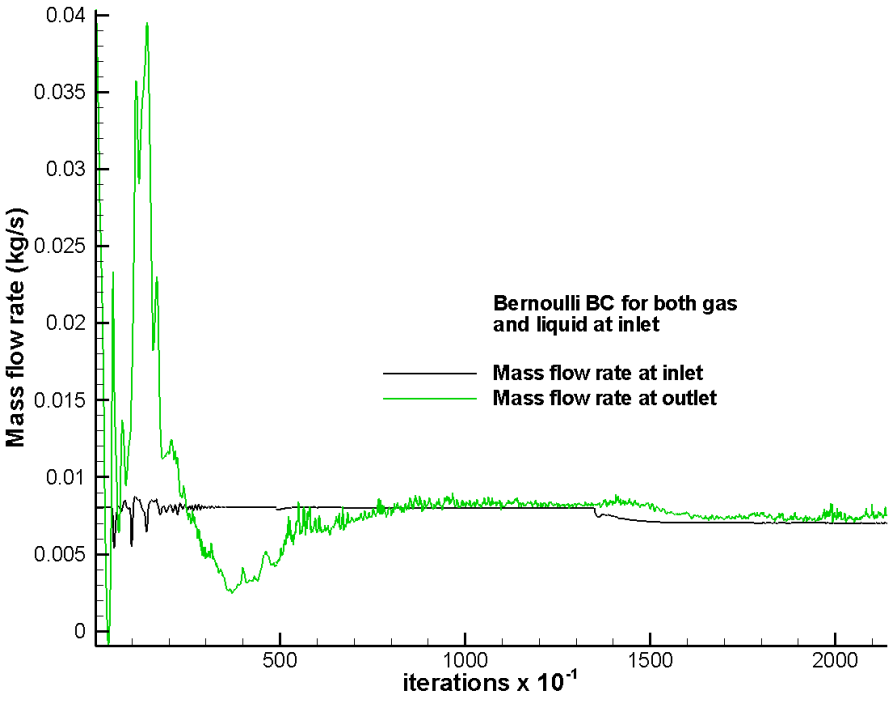

Figure 5.23: Total mass flow rates, Bernoulli BCs for gas and liquid

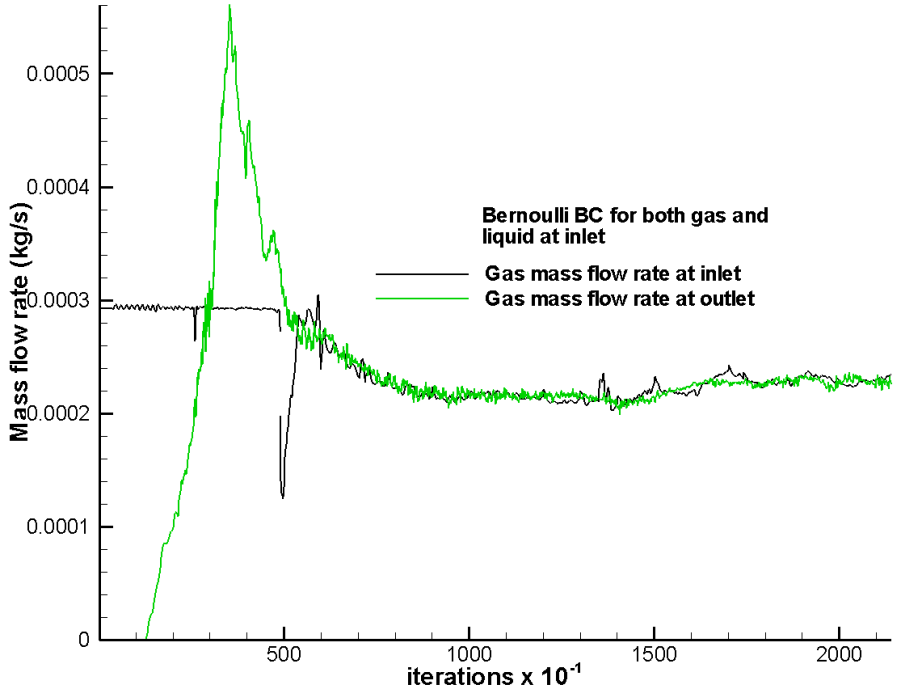

Figure 5.24: Gas mass flow rates, Bernoulli BCs for gas and liquid

mass flow rate approaches the inlet mass flow rate as a steady state is reached. Since the Bernoulli boundary condition is also imposed on the inlet liquid, the total mass flow rate at inlet (about 6.9×10^{-3} kg/s) deviates from the expected value (about 7.5×10^{-3} kg/s). Fig. 5.24 shows inlet and exit mass flow rates for the gas phase. Again, the outlet gas mass flow rate agrees well with the inlet gas mass flow rate when a steady state is reached, but both rates approach a value (about 2.3×10^{-4} m/s) which is much lower than the expected value (about 3×10^{-4} m/s). This corresponds to an effective GLR of 3.3 %.

5.2.5 Case with Bernoulli BC for Gas at a Higher Gas Pressure at Inlet

From the results of above three cases, we find that the outlet gas mass flow rate is much lower than the expected value when either the subsonic or Bernoulli boundary condition is used for the inlet gas. The aerating gas flowing into the plenum is driven

by the pressure drop acrosss the injector. Thus, if the pressure of the freestream is higher along with a constant backpressure, the more gas will flow into the plenum. With this assumption, the inlet gas pressure is assumed to be at the same value as the theoretical analysis in this case, which is about 170 psia.

This case also starts running from the solution of Case 1 at 4900 iterations. Fig. 5.25 presents a snapshot of the centerline pressure obtained with Bernoulli boundary condition for inlet gas at a higher pressure. The results are compared with experimental data and with inlet/exit values determined from the theoretical analyses. The centerline pressure distribution of this case is very similar to those of the cases with discharge tube discussed in the previous section. The numerical results agree well with the theoretical predicitons at inlet and outlet. They both show higher pressure levels than indicated in the experimental data.

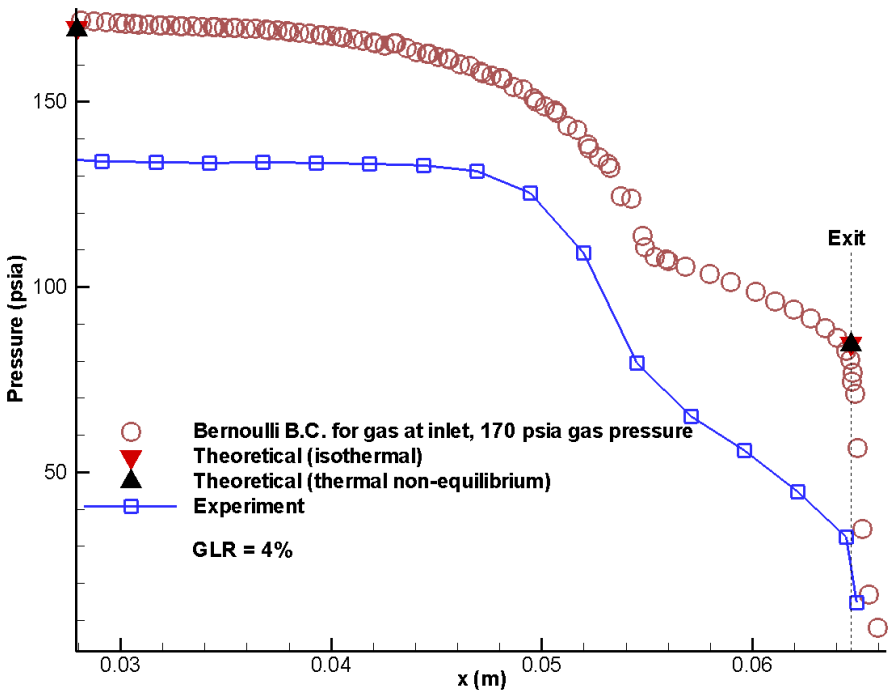

Figure 5.25: Centerline pressure distributions, Bernoulli BC for gas at inlet (170 psia gas pressure)

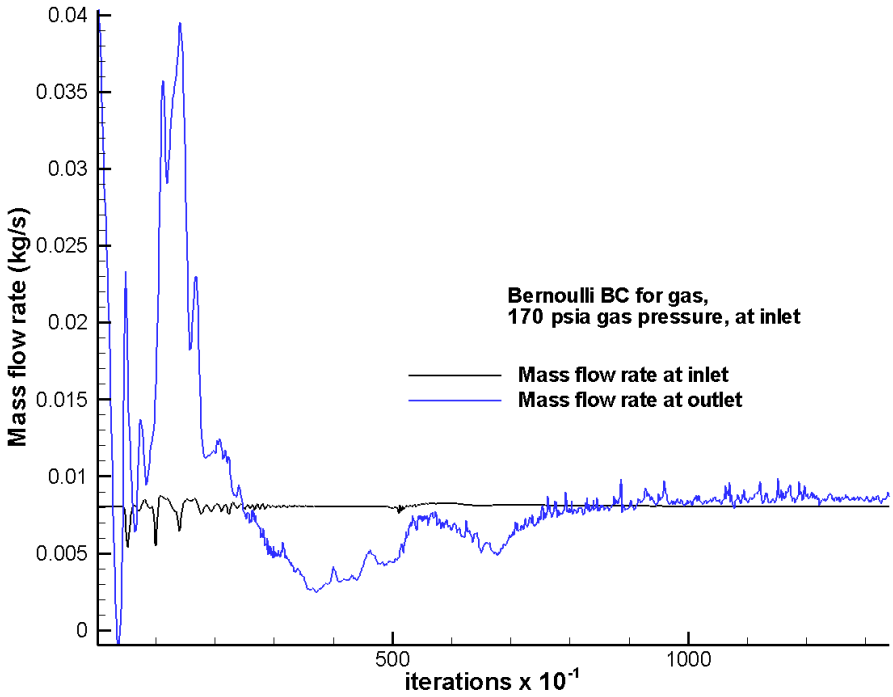

Figure 5.26: Total mass flow rates, Bernoulli BC for gas at inlet (170 psia gas pressure)

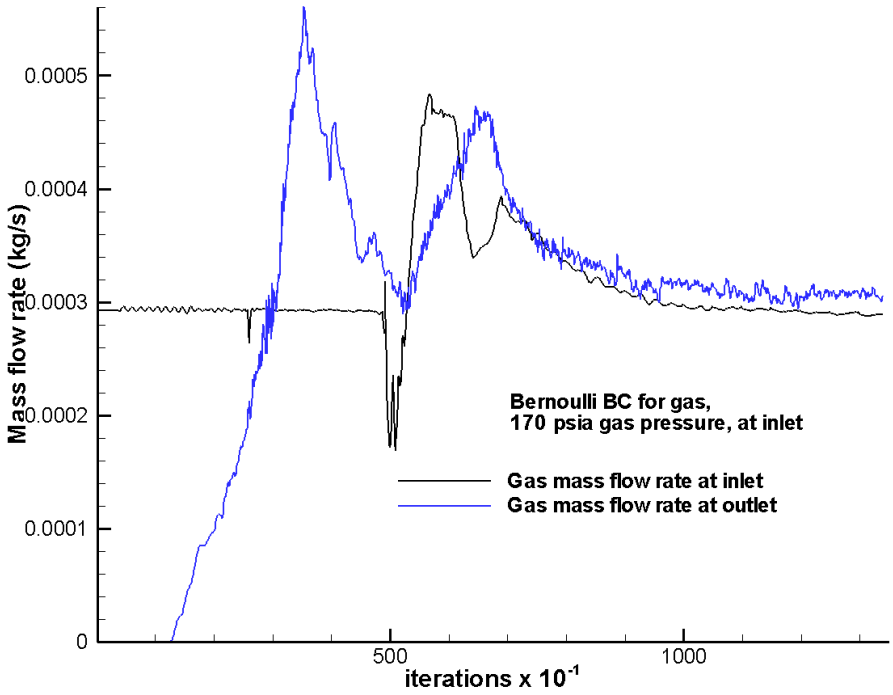

Figure 5.27: Gas mass flow rates, Bernoulli BC for gas at inlet (170 psia gas pressure)

Fig. 5.26 shows inlet and exit mass flow rates for the mixture. As shown, the exit mass flow rate approaches the inlet mass flow rate as a steady state is reached. Fig. 5.27 shows inlet and exit mass flow rates for the gas phase. This time, the outlet gas mass flow rate agrees better with the inlet gas mass flow rate when a steady state is reached but is still not completely matched. This implies that the chosen plenum pressure is slightly high. This behavior is also like that observed in the discharge tube cases.

5.2.6 Concluding Remarks

Simulations of the transient, three-dimensional, two-phase flow within the "out-in" injector with plenum chamber have been performed, and the results compared with experimental pressure measurements. The flow pattern is very similar to those simulations with discharge tube cases. The aerating gas forces the liquid flow toward the centerline, and breaks up the liquid jet well before the exit of the tube. Predicted centerline pressure distributions with all boundary conditions except one (Bernoulli BC at a higher gas pressure at inlet) are close to the experimental data, but are lower than the theoretical analyses that assume choked flow at the exit of the injector tube. The total mass gas rates at outlet in these cases approach the total mass gas rates at outlet, but the gas mass rates at outlet approach a value lower than the expected value. Predicted centerline pressure levels for the case with the Bernoulli BC at a higher gas pressure in the plenum at inlet agrees well with the theoretical analysis, but are consistently larger than the experimental data. The gas mass flow rate at outlet for this case does approach the expected value, however.

These results are consistent with those of the discharge tube cases. This implies that inaccuracies exhibited in comparing with experimental data are not the result of simplifications in the injector geometry.

5.3 Injector Simulations with Probe Effects

The results presented in the previous two sections show some discrepancies between the numerical predictions and the experimental data. If the numerical results of the mass flow rates for both mixture and gas at the outlet are at the same level as the experimental data, the centerline pressure level will be higher than the experimental data. On the other hand, if the centerline pressure at the inlet in the simulations is at the same level as the experimental data, then the gas mass flow rate at outlet in the simulations will drop below the experimental data, resulting in a lower effective GLR value. Since the pressure probe's diameter (152 μm) is not small compared with the injector diameter (1 mm), the intrusion of the probe can change the flow characteristics of the two-phase flow inside the injector, and this effect may not be negligible. Thus, we need to take the probe effects into account in the simulations.

Table 5.5: Description of injector simulations with probe effects

Case	GLR (%)	Probe tip location at x axis (m)
1	4.0	0.03
2	4.0	0.04
3	4.0	0.045
4	4.0	0.0475
5	4.0	0.05
6	4.0	0.055
7	4.0	0.06
8	4.0	0.0625
9	4.0	0.06469 (exit)

Only one GLR mass ratio (4%)is chosen in the simulations, and laminar flow is assumed. All simulations are initialized from the solution of the baseline (Case 4 in Section 5.2) at 13400 iterations. The effect of the probe on the flowfield is simulated using an immersed boundary method (Appendix E). The probe tip is positioned at various axial locations. Table 5.5 lists all cases simulated in this section.

5.3.1 Basic Flow Features

Fig. 5.28 presents snapshots of density contours within the injector and the plenum along the X-Y centerplane, where the probe tip is at $x = 0.03$m location. The GLR mass ratio is 4%, and the flow is assumed to be laminar. As before, the Y scale is exaggerated by a factor of 2.5. The probe is blanked out by only displaying the positive signed distance in the contour plots. As shown, the probe is whollly within

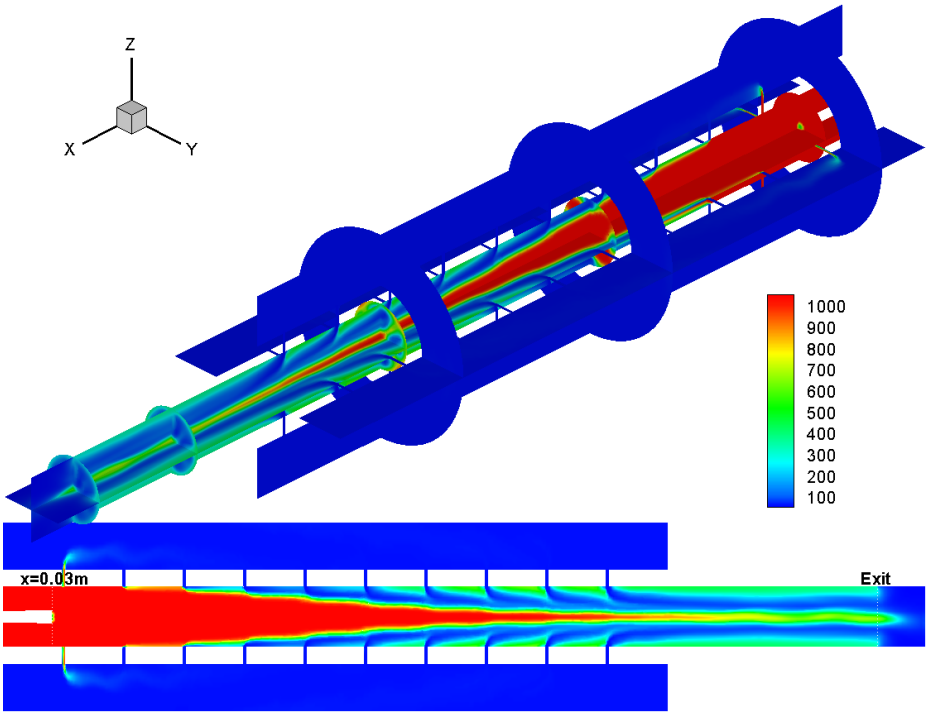

Figure 5.28: Snapshot of density contours: Probe tip at $x = 0.03$m

the liquid core, and the flow features are very similar to the plenum cases in the previous section. In the upstream section, since the pressure in the discharge tube is larger than the pressure in the plenum, the liquid flow is injected from the tube into the plenum. In the downstream section, the plenum pressure is larger than the tube pressure, thus the aerating gas is dispersed through the array of small holes into the discharge tube and is displaced toward the walls of the tube, forcing the liquid flow toward the centerline. This feature is also shown in Cases 2-4, where the probe tip

ranges from $x = 0.04$m to $x = 0.0475$m. This implies that the probe's presence has little effect on the flowfield if it is contained wholly within the liquid core.

Fig. 5.29 presents snapshots of density contours within the injector and the plenum along the X-Y centerplane, where the probe tip is at the $x = 0.05$m location. As

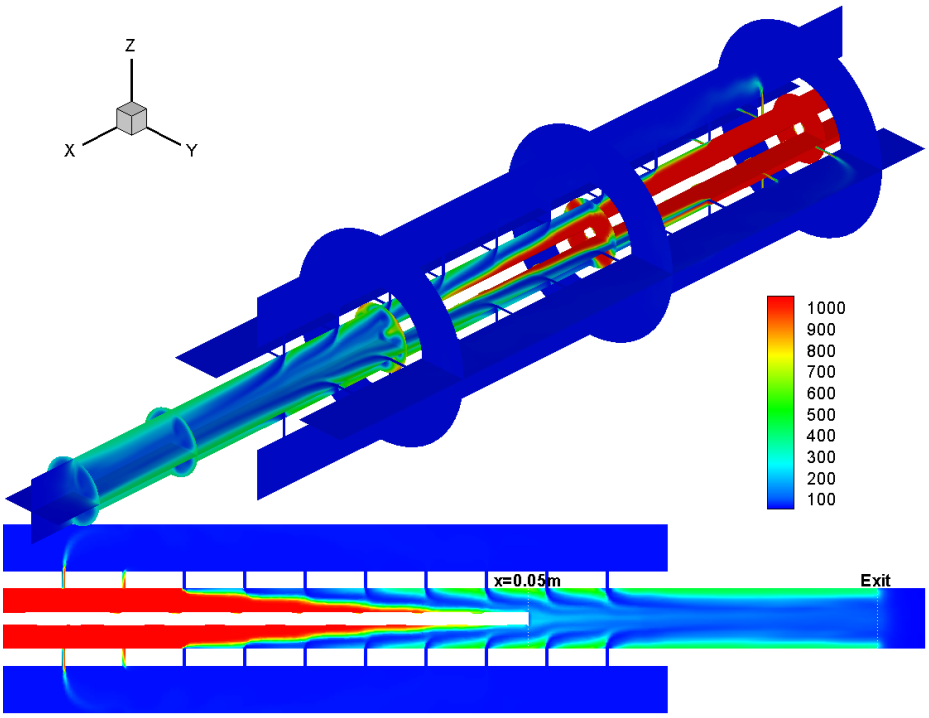

Figure 5.29: Snapshot of density contours: Probe tip at $x = 0.05$m

shown, the probe is not wholly within the liquid core any more. The probe tip is in the two-phase mixture flow, and the flow features are not as similar to Case 1 (see Fig. 5.28) and the plenum cases (see Fig. 5.15, especially in the downstream section. In the upstream section, the liquid flow is injected from the tube into the plenum as before. But in the downstream section, the breakdown of the liquid core into a highly mixed two-phase fluid right behind the wake area is accelerated due to the intrusion of the probe. The two-phase mixture is more homogeneous at the exit-plane compared with Case 1 and previous cases. Cases 6-9 also follow this change of liquid breakup. This implies that the probe's presence does affect the flowfield if the probe tip is in the two-phase fluid area.

5.3.2 Pressure Distributions

In this section, pressure distributions along the outside of the probe surface and downstream of the probe tip are compared with centerline pressure results of the baseline (Case 4 in Section 5.2), theoretical analyses and experimental data.

Fig. 5.30 presents a snapshot of the pressure distributions for Cases 1-4, where the probe tip location is from $x = 0.03$m to $x = 0.0475$m. The pressure distributions of these cases are very close to that of the baseline. The numerical results agree well with the theoretical predicitions at the inlet and outlet. They both show higher pressure levels than indicated in the experimental data. These pressure distributions further indicate that the probe has little effect on the flowfield when it is wholly within the liquid core.

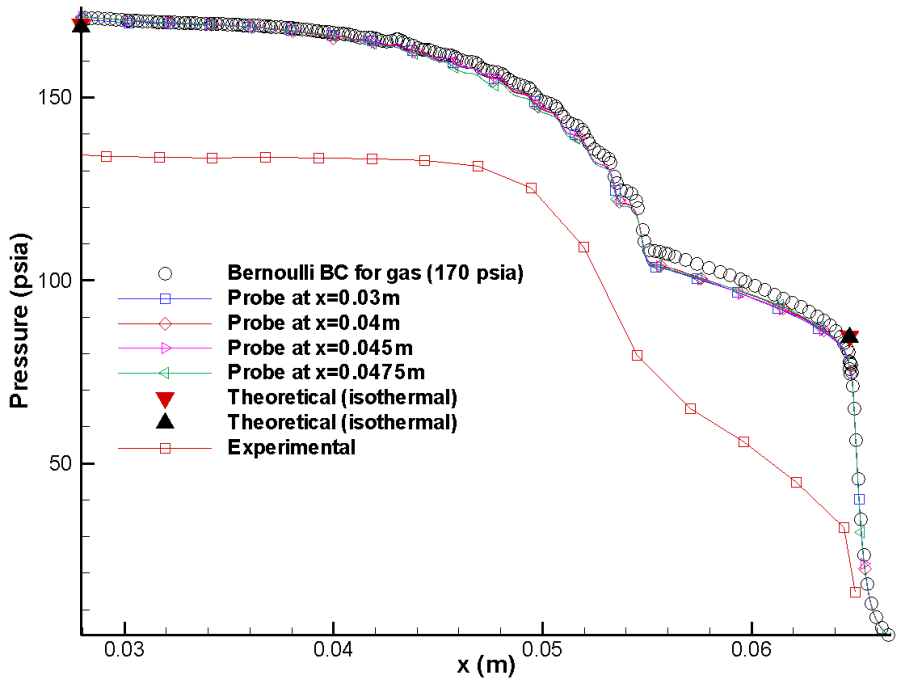

Figure 5.30: Pressure distributions, Probe tip at $x = 0.03$m-0.0475m

Figs. 5.31-5.35 present snapshots of the pressure distributions for Cases 5-9, where the probe tip location ranges from $x = 0.05$m to $x = 0.06469$m (exit). The pressure

distributions of these cases are very close to that of the baseline along the outside of the probe surface in the upstream section. In the downstream area, the pressure levels are lower than that of the baseline, but are still much higher than the experimental data. Also, right near the probe tip's location, there is a pressure dip. It is not a small drop (about 20-40 psia) compared with the pressure value (at the order of 100 psia). That also further indicates that the intrusion of the probe does affect the flowfield of the two-phase flow if the probe is not wholly within the liquid core. The dip appears to be associated with the expansion of the two-phase flow around the probe tip. At these downstream positions, the two-phase flow is supersonic, by virtue of the low sound speed of the two-phase mixture. Thus, a Prandtl-Meyer wave is generated, followed by a recompression downstream of the recirculation region located at the probe tip. The pressure tap at the probe tip would actually measure the pressure downstream of the expansion wave, which is lower than that away from the probe.

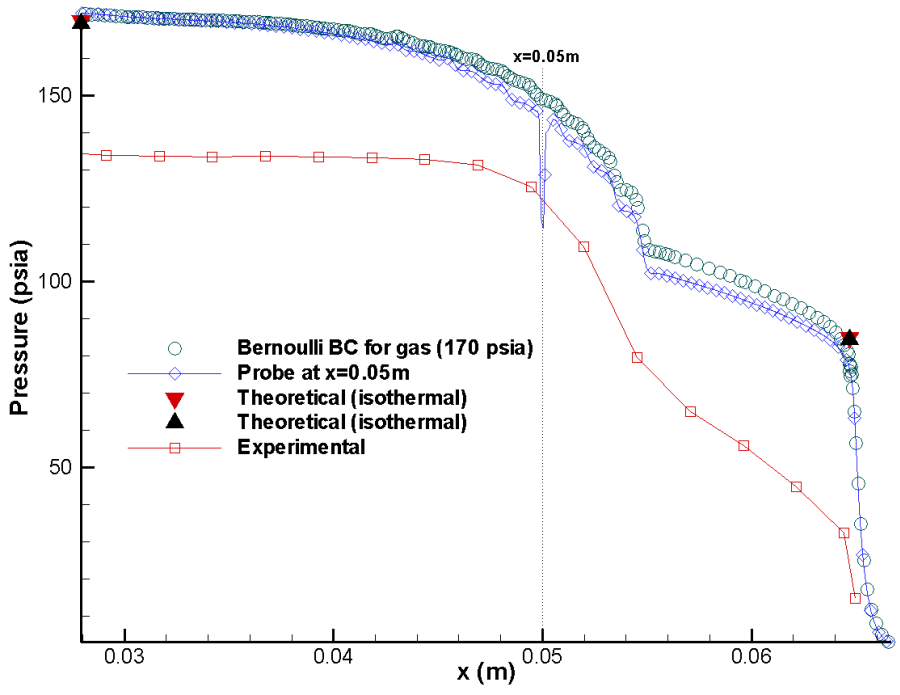

Figure 5.31: Pressure distributions, Probe tip at $x = 0.05$m

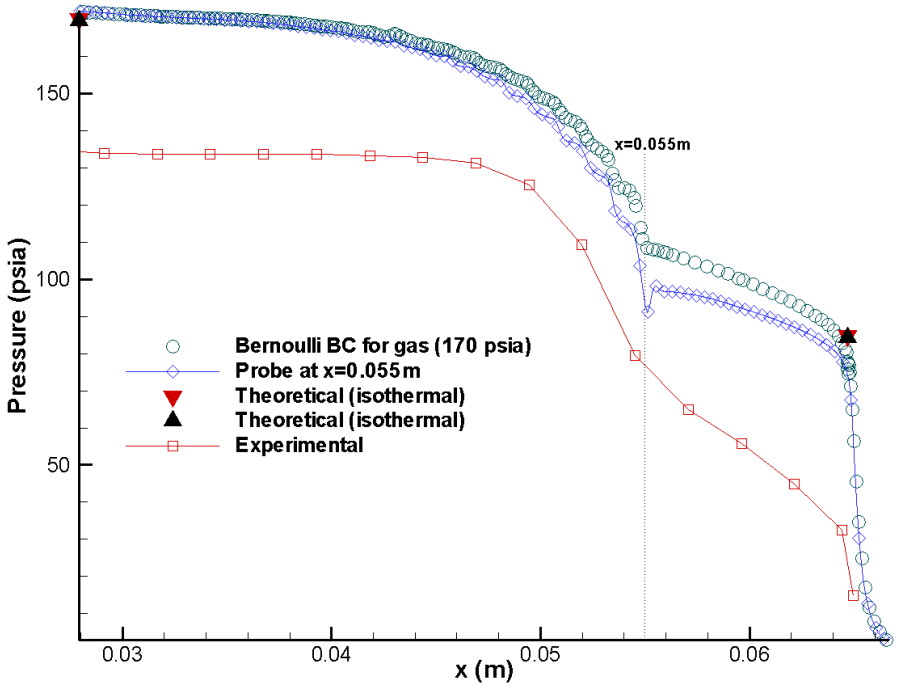

Figure 5.32: Pressure distributions, Probe tip at $x = 0.055$m

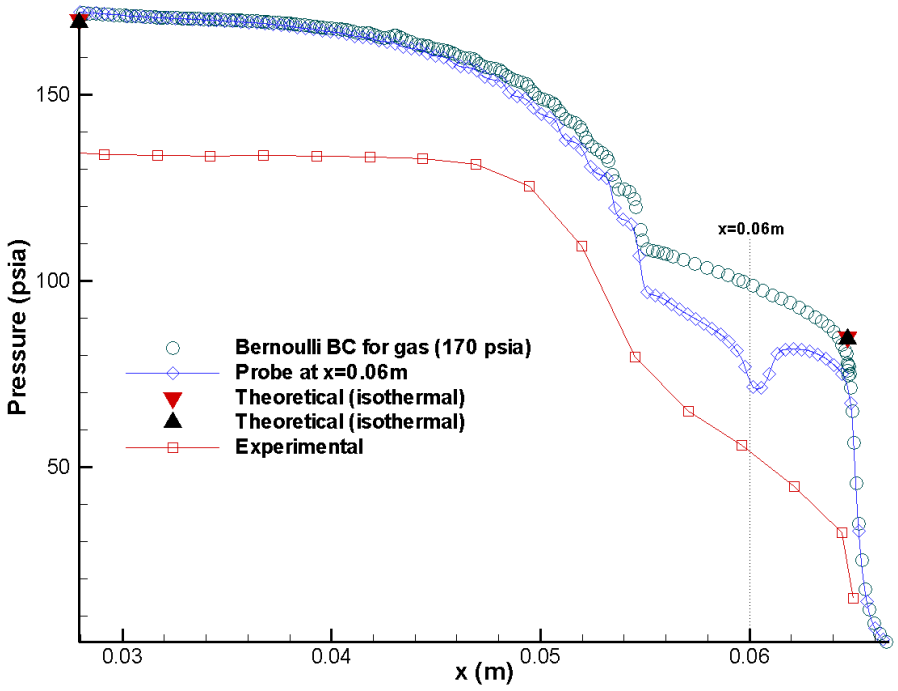

Figure 5.33: Pressure distributions, Probe tip at $x = 0.06$m

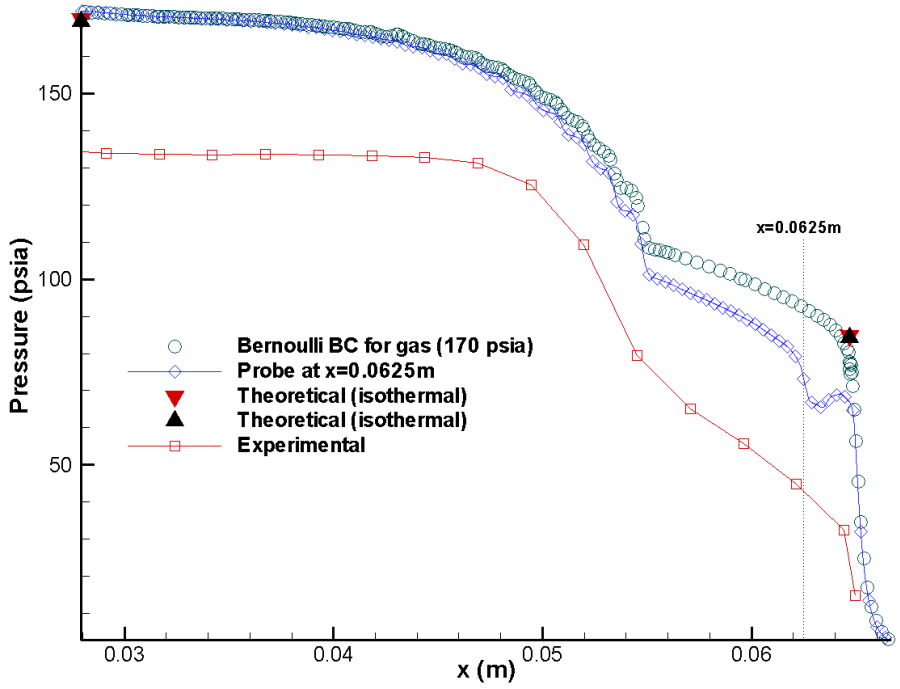

Figure 5.34: Pressure distributions, Probe tip at $x = 0.0625$m

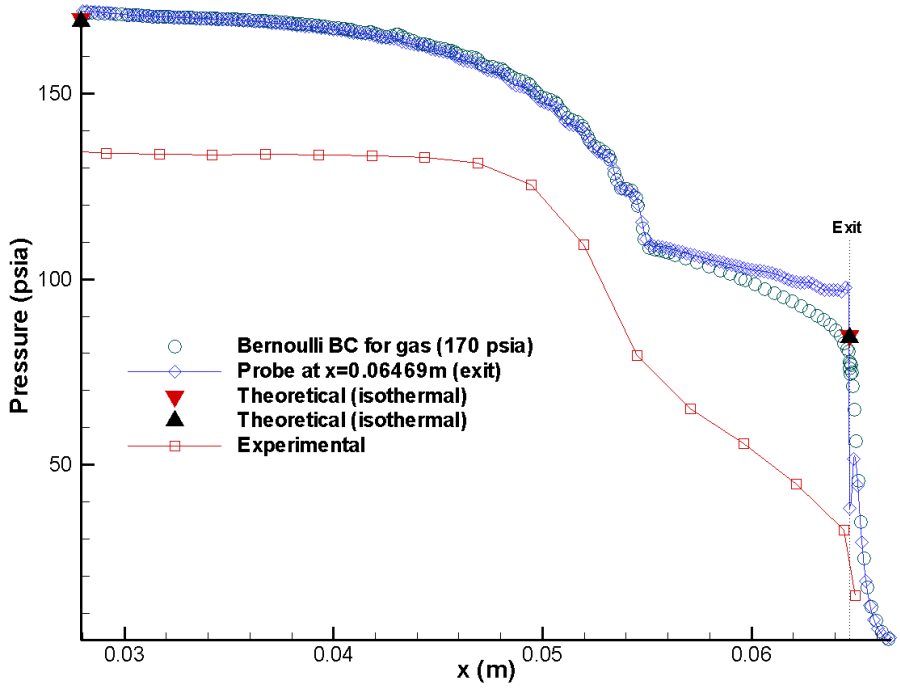

Figure 5.35: Pressure distributions, Probe tip at $x = 0.06469$m (exit)

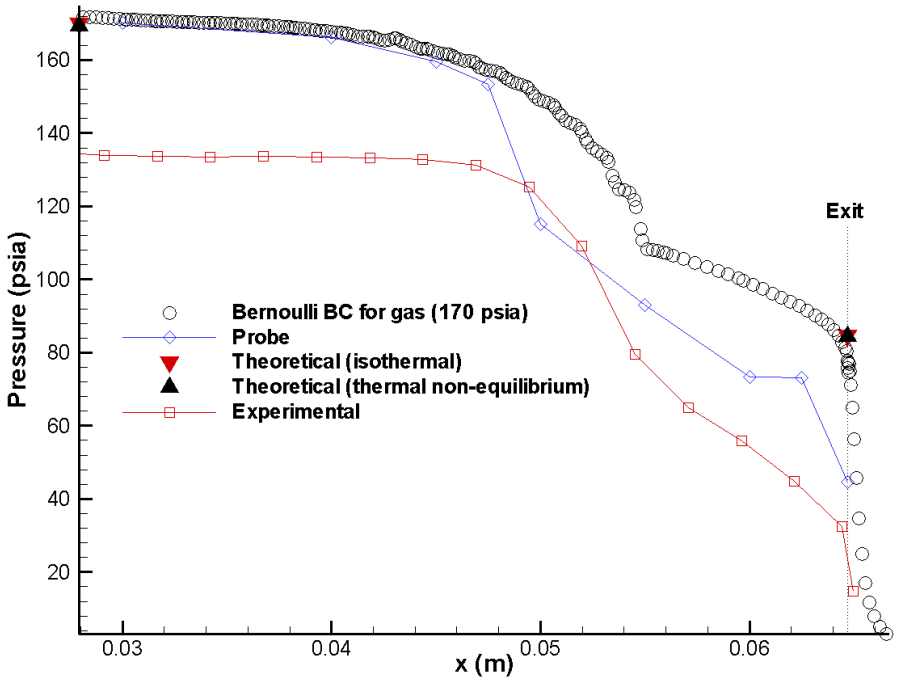

Figure 5.36: Pressure distributions, extracted from all probe tip locations

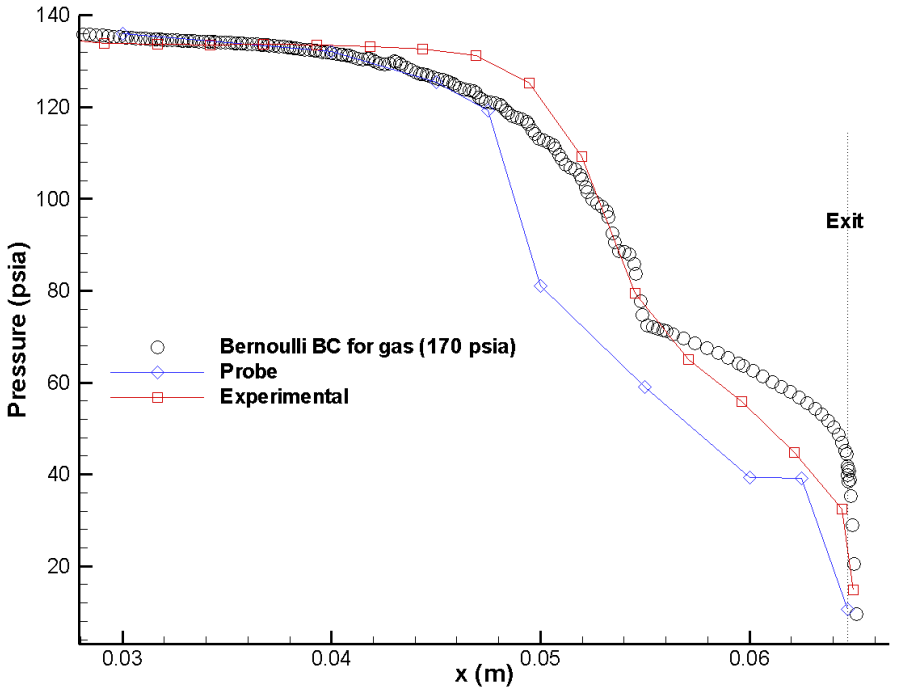

Figure 5.37: Pressure distributions (adjusted), extracted from all probe tip locations

Fig. 5.36 shows the pressure level at each probe tip location extracted from the above results. From this figure, it is clearly that the pressure level at the probe tip is progressively lowered as the probe is moved near to the exit-plane. Fig. 5.37 shows an adjusted view of the pressure distributions in the same way described in Section 5.1. We can find that in the two-phase mixing region, the shape of the pressure distribution for the probe simulations is closer to the experimental data. The distributions presented were extracted from instantaneous flowfield data. Some of the non-smooth behavior could possibly level out with time-averaging of the data, which is more insteady with the probe located toward the exit plane.

5.3.3 Mass Conservation

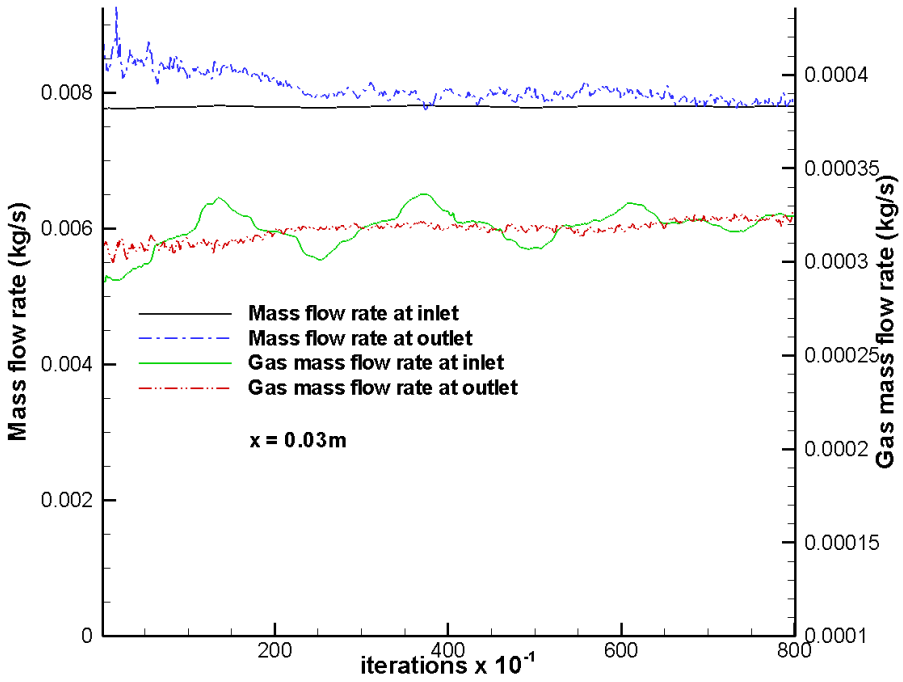

Figure 5.38: Mass flow rates for probe tip at $x = 0.03$m

Figs. 5.38-5.46 show inlet and exit mass flow rates for the mixture and the gas alone for the cases discussed in this section. It is shown that the gas mass flow rate at the outlet approaches that at the inlet for all cases. The total mass flow rate at

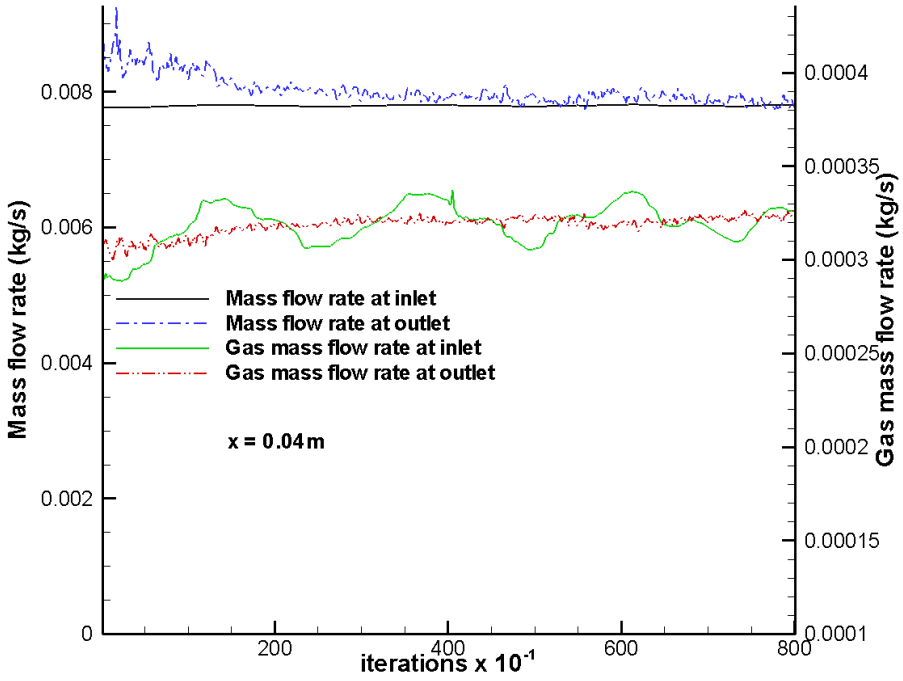

Figure 5.39: Mass flow rates for probe tip at $x = 0.04$m

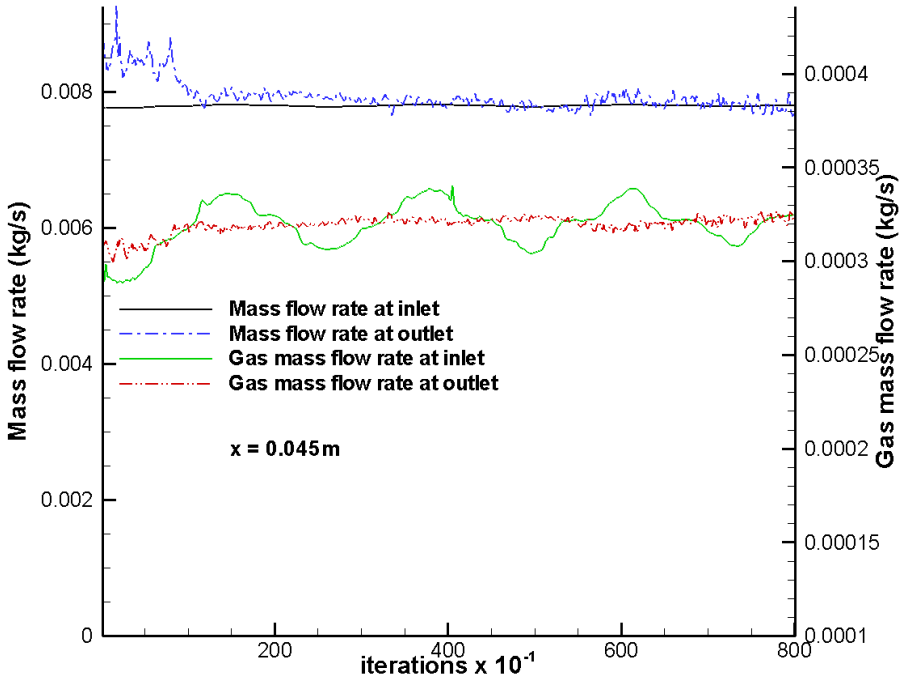

Figure 5.40: Mass flow rates for probe tip at $x = 0.045$m

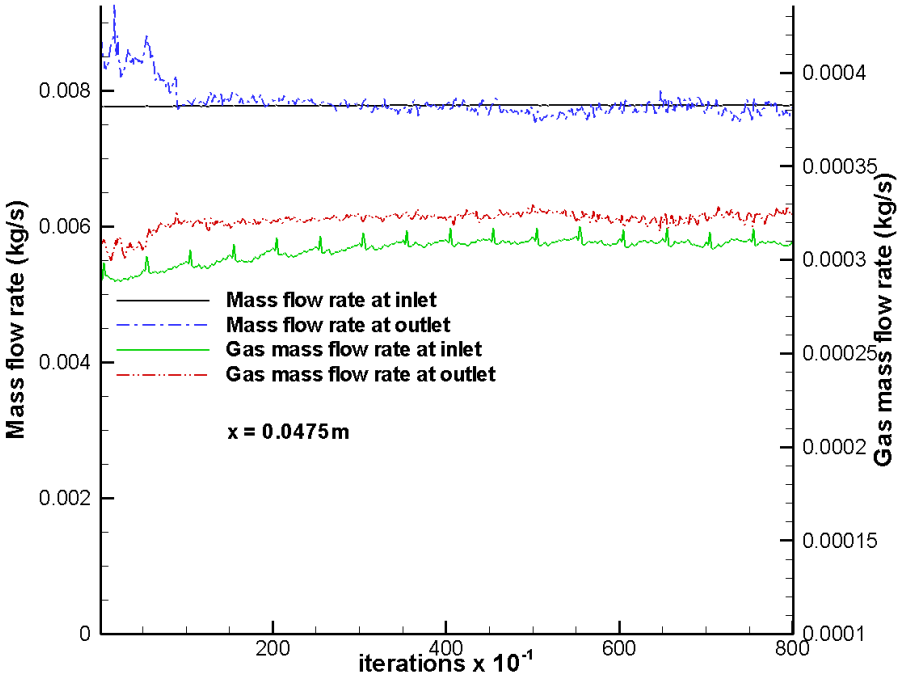

Figure 5.41: Mass flow rates for probe tip at $x = 0.0475$m

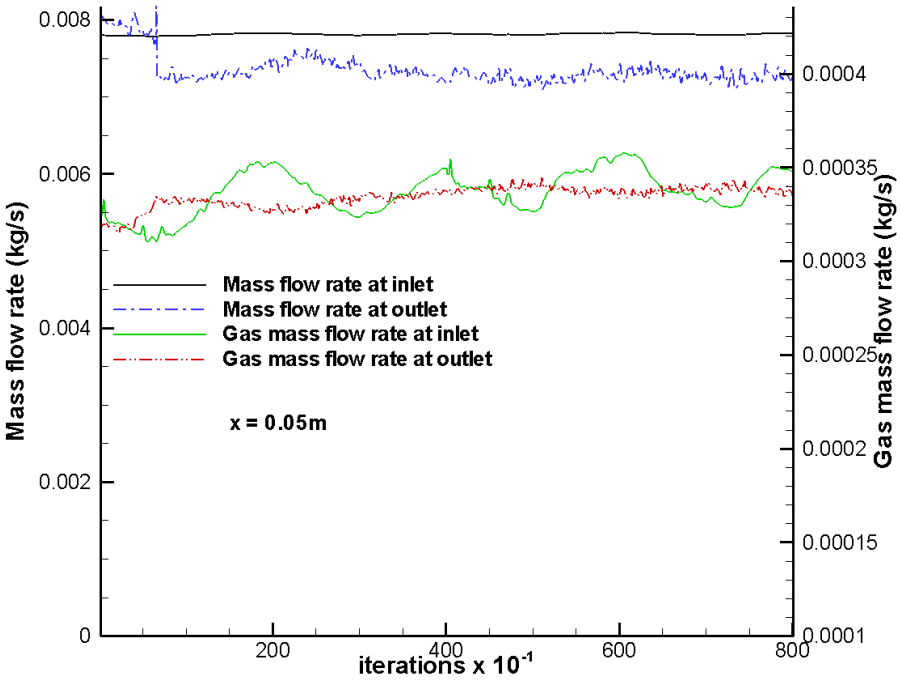

Figure 5.42: Mass flow rates for probe tip at $x = 0.05$m

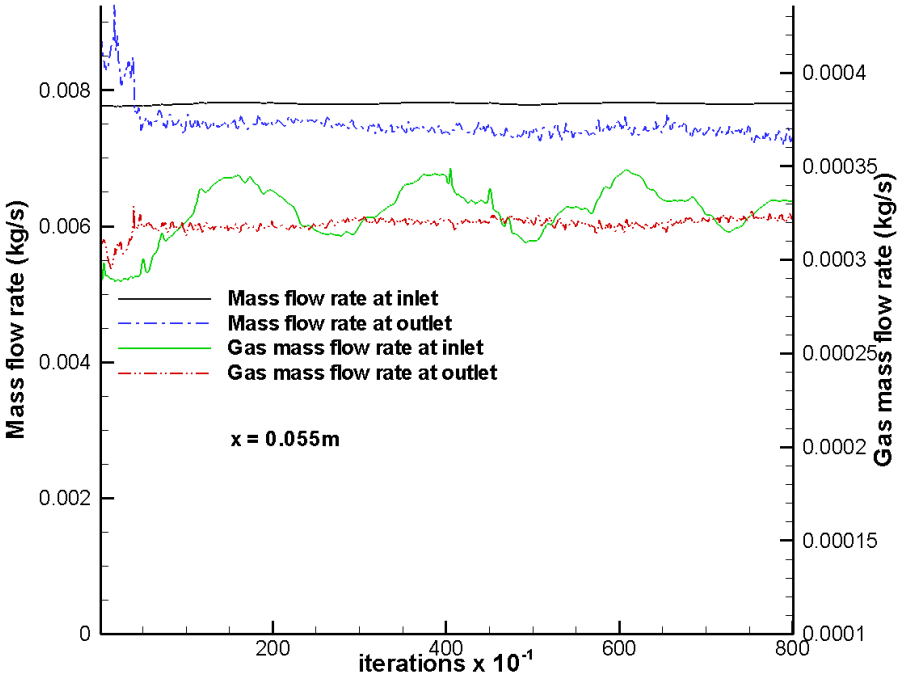

Figure 5.43: Mass flow rates for probe tip at $x = 0.055$m

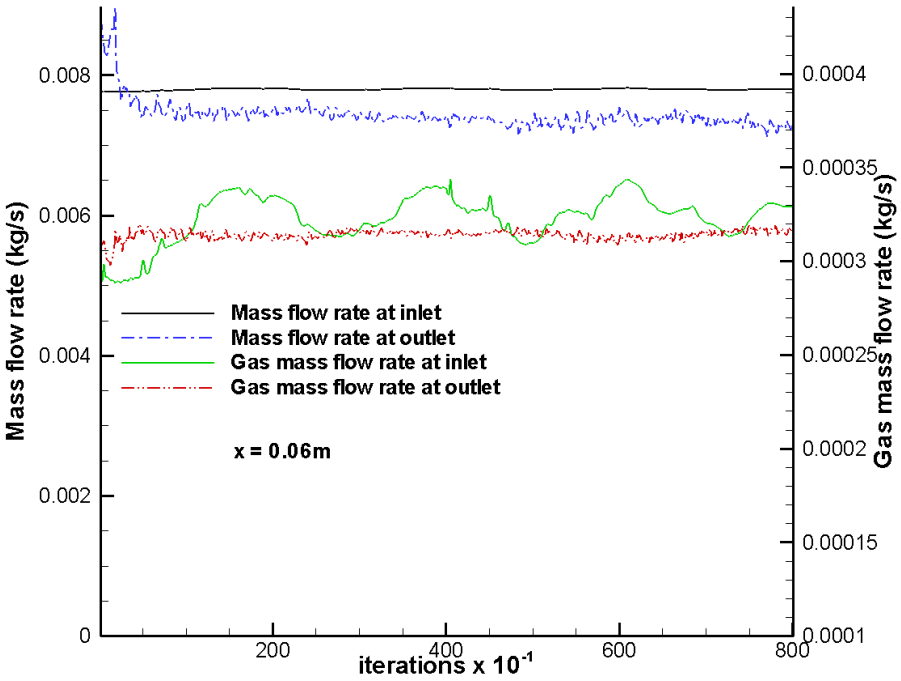

Figure 5.44: Mass flow rates for probe tip at $x = 0.06$m

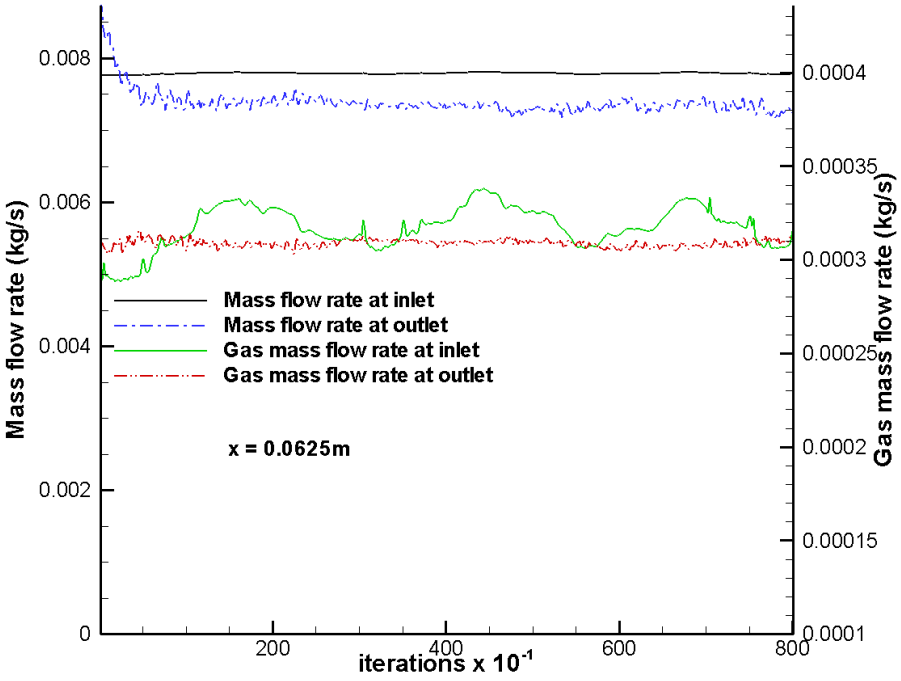

Figure 5.45: Mass flow rates for probe tip at $x = 0.0625$m

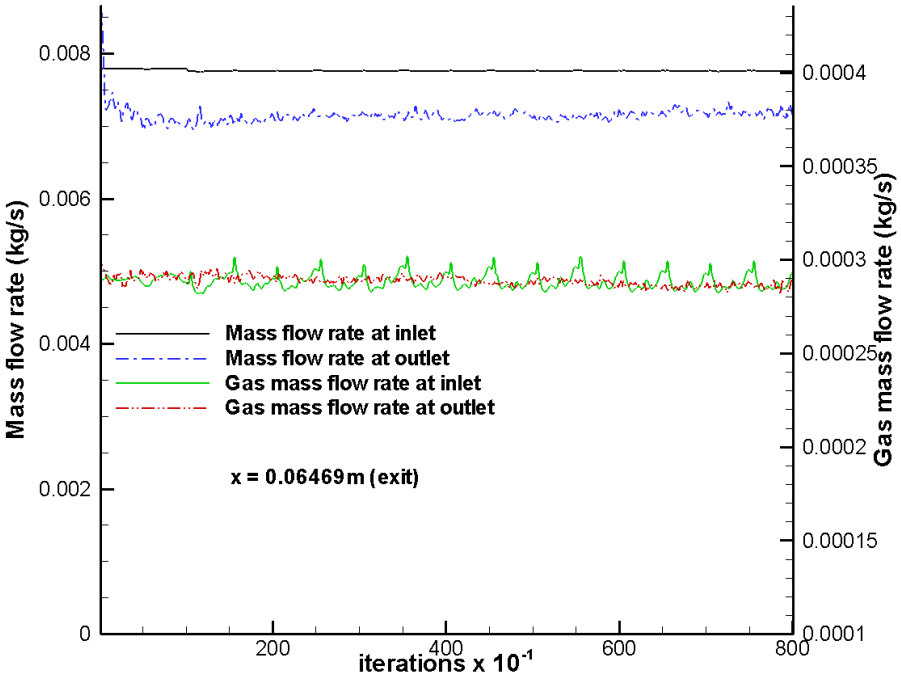

Figure 5.46: Mass flow rates for probe tip at $x = 0.06469$m (exit)

the outlet approaches the inlet value like the baseline does where the probe is wholly within the liquid core. But for the cases where the probe is not wholly within the liquid core, the total mass flow rate at the outlet approaches a lower value than that at the inlet. That is probably because that the intrusion of the probe requires a much longer time period for the flow to reach the steady state. Also, the immersed boundary method "blanks out" center cells and interpolates flow variables (see Appendix E). This treatment is not necessary conservative.

5.3.4 Concluding Remarks

Simulations of the transient, three-dimensional, two-phase flow within the "out-in" injector with plenum chamber and with the intrusion of the probe have been performed, and the results compared with experimental pressure measurements, theoretical analyses and the baseline result of Case 4 in Section 5.2. The flow pattern and the pressure distribution are very similar to the baseline results of Case 4 in Section 5.2 when the probe is wholly within the liquid core. But the two-phase mixture is more homogeous at the exit-plane if the probe tip is in the two-phase fluid area, and the flow is more unsteady. And there is a pressure drop near the probe tip's location in these cases. These features imply that the intrusion of the probe does affect the flowfield if the probe tip is in the two-phase area, instead of the liquid core. This effect could explain some of the discrepancies evidenced in the shape of the pressure distributions in the two-phase mixing region but does not explain the discrepancies evidenced in the absolute pressure level in the injector.

5.4 Crossflow Simulations

In order to further facilitate the use of the aerated-liquid jets in practical applications, such as a scramjet combustor, a detailed characterization of the corresponding spray

plume and droplet properties in a crossflow enviroment is needed. The effects of freestream Mach number on the evolution of the spray structure is also examined, and results are compared with experimental imaging data.

Only one GLR mass ratio (4%) is chosen in the simulations, and turbulent flow is assumed. Subsonic boundary condition is used for inflow air. At the injection hole, all properties are fixed since flow is choked. Subsonic boundary condition is used for tunnel outflow. Table 5.6 lists all cases simulated in this section. All cases have same initial static pressure and temperature conditions for the tunnel. They are set to be 140 kPa and 293 K, respectively. The diameter of the injector hole is 1 mm.

Table 5.6: Description of crossflow simulations

Case	M_∞	Grid	Initial conditions for the injector hole
1	0.1	coarse grid	results of theoretical analysis
2	0.2	coarse grid	results of theoretical analysis
3	0.3	coarse grid	results of theoretical analysis
4	0.3	coarse grid	solution of injector simulation with Bernoulli BCs for gas and liquid at inlet
5	0.3	coarse grid	solution of injector simulation with Bernoulli BC for gas at 170 psia pressure at inlet
6	0.3	refined grid	solution of injector simulation with Bernoulli BC for gas at 170 psia pressure at inlet
7	0.3	refined grid	results of theoretical analysis

The Mach number of the freestream air, M_∞, in the subsonic wind tunnel varied from 0.1 to 0.2 and 0.3. Contour plots of liquid mass density ($\rho_l \alpha_l = \rho Y_l$) at the X-Z centerplane are compared with experimental shadowgraph images in the figures that follow. All contours are scaled from 1 to 3 kg/m^3. In the experiments, the jet-to-air momentum flux ratio q_0 is used and is defined as:

$$q_0 = \frac{\rho_l w_0^2}{\rho_\infty u_\infty^2}, \tag{5.1}$$

where w_0 is the injector exit velocity in injection direction when the GLR value

is assumed to be zero, and u_∞ is the freestream velocity. As discussed by Lin et al. [1; 2; 5; 7], the effective momentum flux ratio for the aerated-liquid jet is higher than q_0 and is difficult to quantify. In a $M_\infty = 0.3$ crossflow, the numerical calculation of the jet-to-air momentum flux ratio is 5.08 if the injector exit velocity is obtained from the previous injector simulations for GLR=4%. This calculated q_0 is close to the experiment ($q_0 = 5.0$), so we can use the injector solutions as the initial conditions for the jet hole. In $M_\infty = 0.1$ and 0.2 cases, the velocity of the freestream air is smaller that that of $M_\infty = 0.3$ case, so injector flow rate must change to keep constant q_0. Since the experimental conditions for $M_\infty = 0.1$ and 0.2 are not available for us, we can only use theoretical analysis results as the initial conditions for the jet hole.

5.4.1 Freestream Mach 0.1 Case

Fig. 5.47 presents the experimental shadowgraph for injection into a Mach 0.1 crossflow. From this shadowgraph, we can see that the two-phase flow is injected vertically into the wind tunnel. Then it bends in the streamwise direction under the drag force imposed by the freestream air and disperses into a spray plume due to the breakup of the liquid into small droplets. The shadowgraph shows that the spray hits the top wall of the wind tunnel test section at around the $\frac{x}{d_0} = 50$ cross section plane. Some liquid concentrates near the top wall downstream of the impingement points as indicated by the darker region in the shadowgraph. Fig. 5.48 shows predicted liquid mass density contours at the X-Z centerplane for Case 1. Like the experimental shadowgraph, the liquid mass density contours show that the two-phase flow injects into the crossflow vertically as a spray plume. There are several differences between the shadowgraph image and the numerical results. First, the flow in the numerical simulation initially penetrates more vertically than indicated in the experiment. Secondly, the numerical results show a larger curvature of the spray in the streamwise

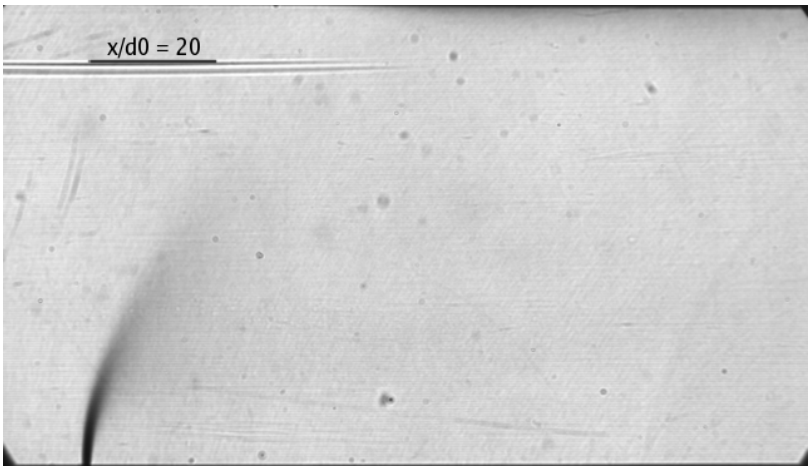

Figure 5.47: Shadowgraph, $M_\infty = 0.1$, GLR=4%, $q_0 = 5.0$

Figure 5.48: Liquid mass density contours, X-Z centerplane, Case 1 (analysis)

direction. Thus, the calculated two-phase flow does not hit the top wall of the wind tunnel. Finally, the numerical results show less lateral dispersion of the plume at the furthest downstream section. Fig. 5.49 shows predicted liquid mass density contours at the $\frac{x}{d_0} = 30$ cross section for Case 1. The spray plume in the cross section shows a horseshoe-shaped structure for the aerated-liquid jets. This structure results from the interaction between the freestream air and the blockage of the aerated-liquid jet. The resulting axial vortices enhance mixing by carrying liquid from the upper portion of the spray plume toward the bottom plate of the wind tunnel. Also, the peak liquid mass is located away from the center plane.

Figure 5.49: Liquid mass density contours, $\frac{x}{d_0} = 30$ cross section, Case 1 (analysis)

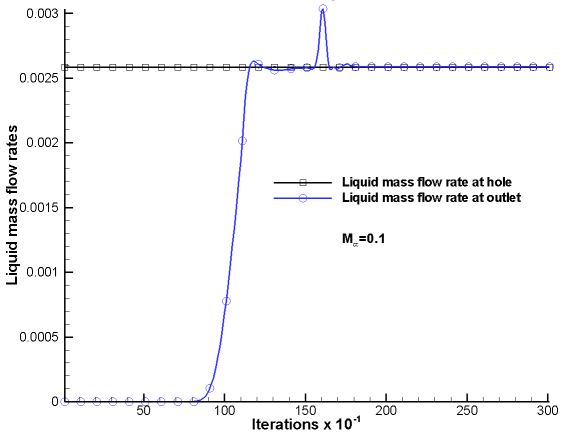

Figure 5.50: Liquid mass flow rates, Case 1 (analysis)

Fig. 5.50 shows inlet and exit liquid mass flow rates for Case 1. Good mass conservation is shown for these cases once a statistically steady state is reached. The code is started with first order spatial accuracy, and is altered to second order spatial accuracy after 1500 iterations. This explains the occurrence of the spike in the liquid mass flow rate at outlet near 1500 iterations. This occurs in all cases in this section.

5.4.2 Freestream Mach 0.2 Case

Fig. 5.51 presents the experimental shadowgraph for freestream Mach number of 0.2. Like the $M_\infty = 0.1$ case, we can see that the two-phase flow injects into the wind tunnel vertically, then bends in the streamwise (x) direction and disperses into a spray

plume. Since the freestream air velocity is larger, the drag on the two-phase flow is larger, and it forces the spray to curve towards flow direction more quickly. This results in a more dispersed spray plume and a lower penetration.

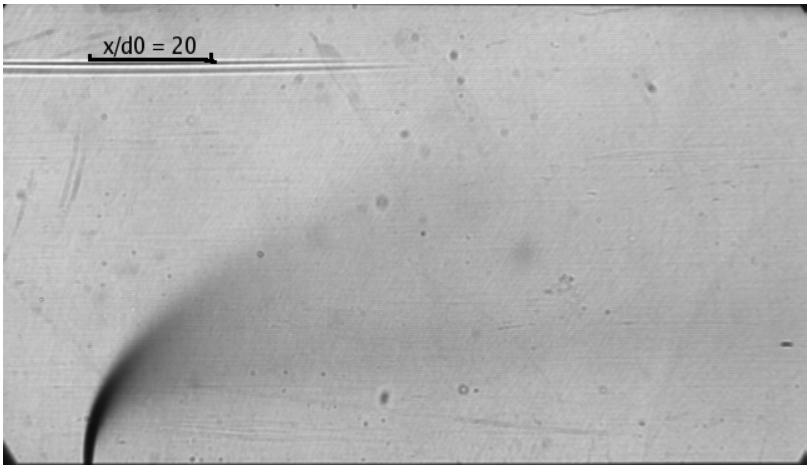

Figure 5.51: Shadowgraph, $M_\infty = 0.2$, GLR=4%, q_0 = 5.0

Figure 5.52: Liquid mass density contours, X-Z centerplane, Case 2 (analysis)

Fig. 5.52 shows calculated liquid mass density contours at the X-Z centerplane for Case 2. Like the experimental shadowgraph, the numerical liquid mass density contours show that the two-phase flow injects into the crossflow vertically as a spray plume. Still, the numerical spray plume is less dispersed laterally than indicated the experiment.

Figure 5.53: Liquid mass density contours, $\frac{x}{d_0} = 50$ cross section, Case 2 (analysis)

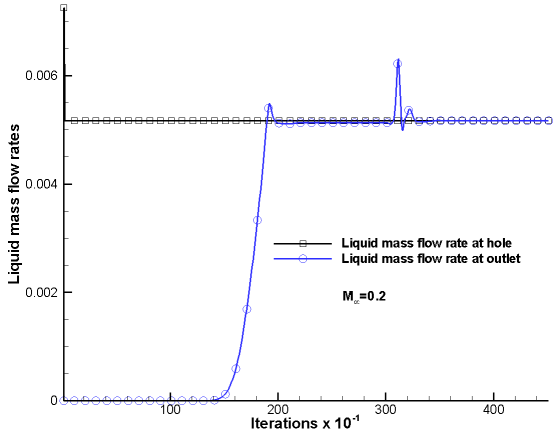

Figure 5.54: Liquid mass flow rates, Case 2 (analysis)

Fig. 5.53 shows predicated liquid mass density contours at the $\frac{x}{d_0} = 50$ cross section for Case 2. The spray plumes in the cross section show an asymmetric horseshoe-shaped structure for the aerated-liquid jets. This asymmetry is probably caused by the following reasons. First, the grid is not symmetric about the X-Z centerplane. Secondly, there is no symmetric condition enforced in the numerical calculation. Finally, this asymmetry is a consequence of the capturing of the natural modes of jet instability where the eddy viscosity is not large enough to initially suppress them.

Fig. 5.54 shows inlet and exit liquid mass flow rates for Case 2. Again, good mass conservation is shown once a statistically steady state is reached.

5.4.3 Freestream Mach 0.3 Cases

Fig. 5.55 presents the experimental shadowgraph image for a freestream Mach number of 0.3. Like the previous cases, we can see that the two-phase flow injects into the wind tunnel vertically, then bends toward the tunnel floor and disperses into a spray plume. Since the freestream air velocity is the largest, the drag force imposed on the two-phase flow is the largest, and it forces the two-phase flow more quickly toward the freestream flow direction and results in the least penetration of the jet.

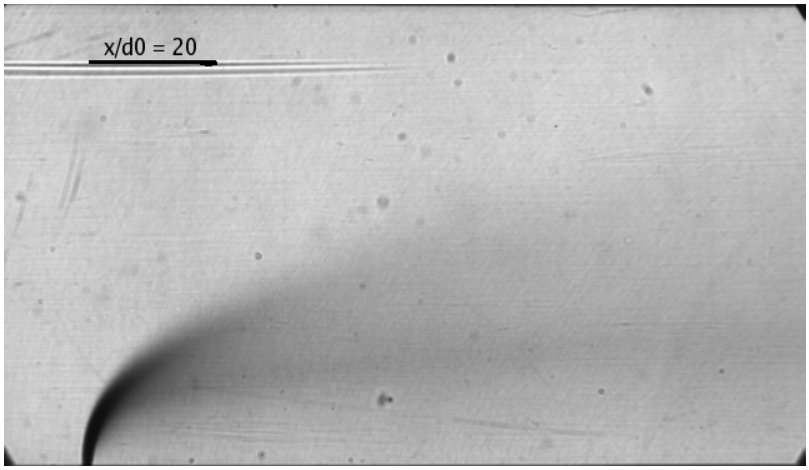

Figure 5.55: Shadowgraph, $M_\infty = 0.3$, GLR=4%, q_0 = 5.0

Figure 5.56: Liquid mass density contours, X-Z centerplane, Case 3 (analysis)

Figure 5.57: Liquid mass density contours, X-Z centerplane, Case 4 (Bernoulli BCs)

Figure 5.58: Liquid mass density contours, X-Z centerplane, Case 5 (170 psia)

Fig. 5.56-Fig. 5.58 show liquid mass density contours at the X-Z centerplane for Cases 3-5. All numerical liquid mass density contours show that the two-phase flow injects into the crossflow and forms a less dispersed spray plume. Numerical results show more expansion of the two-phase flow right after the injector exit. This may be due to the fact that the pressure levels at the injector exit in the simulations and in the theoretical predictions are higher than those measured in the experiment. The result of Case 5 (170 psia gas pressure) shows the highest penetration among the numerical results. The result of Case 4 (both Bernoulli BCs) shows a lower penetration

Figure 5.59: Liquid mass density contours, X-Z centerplane, Case 6 (170 psia)

Figure 5.60: Liquid mass density contours, X-Z centerplane, Case 7 (analysis)

compared with Case 5. This is probably due to a lower injector exit pressure of Case 4. Case 3 (theoretical analysis) has almost the same injector exit pressure as Case 5 does, but the penetration height is lower than that of Case 5. The two-phase jet of Case 3 is uniform at the injector exit plane, as properties were obtained by the one-dimensional analysis of Appendix D. In contrast, the exit conditions for Cases 4 and 5 were obtained by time-averaging exit plane results from simulations of the actual flow within the injector. These different injector exit conditions may cause the difference in the penetration heights among these three cases.

Fig. 5.59 and Fig. 5.60 show numerical results of liquid mass density contours at

centerplane for Cases 6 and 7. These refined-grid results show smoother liquid mass density contours. Liquid mass density contours of Case 6 (170 psia gas pressure) agrees best with the experimental shadowgraph right after injection.

Fig. 5.61-Fig. 5.65 show numerical results of liquid mass density contours at the $\frac{x}{d_0} = 50$ cross section for Cases 3-7. Again, the spray plumes in the cross section show a horseshoe-shaped structure for the aerated-liquid jets. Liquid mass density contours obtained on the coarse grid are more narrowly distributed about the centerplane, while those obtained on the refined-grid are distributed further away from the centerplane. Also, the results obtained using the theoretical exit plane conditions are more symmetric about the centerplane.

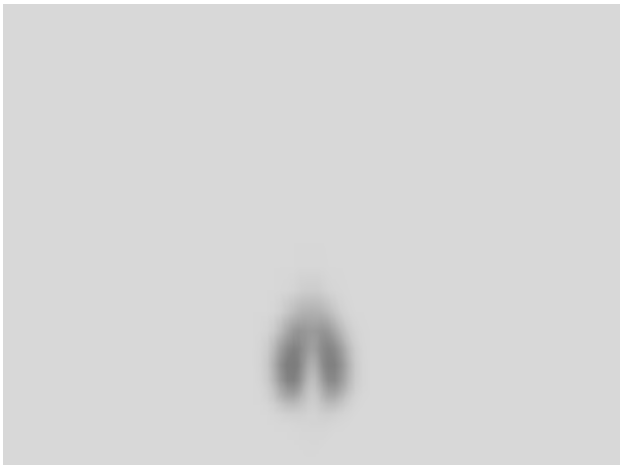

Figure 5.61: Liquid mass density contours, $\frac{x}{d_0} = 50$ cross section, Case 3 (analysis)

Fig. 5.66 shows the velocity streamlines at the $\frac{x}{d_0} = 50$ cross-sectional plane for Case 5. As mentioned earlier in Section 5.4.1, the axial vortices enhance mixing by carrying two-phase fluid from the upper portion of the spray plume toward the bottom plate of the wind tunnel. These streamlines further explain the formation of the horse-shaped structure for the aerated-liquid jet.

Figure 5.62: Liquid mass density contours, $\frac{x}{d_0} = 50$ cross section, Case 4 (Bernoulli BCs)

Figure 5.63: Liquid mass density contours, $\frac{x}{d_0} = 50$ cross section, Case 5 (170 psia)

Figure 5.64: Liquid mass density contours, $\frac{x}{d_0} = 50$ cross section, Case 6 (170 psia)

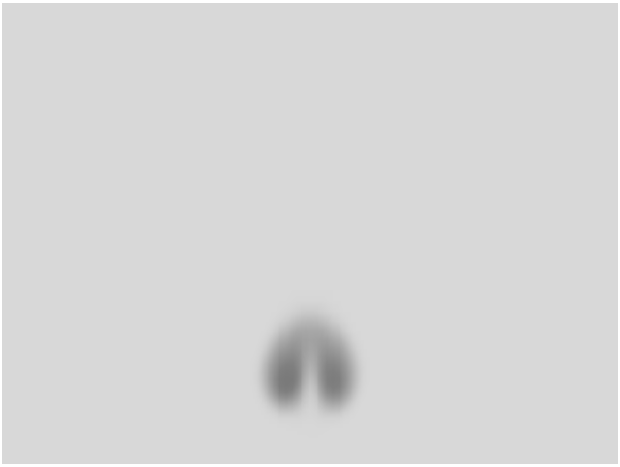

Figure 5.65: Liquid mass density contours, $\frac{x}{d_0} = 50$ cross section, Case 7 (analysis)

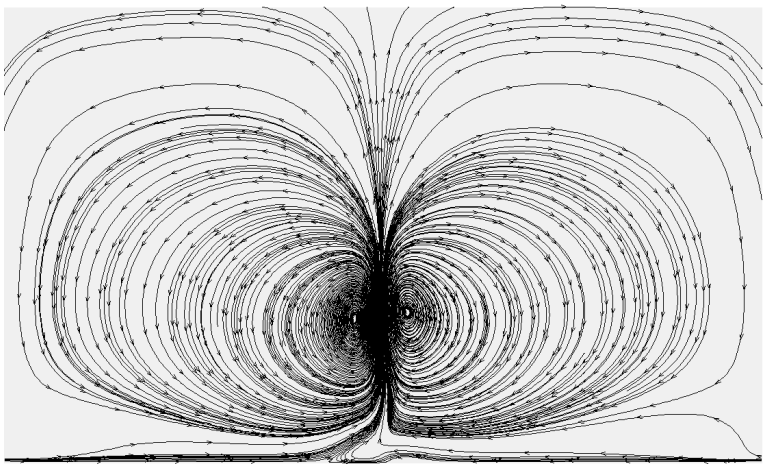

Figure 5.66: Velocity streamlines, $\frac{x}{d_0} = 50$, Case 5 (170 psia)

Fig. 5.67-Fig. 5.71 show inlet and exit liquid mass flow rates for Cases 3-7. Again, good mass conservation is shown once a statistically steady state is reached.

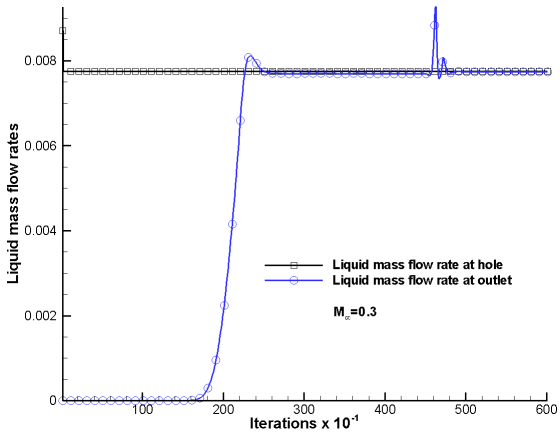

Figure 5.67: Liquid mass flow rates, Case 3 (analysis)

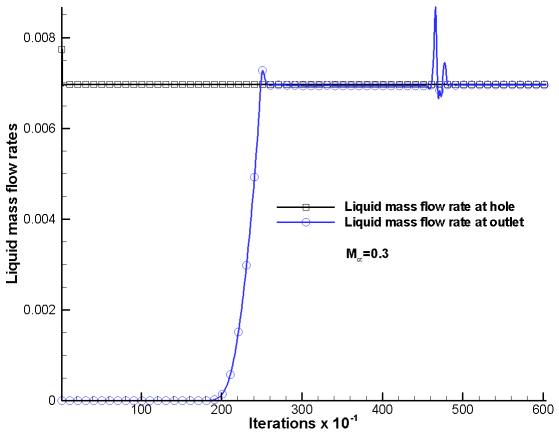

Figure 5.68: Liquid mass flow rates, Case 4 (Bernoulli BCs)

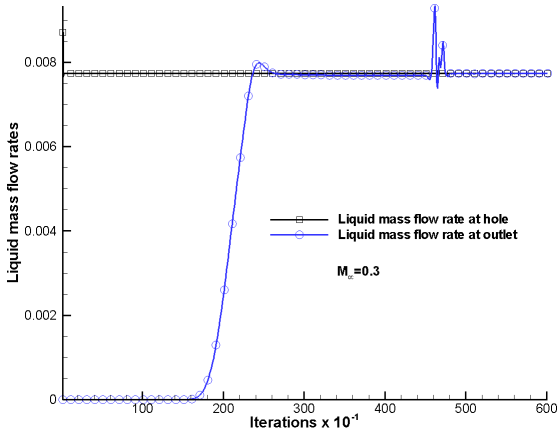

Figure 5.69: Liquid mass flow rates, Case 5 (170 psia)

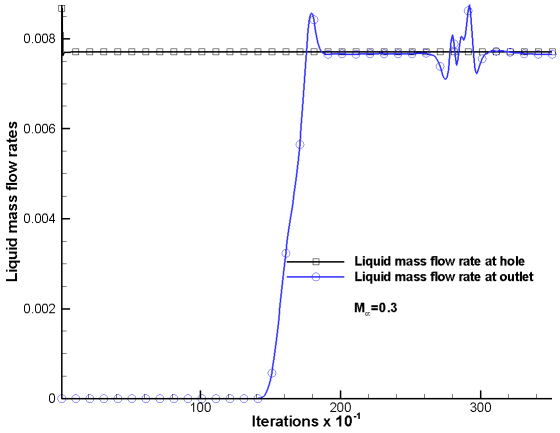

Figure 5.70: Liquid mass flow rates, Case 6 (170 psia)

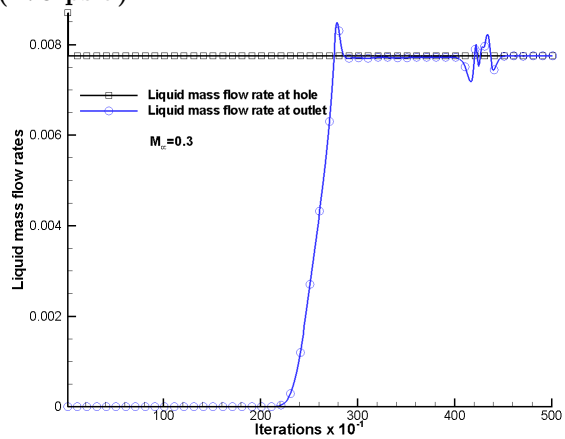

Figure 5.71: Liquid mass flow rates, Case 7 (analysis)

5.4.4 Structures of Aerated-liquid Jets

An important feature of the aerated-liquid jet is its penetration height at a particular cross-sectional plane. The penetration height is the top point of the visualized aerated-liquid jet at a particular cross-sectional plane. Fig. 5.72 shows the aerated-liquid jet penetration heights of different freestream Mach numbers and different GLR values measured from the experiments.

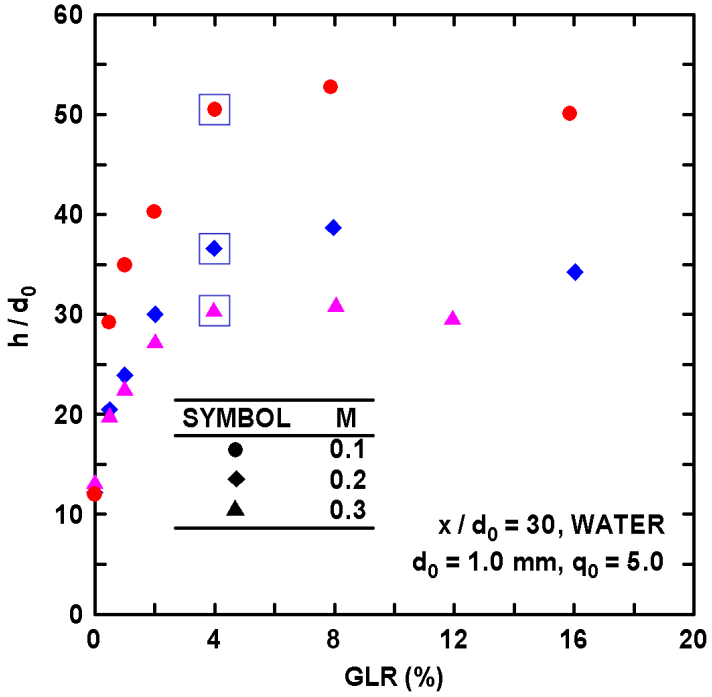

Figure 5.72: Experimental data, aerated-liquid jet penetration heights

Table 5.7: Aerated-liquid jet penetration height ($\frac{h}{d_0}$) at $\frac{x}{d_0} = 30$

M_∞	Shadowgraph	Cases 1-3 (analysis)	Case 4 (Bernoulli)	Case 5 (170 psia)	Case 6 (refined)	Case 7 (refined)
0.1	50.5	39.9				
0.2	36.5	31.4				
0.3	30.5	25.2	28.2	30.8	26.4	21.9

Table 5.7 lists the penetration heights of the aerated-liquid jets of the experimental shadowgraphs and the numerical liquid mass density contours. In the shadowgraph

and liquid mass density contours, the penetration height is taken to be the the top edge of the dark color area. As shown in this table, at $\frac{x}{d_0} = 30$ plane, the penetration height of Case 5 (170 psia gas pressure) is the most closest to the penetration height of the experimental shadowgraph, and Case 7 (refined grid, theoretical analysis) has the lowest penetration height.

To summarize the typical structure of the aerated-liquid jets, Fig. 5.73-Fig. 5.75 show the three-dimensional distributions of liquid mass density for the aerated-liquid jets with $M_\infty = 0.1, 0.2$, and 0.3, respectively. Half planes of the cross section and the centerplane are used to display three-dimensional structures of the aerated-liquid jets. As shown, the liquid mass density distributions in the cross-sectional planes are diluted as streamwise distance $(\frac{x}{d_0})$ increases.

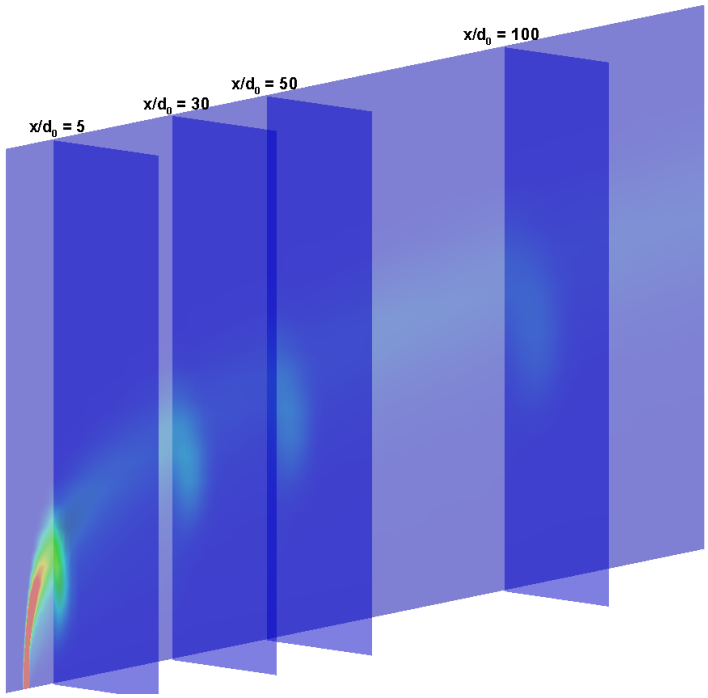

Figure 5.73: Liquid mass density contours, 3-D, Case 1 (analysis)

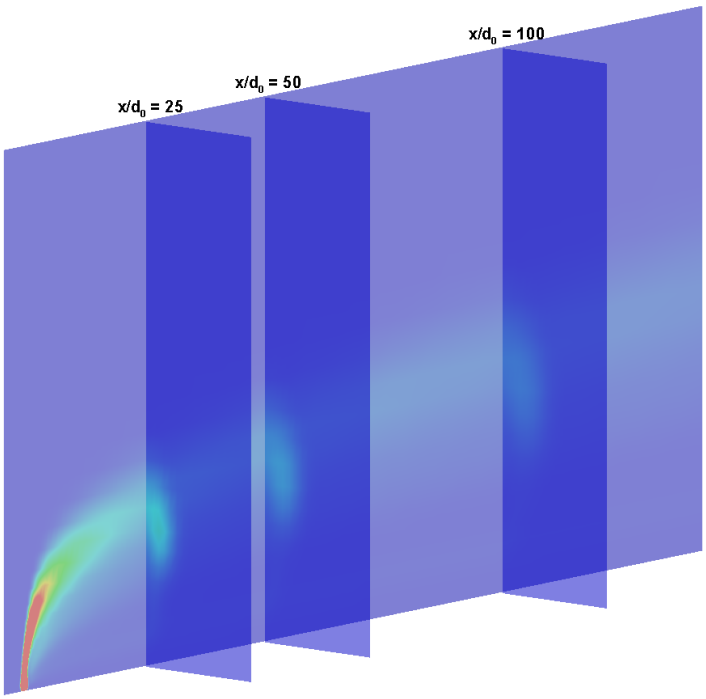

Figure 5.74: Liquid mass density contours, 3-D, Case 2 (analysis)

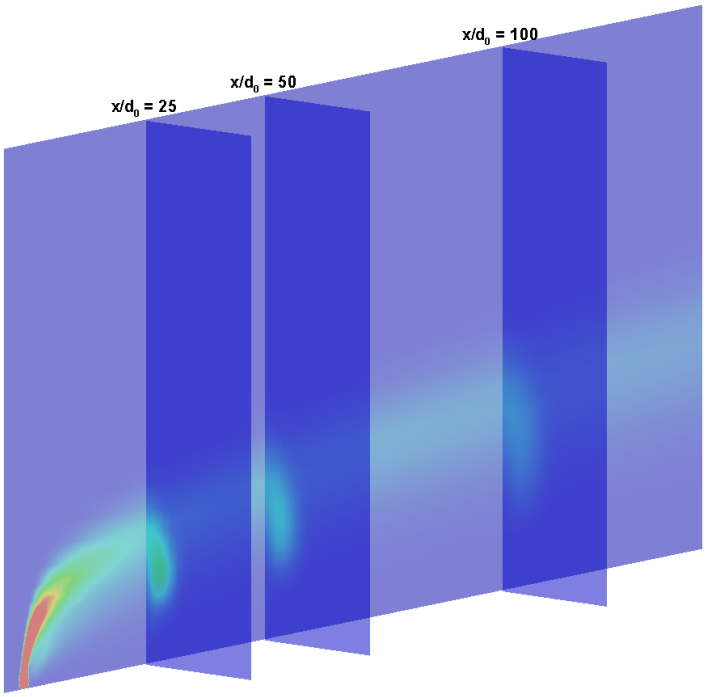

Figure 5.75: Liquid mass density contours, 3-D, Case 3 (analysis)

5.4.5 Concluding Remarks

Simulations of the thermal non-equilibrium, turbulent, three-dimensional, two-phase flow within the subsonic crossflow domain have been performed, and the results compared with experimental shadowgraphs. The two-phase flow vertically injects into the crossflow domain. Then it bends towards the streamwise direction under the drag force imposed by the freestream air and disperses into a spray plume due to the breakup of the liquid into small droplets. With increases in freestream Mach number, the penetration height of the aerated-liquid jet decreases. In the cross-sectional planes, the liquid mass contours show a horseshoe-shape structure of the jet, and are diluted with increases in the streamwise distance. For freestream Mach 0.3 cases, the penetration height of Case 5 (170 psia gas pressure, non-uniform jet inflow) is closest to the experimental shadowgraph, and Case 6 (refined grid, 170 psia gas pressure, non-uniform jet inflow) agrees best with the shadowgraph on the jet profile right after injection. These results provide additional evidence that the previous injector simulations are valid and credible.

5.5 Cross-flow Simulations with Droplet Transport Model

In the crossflow experiment, many droplet properties are measured or calculated. But not all of these properties can be calculated in the simulations with the mixture model. For example, separate liquid droplet velocities can not be obtained, nor can predictions of average droplet size. In order to understand more liquid properties, a droplet transport model is implemented in a decoupled fashion in this work. In this model, one liquid mass continuity equation in conservative form, along with three liquid momentum equations discretized in divergence form, are solved in a similar matter used in the mixture model. No droplet energy equation needs to be solved

since the droplet temperature is assumed to be frozen at the injector exit value. Droplet equations are solved separately from the mixture equations. As a first step, the droplet distribution is assumed to be monodisperse with an inputted diameter.

Only one GLR mass ratio (4%) and one freestream Mach number (0.3) are chosen for the coarse grid simulations, and turbulent flow is assumed. Table 5.8 lists all cases simulated in this section. All cases are initialized from the solution of Case 5 in the previous section. The injector exit plane conditions are obtained from the solution of Case 4 in Section 5.2. Other conditions are set to be the same as described in the previous section.

Table 5.8: Description of crossflow simulations with droplet transport model

Case	Droplet diameter size d_{drop} (μm)
1	5
2	10
3	20
4	40

Fig. 5.76-Fig. 5.79 show liquid mass density contours at the X-Z centerplane for Cases 1-4. All numerical liquid mass density contours show that the two-phase flow injects into the crossflow and forms a dispersed spray plume Numerical results show more expansion of the two-phase flow right after the injector exit. With increases in droplet diameter size d_{drop}, the two-phase flow injects into the crossflow less vertically and bends in the streamwise direction more quickly. The contours become less smooth in the edge of the dark area. Also, liquid mass density contours become darker with increases in droplet diameter size. This indicates that more liquid is concentrated on the centerplane when droplet diameter size increases.

Figure 5.76: Liquid mass density contours, $d_{\text{drop}} = 5\mu\text{m}$, Case 1

Figure 5.77: Liquid mass density contours, $d_{\text{drop}} = 10\mu\text{m}$, Case 2

Figure 5.78: Liquid mass density contours, $d_{\text{drop}} = 20\mu\text{m}$, Case 3

Figure 5.79: Liquid mass density contours, $d_{\text{drop}} = 40\mu\text{m}$, Case 4

Figure 5.80: Liquid mass density contours, $\frac{x}{d_0} = 50$, $d_{\text{drop}} = 5\mu\text{m}$, Case 1

Figure 5.81: Liquid mass density contours, $\frac{x}{d_0} = 50$, $d_{\text{drop}} = 10\mu\text{m}$, Case 2

Figure 5.82: Liquid mass density contours, $\frac{x}{d_0} = 50$, $d_{\text{drop}} = 20\mu\text{m}$, Case 3

Figure 5.83: Liquid mass density contours, $\frac{x}{d_0} = 50$, $d_{\text{drop}} = 40\mu\text{m}$, Case 4

Fig. 5.80-Fig. 5.83 show predicated liquid mass density contours at the $\frac{x}{d_0} = 50$ cross section for Cases 1-4. The spray plumes in the cross section show that more liquid concentrates on the X-Z centerplane, and the horseshoe-shaped structure observed in the previous section fades away with increases in the droplet diameter size. This indicates that liquid material accumulates to the centerplane. There are two possible reasons to explain the clustering.

First reason is described as follows. Fig. 5.84 and Fig. 5.85 show vertical and lateral velocity contours at the $\frac{x}{d_0} = 50$ cross-sectional plane for Case 5 of the mixture model.

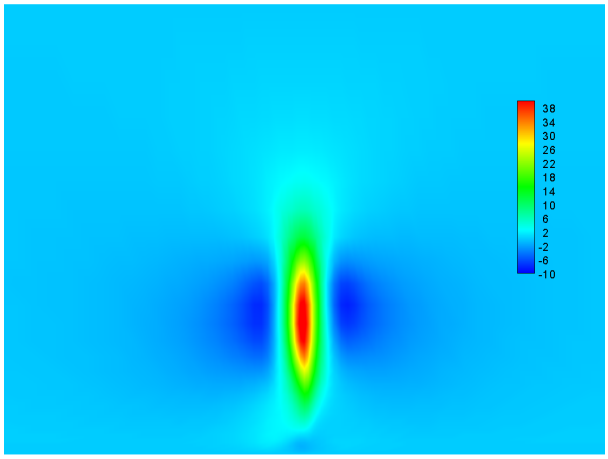

Figure 5.84: Vertical velocity contours, mixture, Case 5 (170 psia)

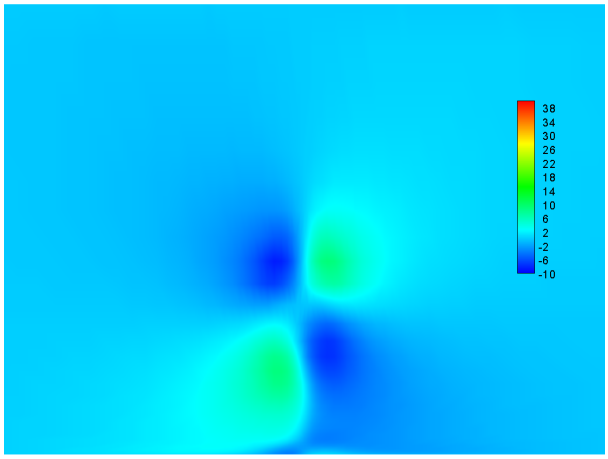

Figure 5.85: Lateral velocity contours, mixture, Case 5 (170 psia)

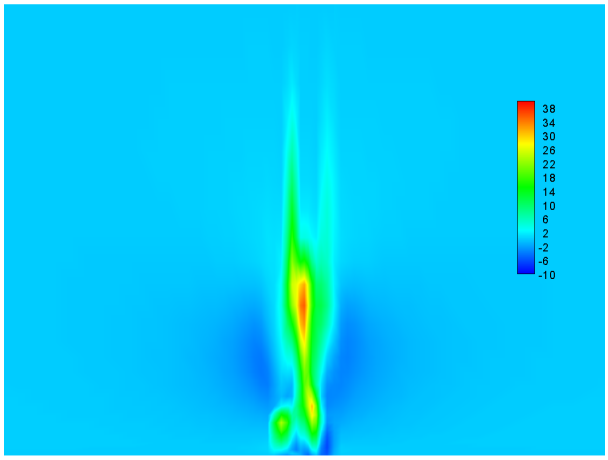

Figure 5.86: Vertical velocity contours, $d_{\text{drop}} = 20\mu\text{m}$, $\frac{x}{d_0} = 50$

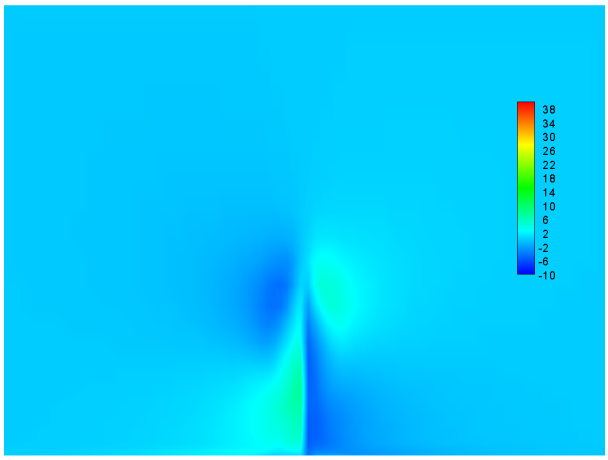

Figure 5.87: Lateral velocity contours, $d_{\text{drop}} = 20\mu\text{m}$, $\frac{x}{d_0} = 50$

Fig. 5.86 and Fig. 5.87 show vertical and lateral velocity contours at the $\frac{x}{d_0} = 50$ cross-sectional plane for $d_{\text{drop}} = 20\mu$m of the droplet model. As shown, the magnitude of the vertical velocity is much larger than that of the lateral velocity. That implies that the drag force in vertical direction is much larger than the drag force in the lateral direction. Thus, in the droplet transport model, the two-phase flow disperses more in the vertical direction, but less in the lateral direction.

The second reason is mainly due to the lack of a pressure gradient term in the droplet momentum equations and the degenerate hyperbolic nature of disperse gas-particle flows equations discussed in Refs. [62–65]. In [64], a one-dimensional eigen-analysis shows that the particle equations have three equal eigenvalues indicating that the particle equations are hyperbolic. Because of this degeneracy in the eigensystem, information can only travel through the computational domain in the direction of the particle pathlines. Since there are no pressure forces in the particle equations, particle vacuums can exist. Also, as interactions between particles have been neglected, the particle paths can cross. Lagrangian methods can readily deal with particle paths that cross. Eulerian methods, however, sometimes generate solutions which are not only inaccurate but also physically incorrect. Examples are presented in [63; 64].

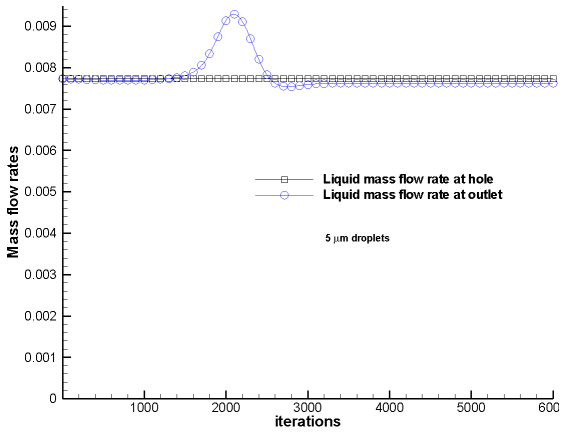

Figure 5.88: Liquid mass flow rates, Case 1 (5 μm)

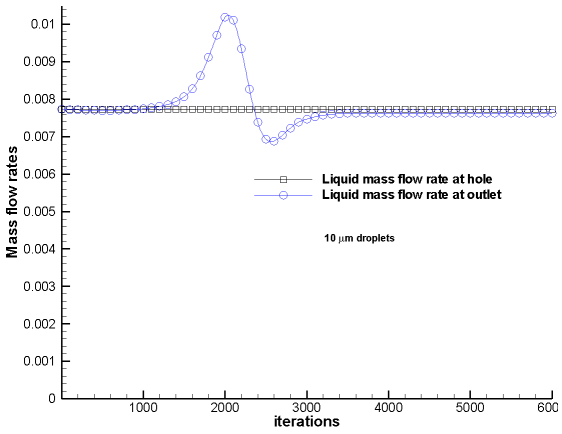

Figure 5.89: Liquid mass flow rates, Case 2 (10 μm)

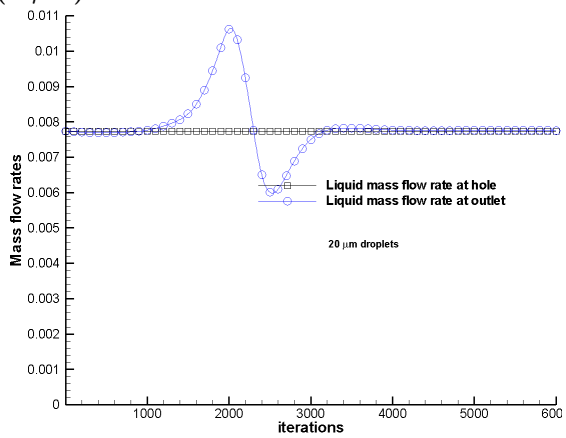

Figure 5.90: Liquid mass flow rates, Case 3 (20 μm)

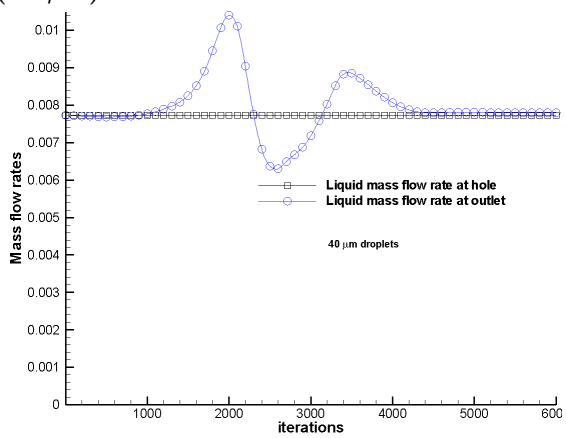

Figure 5.91: Liquid mass flow rates, Case 4 (40 μm)

Fig. 5.88-Fig. 5.91 show inlet and exit liquid mass flow rates for Cases 1-4. Again, good mass conservation is shown once a statistically steady state is reached.

Table 5.9 lists the penetration heights of the aerated-liquid jets of the experimental shadowgraph and the numerical liquid mass density contours. As shown in this table, at $\frac{x}{d_0} = 30$ plane, the penetration heights of Cases 1-3 are all close to that of the experimental shadowgraph, but the penetration heights of Case 4 is lower than others.

In this section, a droplet transport model is used in the simulations of the thermal non-equilibrium turbulent two-phase flow within the subsonic crossflow environment. The spray structure is similar to that in the previous section in the X-Z centerplane,

Table 5.9: Aerated-liquid jet penetration height ($\frac{h}{d_0}$) at $\frac{x}{d_0} = 30$

M_∞	Shadowgraph	Cases 1 (5 μm)	Case 2 (10 μm)	Case 3 (20 μm)	Case 4 (40 μm)
0.3	30.5	31.0	31.5	30.5	27.7

but is very different in the cross-sectional plane. The horseshoe-shaped structure observed in the previous section fades away with increases in the droplet diameter size, and liquid mass accumulates to the X-Z centerplane. This is mainly due to the lack of a pressure gradient term in the droplet momentum equations and the degenerate hyperbolic nature of disperse gas-particle flow equations.

Chapter 6

Conclusions

The present study makes an effort to understand the two-phase fluid dynamics characteristic of aerated-liquid injector and spray structures in the corresponding crossflow domain. Simulations of the transient, three-dimensional, two-phase flow within the "out-in" injector and the corresponding crossflow domain have been performed, and the results compared with experimental pressure measurements of the injector and shadowgraph of the crossflow. Several simulations are performed on three types of geometry (injector only, injector with plenum, and crossflow field) respectively.

For injector discharge tube simulations, three gas-to-liquid mass ratio (GLR) have been used: 2%, 4% and 8%. With increases in GLR, the aerating gas forces the liquid flow toward the centerline, inducing large-scale mixing that acts to break up the liquid jet well before the exit of the tube. Only at the lowest GLR value of 2% is a relatively intact liquid core predicted to exist, and then only under assumed laminar flow conditions. Predicted centerline pressure distributions are consistent with theoretical analyses that assume choked flow at the exit of the injector tube, but exhibit systematically higher absolute levels compared with the experimental data. The shape of the pressure distribution induced by gas injection is best predicted when turbulence effects are modeled and when very fine grids are used. Reasons behind the observed discrepancies may include such experimental factors as leakage in either the gas or liquid flow lines and changes in the flow characteristics due to the presence of the probe.

Only one GLR mass ratio (4%) has been chosen in the injector simulations with

plenum part, and laminar flow has been assumed. The flow pattern is very similar to those simulations with discharge tube cases. The aerating gas forces the liquid flow toward the centerline, and breaks up the liquid jet well before the exit of the tube. Predicted centerline pressure distributions with all boundary conditions except one (Bernoulli BC at a higher gas pressure at inlet) are close to the experimental data, but are lower than the theoretical analyses that assume choked flow at the exit of the injector tube. The total mass gas rate at outlet in these cases approaches the total mass gas rate at outlet, but the gas mass rate at outlet approaches a value lower than the expected value. Predicted centerline pressure levels for the case with the Bernoulli BC at a higher gas pressure at inlet agree well with the theoretical analysis, but are consistently larger than the experimental data. The gas mass flow rate at outlet for this case does approach to the expected value, however. These results are consistent with those of the discharge tube cases. This imply that inaccuracies exhibited in company with experimental data are not the result of simplifications in the injector geometry.

Only one GLR mass ratio (4%) has been chosen in the injector simulations with plenum chamber and with the intrusion of the probe, and laminar flow has been assumed. The flow pattern and the pressure distribution are very similar to the baseline results of Case 4 in Section 5.2 when the probe is wholly within the liquid core. But the two-phase mixture is more homogeous at the exit-plane if the probe tip is in the two-phase mixing region. And there is a pressure drop near the probe tip's location in these cases. These features imply that the intrusion of the probe does affect the flowfield if the probe tip is in the two-phase area, instead of the liquid core. This effect could explain some of the discrepancies evidenced in the shape of the pressure distributions in the two-phase mixing region but does not explain the discrepancies evidenced in the absolute pressure level in the injector.

One GLR mass ratio (4%) and three freestream Mach numbers (0.1, 0.2 and 0.3) have been chosen in the crossflow simulations, and thermal non-equilibrium turbulent flow has been assumed. The two-phase flow vertically injects into the crossflow domain. Then it bends towards the streamwise direction under the drag force imposed by the freestream air and disperses into a spray plume due to the breakup of the liquid into small droplets. With increases in freestream Mach number, the penetration height of the aerated-liquid jet decreases. In the cross-sectional planes, the liquid mass contours show a horseshoe-shape structure of the jet, and are diluted with increases in the streamwise distance. For freestream Mach 0.3 cases, the penetration height of Case 5 (170 psia gas pressure) is closest to the experimental shadowgraph, and Case 6 (refined grid, 170 psia gas pressure) agrees best with the shadowgraph on the jet profile right after injection. These results provide additional evidence that the previous injector simulations are valid and credible.

One GLR mass ratio (4%) and one freestream Mach number (0.3) have been chosen in the crossflow simulations using droplet transport model, and thermal non-equilibrium turbulent flow has been assumed. The spray structure is similar to that in the previous section in the X-Z centerplane, but is very different in the cross-sectional plane. The horseshoe-shaped structure observed in Section 5.4 fades away with increases in the droplet diameter size, and liquid mass accumulates to the X-Z centerplane. This is mainly due to the lack of a pressure gradient term in the droplet momentum equations and the degenerate hyperbolic nature of disperse gas-particle flows equations.

Some future work will be focused on the following areas:

1. to improve the mass conservation properties of the immersed boundary method;

2. to include particulate dispersion terms in the droplet momentum equations to improve the solution of the droplet transport model;

3. to develop a fully coupled gas-droplet approach for better spray prediction;

4. to use the two-phase flow simulation techniques for future simulations of spray development within hydrocarbons-fuelled scramjet combustors.

References

1. Lin, K. C., Kirkendall, K. A., Kennedy, P. J., and Jackson, T. A., "Spray Structures of Aerated-Liquid Fuel Jets in Supersonic Crossflows," AIAA Paper 99-2374, June 1999.

2. Lin, K. C., Kennedy, P., J., and Jackson, T. A., "Spray Penetration Heights of Angle-Injected Aerated Liquid Jets in Supersonic Crossflows," AIAA Paper 2000-0194, January 2000.

3. Lin, K. C., Kennedy, P., J., and Jackson, T. A., "Structures of Aerated Liquid Fuel Jets Interacting with a Shock Train in Supersonic Crossflows," Eighth international conference on liquid atomization and spray systems, June 2000.

4. Lin, K. C., Kennedy, P., J., and Jackson, T. A., "Liquid JP-7 Combustion in a Scramjet Combustor," AIAA Paper 2000-3581, July 2000.

5. Lin, K. C., Kennedy, P., J., and Jackson, T. A., "Spray Structures of Aerated-Liquid Jets in Subsonic Crossflows," AIAA Paper 2001-0330, January 2001.

6. Lin, K. C., Kennedy, P., J., and Jackson, T. A., "Structures of Internal Flow and the Corresponding Spray for Aerated-Liquid Injectors," AIAA Paper 2001-3569, June 2001.

7. Lin, K. C., Kennedy, P., J., and Jackson, T. A., "Penetration Heights of Liquid Jets in High-Speed Crossflows," AIAA Paper 2002-0873, January 2002.

8. Lin, K. C., Kennedy, P., J., and Jackson, T. A., "Structures of Aerated-Liquid Jets in High-Speed Crossflow," AIAA Paper 2002-3178, June 2002.

9. Tian, M. and Edwards, J., "Numerical Simulation of Transient Two-Phase Flow within Aerated-Liquid Injectors," AIAA Paper 2003-4266, June 2003.

10. Turkel, E., "Preconditioned Methods for Solving the Incompressible and Low Speed Compressible Equations," *Journal of Computational Physics*, Vol. 72, 1987, pp. 277–298.

11. Choi, Y. H. and Merkle, C. L., "The Application of Preconditioning in Viscous Flows," *Journal of Computational Physics*, Vol. 105, 1993, pp. 207–223.

12. Weiss, J. M. and Smith, W. A., "Preconditioning Applied to Variable and Constant Density Time-Accurate Flows on Unstructured Meshes," AIAA Paper 94-2209, June 1994.

13. Turkel, E., "Preconditioning Techniques in Computational Fluid Dynamics," *Annual Review of Fluid Mechanics*, Vol. 31, 1999, pp. 385–416.

14. Venkateswaran, S. and Merkle, C. L., "Dual Time Stepping and Preconditioning for Unsteady Computations," AIAA Paper 95-0078, January 1995.

15. Venkateswaran, S. and Merkle, C. L., "Analysis of Preconditioning Methods for the Euler and Navier-Stokes Equations," Lecture notes prepared for the 30th Computational Fluid Dynamics Lecture Series Program of the von Karman Institute (VKI) for Fluid Dynamics, Rhode-Saint Genese, Belgium, March 15-17 1999.

16. Venkateswaran, S. and Merkle, C. L., "Efficiency and Accuracy Issues in Contemporary CFD Algorithms," AIAA Paper 2000-2251, June 2000.

17. Edwards, J. R., "A Low-Diffusion Flux-Splitting Scheme for Navier-Stokes Calculations," *Computers and Fluids*, Vol. 26, No. 6, 1997, pp. 635–659.

18. Edwards, J. R., "Towards Unified CFD Simulation of Real Fluid Flows," AIAA Paper 2001-2524, June 2001.

19. Wesseling, P., "Introduction to Multigrid Methods," NASA CR-195045, 1995.

20. Osher, S. and Sethian, J. A., "Fronts Propagating with Curvature Dependent Speed: Algorithms Based on Hamilton-Jacobi Formulations," *Journal of Computational Physics*, Vol. 79, 1988, pp. 12–49.

21. Osher, S. and Fedkiw, R. P., *Level Set Methods and Dynamic Implicit Surfaces*, Vol. 153 of *Applied Mathematical Sciences*, Springer-Verlag New York, Inc., 2003.

22. Sethian, J. A., "Evolution, Implementation, and Application of Level Set and Fast Marching Methods for Advancing Fronts," *Journal of Computational Physics*, Vol. 169, 2001, pp. 503–555.

23. Sethian, J. A., *Level Set Methods and Fast Marching Methods*, Cambridge University Press, Cambridge, UK, 1999.

24. Fadlun, E. A., Verzicco, R., Orlandi, P., and Mohd-Yusof, J., "Combined Immersed-Boundary Finite-Difference Methods for Three-Dimensional Complex Flow Simulations," *Journal of Computational Physics*, Vol. 161, 2000, pp. 35–60.

25. Kim, J., Kim, D., and Choi, H., "An Immersed-Boundary Finite-Volume Method for Simulations of Flow in Complex Geometries," *Journal of Computational Physics*, Vol. 171, 2001, pp. 132–150.

26. Gilmanov, A., Sotiropoulos, F., and Balaras, E., "A general reconstruction algorithm for simulating flows with complex 3D immersed boundaries on Cartesian grids," *Journal of Computational Physics*, Vol. 191, 2003, pp. 660–669.

27. Mittal, R. and Iaccarino, G., "Immersed Boundary Methods," *Annual Review of Fluid Mechanics*, Vol. 37, 2005, pp. 239–261.

28. Tian, M., *A 2-D Numerical Simulation of Internal Two-Phase Flow for Aerated-Liquid Injectors*, Master's thesis, North Carolina State University, September 2002.

29. Drew, D. A. and Lahey, R. T., "Application of General Constitutive principles of the Derivation of Multidimensional Two-Phase Flow Equations," *International Journal of Multiphase Flow*, Vol. 5, 1979, pp. 243–264.

30. Menter, F. R., "Improved Two-Equation k-ω Turbulence Models for Aerodynamic Flows," NASA TM-103975, 1992.

31. Menter, F. R., "Two Equation Eddy Viscosity Turbulence Models for Engineering Applications," *AIAA Journal*, Vol. 32, No. 8, 1994, pp. 1598–1605.

32. Lindau, J., Venkateswaran, S., Kunz, R., and Merkle, C., "Development of a Fully Compressible Multi-Phase Reynolds Averaged Navier Stokes Model," AIAA Paper 2001-2648, June 2001.

33. McBride, B. J., Gordon, S., and Reno, M. A., "Coefficients for Calculating Thermodynamic and Transport Properties of Individual Species," NASA TM-4513, October 1993.

34. Wilke, C. R., "A Viscosity Equation for Gas Mixtures," *Chemical Physics*, Vol. 18, No. 4, April 1950, pp. 517–519.

35. Saurel, R., Cocchi, J. P., and Butler, P. B., "Numerical Study of Cavitation in the Wake of a Hypervelocity Underwater Projectile," *Journal of Propulsion and Power*, Vol. 15, No. 4, July-August 1999, pp. 513–522.

36. Oldenbourg, R., *Properties of Water and Stream in SI-Units*, Springer-Verlag, Berlin, 1989.

37. Lide, D. R. and Kehiaian, H. V., *CRC Handbook of Thermophysical and Thermochemical Data*, CRC Press, Inc., 1994.

38. Wilcox, D. C., *Turbulence Modeling for CFD*, DCW Industries, 2nd ed., 1998.

39. Tannehill, J. C., Anderson, D. A., and Pletcher, R. H., *Computational Fluid Mechanics and Heat Transfer*, Taylor and Francis, Washington DC, 2nd ed., 1997.

40. Brackbill, J. U., Kothe, D. B., and Zemach, C., "A Continuum Method for Modeling Surface Tension," *Journal of Computational Physics*, Vol. 100, 1992, pp. 335–354.

41. Gidaspow, M., *Multiphase Flow and Fluidization*, Academic Press, 1st ed., 1994.

42. Van Leer, B., Lee, W. T., and Roe, P. L., "Characteristic Time-Stepping or Local Preconditioning of the Euler Equations," AIAA Paper 91-1552-CP, July 1991.

43. Oefelein, J. C. and Yang, V., "Simulation and Analysis of Supercritical Multiphase Combustion Processes," AIAA Paper 96-2880, June 1996.

44. Merkle, C. L., Sullivan, J. Y., Buelow, P. E. O., and Venkateswaran, S., "Computation of Flows with Arbitrary Equations of State," *AIAA Journal*, Vol. 36, No. 4, 1998, pp. 515–521.

45. Kunz, R. F. e. a., "A preconditioned Navier-Stokes method for two-phase flows with application to cavitation prediction," AIAA Paper 99-3329, June 1999.

46. Neaves, M. and Edwards, J., "Hypervelocity Underwater Projectile Calculations Using a Preconditioning Algorithm," AIAA Paper 2003-1286, January 2003.

47. Tian, M., Xiao, X., and Edwards, J., "Numerical Simulation and Experimental Characterization of the Internal Two-Phase Flow within an Aerated-Liquid Injector," AIAA Paper 2004-2645, June 2004, unpublished.

48. Chorin, A. J., "A Numerical Method for Solving Incompressible Viscous Flow Problems," *Journal of Computational Physics*, Vol. 2, 1967, pp. 12–26.

49. Liou, M.-S. and Edwards, J. R., "Numerical Speed of Sound and its Application to Schemes for All Speeds," AIAA Paper 99-3268-CP, June 1999.

50. Liou, M.-S. and Edwards, J. R., "AUSM Schemes and Extensions for Low Mach and Multiphase Flows," Lecture notes prepared for the 30th Computational Fluid Dynamics Lecture Series Program of the von Karman Institute (VKI) for Fluid Dynamics, Rhode-Saint Genese, Belgium, March 15-17 1999.

51. Liou, M.-S. and Steffen, C. J., "A New Flux Splitting Scheme," *Journal of Computational Physics*, Vol. 107, 1993, pp. 23–39.

52. Liou, M.-S., "Ten Years in the Making—AUSM-family," AIAA Paper 2001-2521, June 2001.

53. Edwards, J. R., "A Low-Diffusion Flux-Splitting Scheme for Navier-Stokes Calculations," AIAA Paper 95-1703-CP, June 1995.

54. Edwards, J. R. and Liou, M.-S., "Low-Diffusion Flux-Splitting Methods for Flows at All Speeds," *AIAA Journal*, Vol. 36, No. 9, 1998, pp. 1610–1617.

55. Liou, M.-S., "Progress Towards an Improved CFD Method: AUSM+," AIAA Paper 95-1701, June 1995.

56. Hirsch, C., *Computational Methods for Inviscid and Viscous Flows*, Vol. 2 of *Numerical Computation of Internal and External Flows*, John Wiley & Sons Ltd., 1984.

57. Edwards, J. R., "Development of an Upwind Relaxation Multigrid Method for Computing Three-dimensional, Viscous Internal Flows," *Journal of Propulsion and Power*, Vol. 12, No. 1, 1996, pp. 145–154.

58. Suresh, A. and Huynh, H. T., "Numerical Experiments on a New Class of Nonoscillator Schemes," AIAA Paper 92-0421, January 1992.

59. Karypis, G. and Kumar, V., "A Parallel Algorithm for Multilevel Graph Partitioning and Sparse Matrix Ordering," *Journal of Parallel and Distributed Computing*, Vol. 48, 1998, pp. 71–85.

60. Snir, M., Otto, S., Lederman, S. H., Walker, D., and Dongarra, J., *MPI: The Complete reference*, The MIT Press, 1996.

61. Aoyama, Y. and Nakano, J., *RS/6000 SP: Practical MPI Programming*, IBM Corporation, 1999.

62. Saurel, R., Daniel, E., and Loraud, J. C., "Two-Phase Flows: Second-Order Schemes and Boundary Conditions," *AIAA Journal*, Vol. 32, No. 6, 1994, pp. 1214–1221.

63. Slater, S. A. and Young, J., "The Calculation of Inertial Particle Transport in Dilute Gas-Particle Flows," *International Journal of Multiphase Flow*, Vol. 27, 2001, pp. 61–87.

64. Sachdev, J. S., Groth, C. P. T., and Gottlieb, J. J., "A Parallel Solution-Adaptive Scheme for Multi-Phase Core Flows in Solid Propellant Rocket Motors," *International Journal of Computational Fluid Dynamics*, Vol. 19, No. 2, 2005, pp. 159–177.

65. Sachdev, J. S., Groth, C. P. T., and Gottlieb, J. J., "Numerical Solution of a Dilute and Disperse Gas-Particle Flow," 13th Annual Conference of the CFD Society of Canada, July 31-August 2, 2005.

66. Edwards, J. R., "Numerical Implementation of a Modified Liou-Steffen Upwind Scheme," *AIAA Journal*, Vol. 32, 1994, pp. 2120–2122.

Appendix A

Real Fluid Sound Speed

The sound speed of the real fluid system may be quite complex. It depends on many properties. In order to determine it in the mixture of gas and liquid in our study, an eigenvalue analysis is employed in a generalized equation of state,

$$\rho = \rho\left(p, T\right), \qquad h = h\left(p, T\right) \tag{A.1}$$

For simplicity, a 1-D Euler system is used to determine the eigenvalues,

$$\frac{\partial \mathbf{U}}{\partial t} + \frac{\partial \mathbf{E}}{\partial x} = 0, \quad \mathbf{U} = \begin{bmatrix} \rho \\ \rho u \\ \rho H - p \end{bmatrix}, \mathbf{E} = \begin{bmatrix} \rho u \\ \rho u^2 + p \\ \rho H u \end{bmatrix}, \mathbf{V} = \begin{bmatrix} p \\ u \\ T \end{bmatrix} \tag{A.2}$$

where $\mathbf{U}$ is the conservative variable vector, $\mathbf{E}$ is the flux vector, and $\mathbf{V}$ is the primative variable vector. H is the total enthalpy, $H = h + \frac{1}{2}u^2$. Then the eigenvalues, $\{\lambda_n\}$, are the roots of the characteristic equation resulting from the determinant,

$$\det\left(\frac{\partial \mathbf{V}}{\partial \mathbf{U}}\frac{\partial \mathbf{E}}{\partial \mathbf{V}} - \lambda \mathbf{I}\right) = 0. \tag{A.3}$$

Since it is difficult to compute $\dfrac{\partial \mathbf{V}}{\partial \mathbf{U}}$ directly, we compute $\dfrac{\partial \mathbf{U}}{\partial \mathbf{V}}$ first, then take its inverse. $\dfrac{\partial \mathbf{V}}{\partial \mathbf{U}}$ and $\dfrac{\partial \mathbf{E}}{\partial \mathbf{V}}$ are obtained as:

$$\frac{\partial \mathbf{U}}{\partial \mathbf{V}} = \begin{bmatrix} \rho_p & 0 & \rho_T \\ \rho_p u & \rho & \rho_T u \\ \rho_p H + \rho h_p - 1 & \rho u & \rho_T H + \rho h_T. \end{bmatrix}, \tag{A.4}$$

$$\frac{\partial \mathbf{E}}{\partial \mathbf{V}} = \begin{bmatrix} \rho_p u & \rho & \rho_T u \\ \rho_p u^2 + 1 & 2\rho u & \rho_T u^2 \\ \rho_p H u + \rho h_p u & \rho H + \rho u^2 & \rho_T H u + \rho h_T u \end{bmatrix}. \tag{A.5}$$

Taking the inverse of $\dfrac{\partial \mathbf{V}}{\partial \mathbf{U}}$ we get

$$\frac{\partial \mathbf{V}}{\partial \mathbf{U}} = \begin{bmatrix} \dfrac{\rho_T H + \rho h_T - \rho_T u^2}{\rho\rho_p h_T - \rho\rho_T h_p + \rho_T} & \dfrac{\rho_T u}{\rho\rho_p h_T - \rho\rho_T h_p + \rho_T} & -\dfrac{\rho_T}{\rho\rho_p h_T - \rho\rho_T h_p + \rho_T} \\ -\dfrac{u}{\rho} & \dfrac{1}{\rho} & 0 \\ \dfrac{\rho_p u^2 - \rho_p H - \rho h_p + 1}{\rho\rho_p h_T - \rho\rho_T h_p + \rho_T} & \dfrac{-\rho_p u}{\rho\rho_p h_T - \rho\rho_T h_p + \rho_T} & \dfrac{\rho_p}{\rho\rho_p h_T - \rho\rho_T h_p + \rho_T} \end{bmatrix} \tag{A.6}$$

Thus $\dfrac{\partial \mathbf{V}}{\partial \mathbf{U}} \dfrac{\partial \mathbf{E}}{\partial \mathbf{V}}$ in Eq. A.3 is obtained by multiplying $\dfrac{\partial \mathbf{V}}{\partial \mathbf{U}}$ by $\dfrac{\partial \mathbf{E}}{\partial \mathbf{V}}$:

$$\frac{\partial \mathbf{V}}{\partial \mathbf{U}} \frac{\partial \mathbf{E}}{\partial \mathbf{V}} = \begin{bmatrix} u & \dfrac{\rho^2 h_T}{\rho\rho_p h_T - \rho\rho_T h_p + \rho_T} & 0 \\ \dfrac{1}{\rho} & u & 0 \\ 0 & \dfrac{\rho - \rho^2 h_p}{\rho\rho_p h_T - \rho\rho_T h_p + \rho_T} & u \end{bmatrix} \tag{A.7}$$

Then the characteristic equation of the determinant (Eq. A.3) is:

$$(u-\lambda)\left[(u-\lambda)^2 - \frac{\rho h_T}{\rho\rho_p h_T - \rho\rho_T h_p + \rho_T}\right] = 0 \tag{A.8}$$

Solving this equation, we get the roots:

$$\lambda_1 = u, \quad \lambda_{2,3} = u \pm \sqrt{\frac{\rho h_T}{\rho\rho_p h_T - \rho\rho_T h_p + \rho_T}}. \tag{A.9}$$

These roots are similar to the results, $(u, u \pm a)$, if the ideal gas equation of state is used. Thus, the sound speed for a generalized equation of state is obtained as:

$$a = \sqrt{\frac{\rho h_T}{\rho\rho_p h_T - \rho\rho_T h_p + \rho_T}}. \tag{A.10}$$

When the ideal gas equation of state is used, the sound speed reverts to $a = \sqrt{\gamma \mathcal{R} T}$. If the flow is assumed isothermal, then the sound speed is simplified as:

$$\frac{1}{a^2} = \rho_p. \tag{A.11}$$

Appendix B

Eigenvalues of the Preconditioned System

The one-dimensional Euler system described in Appendix A can be preconditioned as:

$$\mathbf{P}\frac{\partial \mathbf{V}}{\partial t} + \frac{\partial \mathbf{E}}{\partial x} = 0 \tag{B.1}$$

where $\mathbf{P}$ is the preconditioning matrix obtained using the same method described in Section 3.1:

$$\mathbf{P} = \begin{bmatrix} \rho_p + \Theta & 0 & \rho_T \\ (\rho_p + \Theta)u & \rho & \rho_T u \\ (\rho_p + \Theta)H + \rho h_p - 1 & \rho u & \rho_T H + \rho h_T \end{bmatrix}, \tag{B.2}$$

$$\Theta = \frac{1}{V_{ref}^2} - \frac{1}{a^2}. \tag{B.3}$$

The eigenvalues of the preconditioned system, i.e., $\mathbf{P}^{-1}\dfrac{\partial \mathbf{E}}{\partial \mathbf{V}}$, are obtained as follows using the same procedure described in Appendix A:

$$\lambda_1 = u, \quad \lambda_{2,3} = u' \pm a' = \frac{1 + M_{ref}^2}{2}\left[u \pm a\frac{\sqrt{\left(1 - M_{ref}^2\right)^2 M^2 + 4M_{ref}^2}}{1 + M_{ref}^2}\right], \tag{B.4}$$

where

$$M_{ref} = \frac{V_{ref}}{a}, \quad M = \frac{u}{a} \tag{B.5}$$

are the reference Mach number and the Mach number respectively.

Appendix C

Interface Flux Jacobian Matrices

The matrices A-G in Section 3.3 are functions of the inviscid and viscous flux Jacobians. This chapter introduces an implicit formulation to construct these matrices, which is detailed in [17; 66]. Implicit techniques are used to integrate the unsteady Navier-Stokes equations. A local time linearization of the nonlinear system is usually required. Also, a matrix inversion procedure for solving the linear system at each time level is required too.

A first-order linearization of the LDFSS interface flux $\mathbf{E}_{i+\frac{1}{2}}$ (in ξ direction) can be constructed by defining

$$\begin{aligned} &\frac{\partial \mathbf{E}_{i+\frac{1}{2}}}{\partial \mathbf{V}_{i+\frac{1}{2}}} \Delta V_{i+\frac{1}{2}} = A^{+}_{i+\frac{1}{2}} \Delta V_i + A^{-}_{i+\frac{1}{2}} \Delta V_{i+1}, \\ &A^{+}_{i+\frac{1}{2}} = \frac{\partial \mathbf{E}_{i+\frac{1}{2}}}{\partial \mathbf{V}_i}, \quad A^{-}_{i+\frac{1}{2}} = \frac{\partial \mathbf{E}_{i+\frac{1}{2}}}{\partial \mathbf{V}_{i+1}}, \end{aligned} \tag{C.1}$$

where $\mathbf{E}_{i+\frac{1}{2}}$ is the interface flux as defined in Eq. 3.12,

$$\mathbf{E}_{i+\frac{1}{2}} = \mathbf{E}^{c}_{i+\frac{1}{2}} + \mathbf{E}^{p}_{i+\frac{1}{2}} = \frac{|\nabla \xi|}{J} \left(U^{+} \Phi_i + U^{-} \Phi_{i+1} \right) + \frac{|\nabla \xi|}{J} P_{\frac{1}{2}} \Psi_i. \tag{C.2}$$

The direct calculations of the above expressions are rather complicated and expensive to compute. A simpler, approximate linearization with good stability properties can be derived by contracting the expressions for the 'positive' and 'negative' flux Jacobians $A^{+}_{i+\frac{1}{2}}$ and $A^{-}_{i+\frac{1}{2}}$ to the grid nodes i and $i+1$, respectively. This procedure results in the following implicit representation:

$$\frac{\partial \mathbf{E}_{i+\frac{1}{2}}}{\partial \mathbf{V}_{i+\frac{1}{2}}} \Delta V_{i+\frac{1}{2}} = A^{+}_{i} \Delta V_i + A^{-}_{i+1} \Delta V_{i+1}, \tag{C.3}$$

where

$$A_i^{\pm} = \frac{1}{2}\left[\frac{\partial \mathbf{E}_i}{\partial \mathbf{V}_i} \pm \left(\left.\frac{\partial \mathbf{E}_{i+\frac{1}{2}}}{\partial \mathbf{V}_i}\right|_i - \left.\frac{\partial \mathbf{E}_{i+\frac{1}{2}}}{\partial \mathbf{V}_{i+1}}\right|_i\right)\right]. \tag{C.4}$$

The last two derivatives in Eq. C.4 are both contracted to grid node i to make the Jacobian matrix simpler. $\mathbf{E}_i$ is the actual flux as defined in Eq. 3.10,

$$\mathbf{E}_i = \mathbf{E}_i^c + \mathbf{E}_i^p = \frac{|\nabla\xi|}{J}\left(\overline{\mathcal{U}}\Phi_i + p_i\Psi_i\right). \tag{C.5}$$

Thus, the differentiation of $\mathbf{E}_i$ can be expressed as

$$\frac{\partial \mathbf{E}_i}{\partial \mathbf{V}_i} = \frac{|\nabla\xi|}{J}\left[\overline{\mathcal{U}}\left(\frac{\partial \Phi}{\partial \mathbf{V}}\right)_i + \Phi_i\Psi_i^T + \Psi_i\vec{v}^T\right], \tag{C.6}$$

where $\vec{v}$ is defined in Eq. 3.3.

The linearization of flux Jacobians can be obtained by index contraction as follows:

$$\left.\frac{\partial \mathbf{E}_{i+\frac{1}{2}}}{\partial \mathbf{V}_i}\right|_i - \left.\frac{\partial \mathbf{E}_{i+\frac{1}{2}}}{\partial \mathbf{V}_{i+1}}\right|_i = \frac{|\nabla\xi|}{J}\left[|\overline{\mathcal{U}}|\left(\frac{\partial \Phi}{\partial \mathbf{V}}\right)_i + \Phi_i r^T + \Psi_i s^T\right], \tag{C.7}$$

where

$$r = \begin{bmatrix} 0 \\ \vdots \\ 0 \\ 0 \\ 2\tilde{a}_{\frac{1}{2}}M_{\frac{1}{2}}/(\rho_i V_{ref}^2) \\ \xi_x\left[(1+\beta_i)\,\mathrm{sign}\,(M_i) - \beta_i M_i\right] \\ \xi_y\left[(1+\beta_i)\,\mathrm{sign}\,(M_i) - \beta_i M_i\right] \\ \xi_z\left[(1+\beta_i)\,\mathrm{sign}\,(M_i) - \beta_i M_i\right] \\ 0 \end{bmatrix}, \quad s = \begin{bmatrix} 0 \\ \vdots \\ 0 \\ 0 \\ (1+\beta_i)\,\mathrm{sign}\,(M_i) - \beta_i M_i \\ -\xi_x\beta_i\rho_{\frac{1}{2}}V_{ref}^2 g'(M_i)/\tilde{a}_{\frac{1}{2}} \\ -\xi_y\beta_i\rho_{\frac{1}{2}}V_{ref}^2 g'(M_i)/\tilde{a}_{\frac{1}{2}} \\ -\xi_z\beta_i\rho_{\frac{1}{2}}V_{ref}^2 g'(M_i)/\tilde{a}_{\frac{1}{2}} \\ 0 \end{bmatrix}. \tag{C.8}$$

The flux Jacobians $A_i^{\pm}$, then, may be expressed as

$$A_i^{\pm} = \frac{|\nabla\xi|}{2J}\left[\left(\overline{\mathcal{U}} \pm |\overline{\mathcal{U}}|\right)\left(\frac{\partial \Phi}{\partial \mathbf{V}}\right)_i + \Phi_i\left(\Psi_i^T \pm r^T\right) + \Psi_i\left(\vec{v}^T \pm s^T\right)\right], \tag{C.9}$$

where $\dfrac{\partial \Phi}{\partial \mathbf{V}}$ can be expressed as

$$\frac{\partial \Phi}{\partial \mathbf{V}} = \begin{bmatrix} \rho Y_g + \rho_{Y_{g,1}} Y_{g,1} Y_g & \cdots & \rho_{Y_{g,N_g-1}} Y_{g,1} Y_g & \rho Y_{g1} + \rho_{Y_g} Y_{g,1} Y_g & \rho_p Y_{g,1} Y_g & 0 & 0 & 0 & \rho_T Y_{g,1} Y_g \\ \vdots & \ddots & \vdots & \vdots & \vdots & \vdots & \vdots & \vdots & \vdots \\ \rho_{Y_{g,1}} Y_{g,N_g-1} Y_g & \cdots & \rho Y_g + \rho_{Y_{g,N_g-1}} Y_{g,N_g-1} Y_g & \rho Y_{g,N_g-1} + \rho_{Y_g} Y_{g,N_g-1} Y_g & \rho_p Y_{g,N_g-1} Y_g & 0 & 0 & 0 & \rho_T Y_{g,N_g-1} Y_g \\ \rho_{Y_{g,1}} Y_g & \cdots & \rho_{Y_{g,N_g-1}} Y_g & \rho + \rho_{Y_g} Y_g & \rho_p Y_g & 0 & 0 & 0 & \rho_T Y_g \\ \rho_{Y_{g,1}} & \cdots & \rho_{Y_{g,N_g-1}} & \rho_{Y_g} & \rho_p & 0 & 0 & 0 & \rho_T \\ \rho_{Y_{g,1}} u & \cdots & \rho_{Y_{g,N_g-1}} u & \rho_{Y_g} u & \rho_p u & \rho & 0 & 0 & \rho_T u \\ \rho_{Y_{g,1}} v & \cdots & \rho_{Y_{g,N_g-1}} v & \rho_{Y_g} v & \rho_p v & 0 & \rho & 0 & \rho_T v \\ \rho_{Y_{g,1}} w & \cdots & \rho_{Y_{g,N_g-1}} w & \rho_{Y_g} w & \rho_p w & 0 & 0 & \rho & \rho_T w \\ \rho_{Y_{g,1}} H + \rho h_{Y_{g,1}} & \cdots & \rho_{Y_{g,N_g-1}} H + \rho h_{Y_{g,N_g-1}} & \rho_{Y_g} H + \rho h_{Y_g} & \rho_p H + \rho h_p & \rho u & \rho v & \rho w & \rho_T H + \rho h_T \end{bmatrix} \tag{C.10}$$

Appendix D

One-Dimensional Injector Theoretical Analysis

In the injector simulations, a one-dimensional theoretical analysis is used to provide a consistency check when comparing pressure predictions with experimental measurements. The two-phase mixture flow is assumed isothermal (as in the simulations) and thermal non-equilibrium (with a liquid-phase energy equation from Saurel, et al.[35]).

The flow is assumed to be a homogeneous mixture of liquid water and nitrogen gas that is choked at the injector exit. Frictional forces are neglected due to the small axial extent of the injector and gravitational effects (though included in the analysis) are found to be negligible.

For the two-phase mixture model under isothermal conditions, the sound speed a resulting from the eigenvalue analysis is given in Eq. 2.43:

$$\frac{1}{a^2} = \rho_p = \left(\frac{\rho}{\rho_g}\right)^2 Y_g \frac{\partial \rho_g}{\partial p} + \left(\frac{\rho}{\rho_l}\right)^2 Y_l \frac{\partial \rho_l}{\partial p}. \tag{D.1}$$

Then $u_e = a_e$, where the subscript 'e' represents the exit plane of the injector. According to the mass conservation and momentum conservation, we have the following equations for mass and momentum.

$$\text{continuity} \quad : \quad \int_A \rho \mathbf{v} \cdot \mathbf{n} \mathrm{d}A = 0, \tag{D.2}$$

$$\text{gas phase continuity} \quad : \quad \int_A \rho Y_g \mathbf{v} \cdot \mathbf{n} \mathrm{d}A = 0, \tag{D.3}$$

$$\text{axial momentum conservation} \quad : \quad \int_A \rho u \mathbf{v} \cdot \mathbf{n} \mathrm{d}A = -\int_A p n_x \mathrm{d}A + \int_V \rho g \mathrm{d}V, \tag{D.4}$$

We can evaluate Eq. D.2 over the surface of the injector tube, considering gas mass injection as defined by the GLR value. The continuity equation can thus be written as a function f_1:

$$f_1 = \rho_e a_e - (1 + \text{GLR})\rho_i u_i = 0, \tag{D.5}$$

where the subscript 'i' represents the inlet plane. Combining continuity and gas phase continuity equations, we have

$$Y_{g,e} = \frac{\text{GLR}}{1 + \text{GLR}}. \tag{D.6}$$

With this, Eq. D.5 can be solved iteratively using Newton's method to yield the exit plane pressure. Similarly, from the momentum equation, we have

$$p_i = p_e - \rho_{l,e} g L_{tube} + \rho_e a_e^2 - \rho_\infty u_\infty^2, \tag{D.7}$$

where p_i is the inlet pressure, $g = -9.81$ m/s^2 is the gravity acceleration, and L_{tube} is the length of the tube.

For the thermal non-equilibrium case, the energy equation must be considered in the analysis. In this case, the sound speed from the eigenvalue analysis is given as

$$a^2 = \frac{\rho h_T}{\rho\rho_p h_T - \rho\rho_T h_p + \rho_T}, \tag{D.8}$$

where

$$\rho_T = \left(\frac{\rho}{\rho_g}\right)^2 Y_g \frac{\partial \rho_g}{\partial T_g} + \left(\frac{\rho}{\rho_l}\right)^2 Y_l \frac{\partial \rho_l}{\partial T_l}, \tag{D.9}$$

$$h_T = Y_g \frac{\partial h_g}{\partial T_g} + Y_l \frac{\partial h_l}{\partial T_l}. \tag{D.10}$$

The adiabatic energy equation is also added to the system:

$$\int_A \rho h_0 \mathbf{v} \cdot \mathbf{n} \mathrm{d}A = 0. \tag{D.11}$$

After some substitution steps, we get two more functions f_2, and f_3:

$$f_2 = \left(h_l + \frac{1}{2}a^2\right)|_e - h_{0l}|_i = 0, \quad f_3 = \left(h_g + \frac{1}{2}a^2\right)|_e - h_{0g}|_i = 0, \tag{D.12}$$

Now we need to simultaneously solve the coupled equation system (Eq. D.5 and Eq. D.12) iteratively using Newton's method to yield the exit plane temperature and pressure.

Appendix E

Immersed Boundary Algorithm

An immersed boundary technique developed by the Edwards group (references available soon) is used in simulations for the injector flowfield with the probe. The procedure is not restricted to Cartesian grids. It starts from the basic idea of Fadlun, et al. [24]. In Ref. [24], the key concept is that the velocity of the fluid must be equal to the velocity of the moving body at its surface. This is achieved by applying a forcing function to the momentum equations such that the desired boundary velocity is recovered as the solution at each time step. In Edwards' method, the forcing function is defined in the context of the subiteration step. This is achieved by formulating the governing equations as an implicit system at time level $n+1$. The flow properties, $\mathbf{V} = [y_{g,1}, \ldots, Y_g, p, u, v, w, T]^T$ are updated from time level n ($V^{n+1,m=0} = V^n$) to time level $n+1$ over $m_{\max}$ subiterations ($V^{n+1,m=m_{\max}} = V^{n+1}$) expressed as follows:

$$R^{n+1,m}_{y_{g,1},\mathrm{IB}} = \left(1 - G(\phi^{n+1})\right) R^{n+1,m}_{y_{g,1}} + G(\phi^{n+1})(y^{n+1,m}_{g,1} - y^{n+1,m}_{g,1,\mathrm{B}}), \tag{E.1}$$

$$R^{n+1,m}_{Y_g,\mathrm{IB}} = \left(1 - G(\phi^{n+1})\right) R^{n+1,m}_{Y_g} + G(\phi^{n+1})(Y^{n+1,m}_{g} - Y^{n+1,m}_{g,\mathrm{B}}), \tag{E.2}$$

$$R^{n+1,m}_{c,\mathrm{IB}} = \left(1 - G(\phi^{n+1})\right) R^{n+1,m}_{c} + G(\phi^{n+1})(p^{n+1,m} - p^{n+1,m}_{B}), \tag{E.3}$$

$$R^{n+1,m}_{u_i,\mathrm{IB}} = \left(1 - G(\phi^{n+1})\right) R^{n+1,m}_{u_i} + G(\phi^{n+1})(u^{n+1,m}_{i} - u^{n+1,m}_{i,\mathrm{B}}), \tag{E.4}$$

$$R^{n+1,m}_{E,\mathrm{IB}} = \left(1 - G(\phi^{n+1})\right) R^{n+1,m}_{E} + G(\phi^{n+1})(T^{n+1,m} - T^{n+1,m}_{\mathrm{B}}). \tag{E.5}$$

where $G(\phi(\mathbf{x}, t))$ is a sharp Heaviside function:

$$G(\phi(\mathbf{x}, t)) \begin{cases} = 0 & \mathbf{x} \in \text{field points} \\ = 1 & \mathbf{x} \in \text{band points} \\ = 1 & \mathbf{x} \in \text{interior points} \end{cases} \tag{E.6}$$

and $\phi(\mathbf{x}, t)$ is a signed distance function:

$$\phi(\mathbf{x}, t) \begin{cases} > 0 & \mathbf{x} \in \text{field points} \\ > 0 & \mathbf{x} \in \text{band points} \\ < 0 & \mathbf{x} \in \text{interior points} \end{cases} \tag{E.7}$$

The quantities $\mathbf{V}_B$ are values to which the hydrodynamics solution will relax within the course of the subiteration procedure. These are defined according to interpolation methods presented later. Fig. E.1 shows different types of cell center points in the domain including an immersed body.

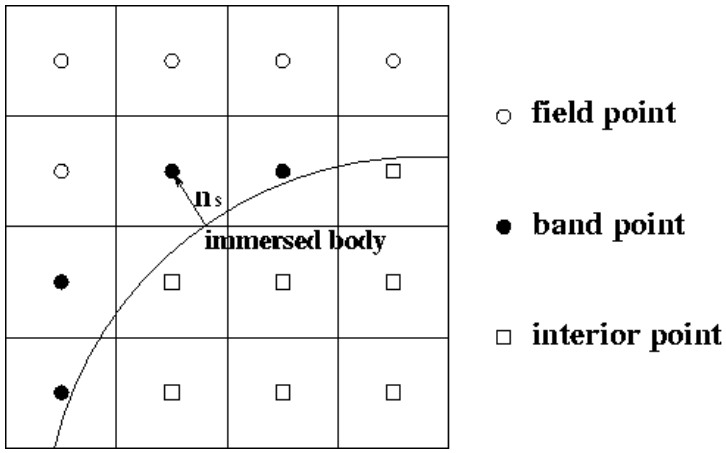

Figure E.1: Different cell center points in the domain including an immersed body

The signed distance is calculated from each field point $\mathbf{x}_k$ to the nearest surface point on each surface $\mathbf{x}_{s,l(k)}$. First, approximate nearest-neighbor searching techniques are used to get the unsigned distance. In practice, this is done only for the number of field points that are within a "bounding box" surrounding the particular surface. Distances outside the "bounding box" are assigned to be a very large positive number. Then, the signed distance function is obtained by multiplying the unsigned distance with the sign of the inner product of the distance vector with the outward normal:

$$\phi_s(\mathbf{x}_k, t) = \text{sign}[(\mathbf{x}_k - \mathbf{x}_{s,l(k)}) \cdot \mathbf{n}_{s,l(k)}]|\mathbf{x}_k - \mathbf{x}_{s,l(k)}|. \tag{E.8}$$

Finally, the global signed distance function at point $\mathbf{x}_k$ is taken as the minimum of

the individual signed distance functions at that point:

$$\phi(\mathbf{x}_k, t) = \min_s[\phi_s(\mathbf{x}_k, t)]. \tag{E.9}$$

The flow properties at field points are calculated from Navier-Stokes equations, which is in the limit $G = 0$ in Eqns.E.1-E.5. For band and interior points, the Navier-Stokes equations are not solved. The flow properties at these points are forced as a function of the field point solutions in neighboring cells and surface velocities. The velocity solution within the band ($u_{i,\mathrm{B}}$) needs to be determined using interpolation techniques, as it is not required that the band cell align with the immersed body.

For interior points, the forcing velocity $u_{i\mathrm{B}}$ is set to that of the nearest surface point, and the other variables are assigned constant values.

For band points, a velocity distribution is first defined in terms of the normal coordinate n. Given that the vector $\mathbf{n}_i = n_x\mathbf{i} + n_y\mathbf{j} + n_z\mathbf{k}$ defines the local surface normal at the nearest surface point $\mathbf{x}_s$ to the band point in question, a general velocity distribution is written as follows:

$$u_{i,\mathrm{B}}(n) = [(u_{I,i} - u_{s,i}) - \mathbf{n}_i(u_{I,i} - u_{s,i}) \cdot \mathbf{n}_i] \left(\frac{n}{d_I}\right)^k + A\mathbf{n}_i(u_{I,i} - u_{s,i}) \cdot \mathbf{n}_i \left(\frac{n}{d_I}\right)^p + u_{s,i}, \tag{E.10}$$

where $u_{I,i}$ is an interpolated velocity and d_I is the location in the direction of the normal coordinate at which the interpolated velocity is defined. Functional forms for these will be presented later. The quantity $u_{s,i}$ is the surface velocity corresponding to the nearest surface point to the band point in question. The forcing velocity for a particular band point $\mathbf{x}_k$ is obtained by evaluating Eq. E.10 at $n = \phi(\mathbf{x}_k, t)$.

The velocity distribution is written in terms of a general power law $\sim n^k$. The constant A (0 or 1) is a "tangency correction" flag that allows the normal component of velocity within the band ($u_{i,\mathrm{B}}(d) \cdot \mathbf{n}_i$) to vary in accord with a different power law ($\sim n^p$) (for $A = 1$) or to remain equal to the surface normal velocity ($u_{s,i}(d) \cdot \mathbf{n}_i$)

throughout the band (for $A = 0$). The calculations for the injector flowfield with the probe use $k = 1$, $p = 2$ and $A = 1$.

A general procedure for interpolating the pressure or some other quantity to the surface is given by the following. The quantity of interest q is represented as a second-order polynomial in the normal distance n for points within the band:

$$q(n) - q_0 = A + Bn + Cn^2, \tag{E.11}$$

with boundary conditions at $n = 0$ given as:

$$(q(n) - q_0)|_{n=0} = q_w - q_0 = A, \quad \frac{\mathrm{d}(q(n) - q_0)}{\mathrm{d}n}\Big|_{n=0} = \beta(q_w - q_0) = B. \tag{E.12}$$

where β is a parameter that enforces either a Neumann boundary conditon ($\beta \to 0$), a Dirichlet boundary condition ($\beta \to \infty$), or some kind of mixed boundary condition for $0 < \beta < \infty$. Substituting these conditions into the polynomial form (Eq. E.11) and its first derivative gives:

$$\hat{q}(n) \equiv q(n) - q_0 = (q_w - q_0)(1 + \beta n) + Cn^2, \quad \frac{\mathrm{d}(\hat{q}(n))}{\mathrm{d}n} \equiv \frac{\mathrm{d}(q(n) - q_0)}{\mathrm{d}n} = \beta(q_w - q_0) + 2Cn. \tag{E.13}$$

At the location of the interpolation point outside the band, these expressions become:

$$\hat{q}(d_I) = (q_w - q_0)(1 + \beta d_I) + Cd_I^2, \quad \frac{\mathrm{d}(\hat{q}(n))}{\mathrm{d}n}\Big|_I = \beta(q_w - q_0) + 2Cd_I. \tag{E.14}$$

Solving this system for the unknowns $q_w - q_0$ and C yields:

$$q_w - q_0 = \frac{2d_I\hat{q}(d_I) - \frac{\mathrm{d}(\hat{q}(n))}{\mathrm{d}n}\Big|_I d_I^2}{2d_I(1 + \beta d_I) - \beta d_I^2}, \quad C = \frac{-\beta\hat{q}(d_I) + (1 + \beta d_I)\frac{\mathrm{d}(\hat{q}(n))}{\mathrm{d}n}\Big|_I}{2d_I(1 + \beta d_I) - \beta d_I^2} \tag{E.15}$$

Substituting these expressions into the functional form (Eq. E.11) gives the interpolation polynomial as follows:

$$\hat{q}(n) = \left(\frac{2d_I(1 + \beta n) - \beta n^2}{2d_I(1 + \beta d_I) - \beta d_I^2}\right)\hat{q}(d_I) - \left(\frac{d_I^2(1 + \beta n) - (1 + \beta d_I)n^2}{2d_I(1 + \beta d_I) - \beta d_I^2}\right)\frac{\mathrm{d}(\hat{q}(n))}{\mathrm{d}n}\Big|_I. \tag{E.16}$$

The calculation of $\left.\dfrac{\mathrm{d}(\hat{q}(n))}{\mathrm{d}n}\right|_I$ is equivalent to $\nabla\hat{q}(n)|_I \cdot \mathbf{n}$, with $\mathbf{n} = n_x\mathbf{i} + n_y\mathbf{j} + n_z\mathbf{k}$. The desired result will be obtained by evaluating this equation at the band point $n = \phi(\mathbf{x}_k, t)$. This procedure, with $\beta = 0$ (Neumann condition), is used for all mass fractions, pressure, and temperature within band cells.

The location at which interpolated properties are defined, d_I, is calculated for a particular field point as

$$d_I = \sum_l \omega_l(\mathbf{x}_l - \mathbf{x}_k) \cdot \mathbf{n}, \quad \omega_l = \frac{w_l}{\sum_m w_m}, \tag{E.17}$$

where w_l is a merit function defined as follows:

$$w_l = \begin{cases} \dfrac{1}{\sqrt{(|\mathbf{x}_l - \mathbf{x}_k|)^2 - ((\mathbf{x}_l - \mathbf{x}_k) \cdot \mathbf{n})^2 + \epsilon}} & \text{if } (\mathbf{x}_l - \mathbf{x}_k) \cdot \mathbf{n} > 0, \\ 0 & \text{otherwise.} \end{cases} \tag{E.18}$$

where ϵ is 10^{-12}. The index l ranges over the 26 cells that surround the given mesh cell.